

# The world of dynamical systems: multistability, neural dynamics and robotic locomotion

DISSERTATION  
zur Erlangung des Doktorgrades  
der Naturwissenschaften

vorgelegt beim Fachbereich Physik der  
Goethe-Universität Frankfurt  
in Frankfurt am Main

von  
**Bulcsú Sándor**  
aus Odorheiu-Secuiesc, Rumänien

Frankfurt am Main, Mai 2017  
D 30



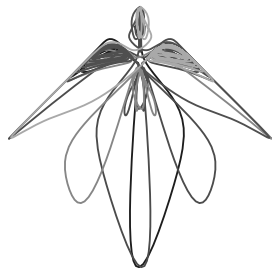
vom Fachbereich Physik der  
Johann Wolfgang Goethe - Universität  
als Dissertation angenommen.

Dekan: Prof. Dr. Owe Philipsen

Gutachter: Prof. Dr. Claudius Gros  
Prof. Dr. Zoltán Néda

Datum der Disputation:

*To my family...*  
*... and to my new family.*



# Contents

<b>Abstract</b>	<b>13</b>
<b>1 General Background</b>	<b>15</b>
1.1 On dynamical systems . . . . .	16
1.1.1 ODEs and maps . . . . .	16
1.1.2 Phase space contraction . . . . .	18
1.1.3 Attractors . . . . .	20
1.1.4 Degenerate attractors and multistability . . . . .	24
1.1.5 Transient states . . . . .	26
1.1.6 Bifurcations . . . . .	27
1.1.7 Famous experimental setups . . . . .	29
<b>2 A new prototype system with multistability</b>	<b>31</b>
2.1 Introduction to prototype dynamical systems . . . . .	32
2.2 Recipes for multistability . . . . .	33
2.2.1 A new class of prototype systems . . . . .	35
2.2.2 Polynomial friction functions . . . . .	35
2.2.3 Generalized potential functions . . . . .	37
2.3 Multistability and chaos in double-well potentials . . . . .	38
2.3.1 Limit-cycle generation . . . . .	38
2.3.2 Generating chaos in the 4-dimensional system . . . . .	41
2.4 Hopf bifurcations in the prototype system . . . . .	45
2.5 Discussion . . . . .	48
<b>3 Transient-state dynamics in neural networks</b>	<b>51</b>
3.1 Introduction to the modeling of neural networks . . . . .	52
3.1.1 Transient-states for cognitive processing . . . . .	53
3.1.2 Neurons and synaptic plasticity . . . . .	54
3.1.3 Rate-encoding neurons and the full-depletion model . . . . .	55
3.2 Transient-state dynamics generated by STSP . . . . .	58
3.2.1 Attractor networks with clique encoding . . . . .	59
3.2.2 Bifurcation analysis of the symmetric network . . . . .	62
3.2.3 Complex activity patterns in random networks . . . . .	65
3.3 Discussion . . . . .	68

<b>4</b>	<b>Robots as complex dynamical systems</b>	<b>71</b>
4.1	Introduction to locomotion robophysics . . . . .	72
4.2	The sensorimotor loop as a dynamical system . . . . .	75
4.2.1	One-neuron controller with internal adaption . . . . .	75
4.2.2	Embodiment as self-organized motion . . . . .	78
4.3	Degenerate attractors and symmetry breaking . . . . .	83
4.3.1	Sensorimotor loop with short-term synaptic plasticity . . . . .	83
4.3.2	Motion patterns as degenerate attractors . . . . .	88
4.3.3	Interactions as autonomous mode switching . . . . .	91
4.3.4	Smooth chaotic meandering . . . . .	93
4.4	Discussion . . . . .	95
<b>5</b>	<b>Conclusions</b>	<b>99</b>
	<b>Appendices</b>	<b>101</b>
<b>A</b>	<b>Dynamical systems</b>	<b>101</b>
A.1	Phase space contraction rate . . . . .	101
A.2	Box-counting dimension . . . . .	102
A.3	Lyapunov exponents . . . . .	102
A.4	Coordinate transformations and stability . . . . .	103
A.4.1	Linear transformations and eigenvalues . . . . .	103
A.4.2	Nonlinear transformations . . . . .	104
A.4.3	Fixpoints of continuous time systems . . . . .	104
A.4.4	Fixpoints of maps . . . . .	105
A.4.5	Phase space contraction . . . . .	106
<b>B</b>	<b>Prototype system</b>	<b>107</b>
B.1	Potential wells with arbitrary shape . . . . .	107
B.2	Bifurcations in the 4-dimensional system . . . . .	108
B.3	Lyapunov exponent . . . . .	110
<b>C</b>	<b>Neural networks</b>	<b>111</b>
C.1	Chaotic dynamics in the symmetric network . . . . .	111
<b>D</b>	<b>Robots</b>	<b>113</b>
D.1	Simulation parameters of the barrel robot . . . . .	113
D.2	Simulation parameters of the spherical robot . . . . .	114
D.3	Stability of the motion primitives . . . . .	115
	<b>References</b>	<b>130</b>
	<b>Acknowledgements</b>	<b>131</b>

# Zusammenfassung

Die Theorie dynamischer Systeme befasst sich typischerweise mit niedrig dimensionalen Systemen [1]. Um aber das dynamische Verhalten von komplexen Systemen, welche von einer Vielzahl von Variablen beschrieben werden, zu verstehen, muss man den Rahmen dieser Theorie erweitern. In dieser Dissertation legen wir dar, wie neu entwickelte Konzepte und Methoden es uns erlauben, die einfachen dynamischen Prinzipien zu finden, welche hinter der Komplexität stehen. In der Forschungsliteratur der letzten Jahre wurden vermehrt Methoden aus der Theorie der dynamischen Systeme als wesentliches Instrument zur Analyse diverser komplexer Phänomene eingesetzt. Um ein tieferes Verständnis für solche Systeme zu erlangen, finden diese Methoden ihre Anwendung beispielsweise bei der Analyse von neuronalen Aktivitätsmustern, wie sie im Gehirn auftreten [2, 3], oder im Zusammenhang mit biologisch inspirierten Robotern, welche implizit und selbst-organisiert ihre physische Gestalt und ihre Umgebung erfahren (Embodiment). Weitere Einsatzgebiete stellen komplexe Netzwerke im Allgemeinen [4], und insbesondere die Untersuchung von rückgekoppelten neuronalen Netzwerken dar, sowie die Regelung von multi-stabilen Systemen [5], welche eine Bandbreite von Anwendungen in verschiedenen wissenschaftlichen und technischen Disziplinen hat [6].

In **Kapitel 1** werden wir, in aller Kürze, die grundlegenden Konzepte und Methoden der Theorie dynamischer Systeme erläutern und eine einheitliche, an die gängigen Standards angelehnte Notation einführen, auf die sich alle darauffolgenden Kapitel dieser Dissertation beziehen werden. Wir beginnen mit dem mathematischen Formalismus, mit dessen Hilfe wir die Dynamik von komplizierteren Systemen, wie beispielsweise von neuronalen Netzwerken und Robotern, untersuchen. Dabei werden unter anderem Konzepte wie kontinuierliche Phasenraumflüsse und diskrete Abbildungen, Attraktoren und ihre Stabilität, aber auch Bifurkationen umfasst. Darauf folgt eine Zusammenfassung aktueller Forschungsergebnisse, samt ihrer Konzepte und Methoden, zur Untersuchung komplexer dynamischer Systeme, welche die Bedeutung von multi-stabilen Systemen, entarteten Attraktoren und Übergangszuständen in dynamischen Systemen erläutern.

In **Kapitel 2** stellen wir anschließend einen neu entwickelten Ansatz zur Konstruktion von multi-stabilen Systemen vor, welcher auf einem Baukastenprinzip beruht. Dazu stellen wir zunächst die Klasse der prototypischen dynamischen Sy-

steme vor, wobei wir darauf hinweisen, dass viele dieser Systeme sich auf ein und dieselbe Art von Gleichung zurückführen lässt. Des Weiteren veranschaulichen wir, wie die Regelung des Energiegleichgewichts genutzt werden kann, um Bifurkationen zu erzeugen. In Abschnitt 2.2 präsentieren wir eine neue Klasse dynamischer Systeme [7], welche als Prototypen für die Modellierung und Untersuchung von komplexen Bifurkationsszenarien von Grenzzyklen und chaotischen Attraktoren dienen, wie sie in komplexeren Systemen höherer Dimension vorkommen können.

Um die Regionen im Phasenraum zu regulieren, in welchen Energie aufgenommen bzw. abgegeben wird, fügen wir einen neuartigen Reibungsterm hinzu, welcher explizit vom mechanischen Potential abhängt, das wiederum aus einer endlichen Anzahl von lokalen Minima besteht.

Indem wir ein verallgemeinertes Potential definieren und damit die Position und Tiefe der jeweiligen Minima bestimmen, sind wir in der Lage – wie mit einem Kochrezept – ein System mit einer bestimmten Anzahl verschiedener Attraktoren zusammenzustellen.

Wir zeigen anhand zweier Beispiele in Abs. 2.3, welche verschiedenen Attraktoren sich mit Hilfe eines einfachen Doppelmuldenpotentials in einem Phasenraum mit Regionen, in denen abwechselnd Energie aufgenommen bzw. abgegeben wird, erzeugen lassen. In einem zweidimensionalen System mit einer Raumdimension lässt sich eine Kaskade von Bifurkationen von Grenzzyklen beobachten. In einem vierdimensionalen Phasenraum (zwei Raumdimensionen) zeigt das Prototypsystem eine Symmetrie brechende Bifurkation bevor eine Kaskade von Periodenverdopplungen das System ins Chaos überführt. Im Falle des beobachteten chaotischen Attraktors kann ebenfalls Intermittenz beobachtet werden. Dabei zeigen wir weiter, dass die Erzeugung von Grenzzyklen aus destabilisierten Fixpunkten nicht von der Form des Potentials an sich bedingt wird. Die einzige Bedingung hierfür ist das Vorhandensein einer endlichen Anzahl von lokalen Minima. Das Kapitel schließt in Abs. 2.4 mit einer analytischen Herleitung für die Erzeugung von Grenzzyklen.

Eines der faszinierendsten ungelösten Probleme der zeitgenössischen Forschung betrifft die Betrachtung des Nervensystems als komplexes, adaptives, dynamisches System [1]. Nichtsdestotrotz birgt die Beschreibung der Dynamik in neuronalen Netzwerken neue Herausforderungen für die klassische Theorie dynamische Systeme [8].

In **Kapitel 3**, stellen wir eine weitere Herangehensweise für die theoretische Behandlung des Nervensystems vor. Dabei werden sowohl das gesamte Repertoire dynamischen Verhaltens, als auch die Bestandteile, welche für die Generierung der einzelnen dynamischen Ausprägungen verantwortlich sind, analysiert, um so das zugrunde liegende Verhalten zu verstehen. Dieser Ansatz stellt einen Zugang zum Feld der Neurowissenschaften her, welcher komplementär ergänzend zur Methodik

---

der Computational Neuroscience ist. Des Weiteren könnte dieser Ansatz zur Entwicklung neuer nützlicher Methoden auf dem Gebiet der nichtlinearen Dynamik beitragen. In diesem Zusammenhang präsentieren wir an dieser Stelle eine neue Klasse von rekurrenten neuronalen Netzwerken, welche Übergangszustände [9] hervorruft, ohne dabei auf externe Stimuli angewiesen zu sein. Wir erörtern die Rolle der synaptischen Kurzzeitplastizität [10] (short-term synaptic plasticity) für die Dynamik des Netzwerkes. Dabei könnte die Kurzzeitplastizität für die Entstehung von Übergangszuständen verantwortlich sein, welche von wenigen Millisekunden bis hin zu einigen Sekunden andauern.

Zu Beginn zeigen wir die wesentlichen Herausforderungen, welche sich ergeben, wenn man das Gehirn als dynamisches System beschreibt, und legen ebenfalls dar, inwieweit das Konzept der Übergangszustände typisch für die Dynamik verschiedener kognitiver Prozesse ist [3]. Darüberhinaus werden Standardmodelle für die Modellierung von Neuronen kontinuierlicher Aktivität und synaptischer Kurzzeitplastizität vorgestellt. Daraufhin folgt eine Analyse der Bifurkationen in einem symmetrischen neuronalen Netzwerk, welches aus vier Neuronen besteht, in Abhängigkeit eines konstanten, globalen externen Stimulus. Dadurch erhalten wir ein tieferes Verständnis für den Zusammenhang der Übergangszustände mit den zerstörten Attraktoren des Netzwerkes. Schließlich präsentieren wir anhand von Beispielen Übergangszustände in größeren Zufallsnetzwerken, welche sich entweder in Form von regulären grenzyklischen Oszillationen oder von chaotisch fluktuierenden Aktivitätsmustern zeigen.

Um zu demonstrieren, welche Rolle die Kurzzeitplastizität für die Entstehung von raum-zeitlichen Mustern spielt, wie sie in vielen kognitiven Phänomenen beobachtet wird, betrachten wir Netzwerke, welche Cliques kodieren, d. h. deren Fixpunkte Cliques aktiver Neuronen sind. Die exzitatorischen und inhibitorischen Strukturen verhalten sich dabei komplementär zueinander. Die zugrundeliegende Topologie des Netzwerkes ist nicht nur biologisch plausibel, sondern ermöglicht auch eine beliebig große Zahl an möglichen Zuständen, welche in diesem Fall jeweils einer Clique aktiver, exzitatorisch verbundener Neuronen entsprechen.

Der von uns vorgeschlagene Mechanismus zur Generierung von Übergangszuständen basiert nicht auf heteroklinen Kanälen, welche im Allgemeinen nicht stabil sind und nur in Systemen mit spezieller Topologie vorkommen [3]. Daher sind wir der Auffassung, dass die hier vorgestellten Prinzipien insbesondere große Bedeutung für die Modellierung von biologisch realistischen neuronalen Netzwerken haben, welche im Allgemeinen durch die Präsenz mehrerer verschiedener Zeitskalen charakterisiert werden.

Das Forschungsgebiet der künstlichen Intelligenz ist im Allgemeinen sehr stark mit den Gebieten Computational Neuroscience und Hirnforschung verknüpft. Teilgebiete, die sich mit künstlichen kognitiven Systemen und autonomen Robo-

tern befassen, versuchen die Ergebnisse und Methoden der Neurowissenschaften, Kognitionswissenschaften und der Theorie komplexer Systeme zu vereinen und gleichzeitig neue Paradigmen für selbstständig agierende künstliche Systeme und Roboter zu entwickeln. In diesem Sinne erweitern wir in **Kapitel 4** den Anwendungsbereich der Theorie dynamischer Systeme und ihrer Konzepte auf die Untersuchung robotischer Fortbewegung. Dafür kombinieren wir die Ergebnisse der vorhergehenden Kapitel.

Zuerst machen wir den Leser dabei mit dem Feld der sogenannten locomotion robotics vertraut [11] und setzen es in Kontrast zu herkömmlichen Ansätzen der Robotik. Wir untersuchen das Verhalten von einfachen, zylindrisch oder sphärisch geformten, rollenden Robotern mit Hilfe der Simulationsumgebung LPZ-Robots [12] und zeigen auf, dass selbst minimale Kontrollmechanismen komplexe Bewegungsmuster erzeugen können. Das “Nervensystem” des Roboters besteht in diesem Fall aus einem einzelnen oder drei gekoppelten Neuronen, welche die aktuelle Position eines Aktors im Roboter erfassen. Die Aktivität der Neuronen wird, in Anlehnung an die neuronalen Netzwerke, die in **Kapitel 3** vorgestellt wurden, durch interne Plastizität und Kurzzeitplastizität beeinflusst. Die resultierenden Bewegungsformen entsprechen Grenzyklen und chaotischen Attraktoren im allumfassenden Phasenraum der internen und externen Variablen. Im Zuge unserer Untersuchungen haben wir heraus gefunden, dass die Interaktion mit anderen Robotern oder anderen Hindernissen zum Hin- und Herschalten zwischen verschiedenen parallel existierenden Attraktoren führt. Dies ist die bemerkenswerte Konsequenz der in **Kapitel 2** diskutierten Multistabilität.

Das dynamische Verhalten der Roboter ist durch die lokalen Instabilitäten, welche von der Dynamik der Neuronen erzeugt werden, selbst-organisiert, solange es nicht durch eine Top-down-Kontrolle übersteuert wird [12]. Da die Fortbewegung als solche ohne diese sensomotorische Schleife gar nicht, oder nur mit sehr wenigen, intrinsisch vorhandenen Kontrollmustern ablaufen würde, können wir davon ausgehen, dass diese Roboter vollständig verkörpert (fully embodied) [13] sind. Wie in Abs. 4.2.1 beschrieben, schlagen wir vor, das Embodiment aus der Perspektive der Theorie dynamischer Systeme zu behandeln. Die Methode basiert auf dem Vergleich von tatsächlich beobachteten Fortbewegungsmustern und den Mustern, welche intern und ohne Umwelteinfluss erzeugt werden. Als Beispiel zeigen wir, dass ein tonnenförmiger Roboter auch dann noch in der Lage ist eine Rollbewegung zu generieren, wenn das isolierte Kontrollsystem des Aktors ohne äußere Einflüsse in einen stabilen Fixpunkt ohne interne Dynamik konvergieren würde [14]. Anhand der so entstehenden Rollbewegung, welche sich ebenfalls in der Dynamik des Kontrollsystems wiederfindet, lässt sich zeigen, wie grundlegend wichtig die Rückkopplung der Umgebung für die Entwicklung von komplexen Verhaltensmustern ist.

Die daraus entstehenden Fortbewegungsmuster entsprechen selbst-organisierten

---

Grenzyklen und chaotischen Attraktoren im kombinierten Phasenraum des Roboters, welcher sich aus den internen Variablen (Körper, Aktor, Kontrollsystem) und den externen, der Umgebung entsprechenden Variablen zusammensetzt. Es ist möglich diese Unterteilung zu machen, wenn die internen Variablen einen unabhängigen Unterraum des Systems aufspannen [15]. Die Dynamik des tonnenförmigen Roboters und des kugelförmigen Roboters sind unabhängig von deren Position oder Bewegungsrichtung. Trotzdem sind diese externen Variablen sehr wohl notwendig für die Interpretation des Verhaltens als allgemeine Fortbewegung des Roboters und insbesondere für das Erkundungsverhalten des Roboters. Aufgrund der globalen Symmetrien formen die entarteten Attraktoren ein Kontinuum in der Bewegungsebene. Im Falle dass mehrere koexistierende Attraktoren zugegen sind, also das System multi-stabil ist [5], entscheiden die Anfangsbedingungen der internen Variablen darüber, welcher Attraktor aus dem überlappendem Kontinuum ausgewählt wird und damit wie sich das Langzeitverhalten entwickelt.

Unsere Untersuchungen sind Bestandteil der seit Langem bestehenden Bemühungen, die Komplexität in den Kontrollsystemen für robotische Fortbewegung zu reduzieren [16, 17]. Dabei konzentrieren wir uns besonders auf die Ausbildung von Attraktoren im kombinierten Phasenraum aus Roboter und Umgebung. Diese Herangehensweise hat sich als erfolgreich herausgestellt, was das Verständnis von verschiedenen Fortbewegungsarten als grenzyklische Attraktoren [18] angeht. Dennoch sind wir davon überzeugt, dass eine systematische Theorie der robotischen Fortbewegung auf Grundlage der Theorie dynamischer Systeme einen signifikanten Beitrag sowohl für die Entwicklung als auch für die Realisierung selbständiger Roboter liefern würde. Die Arbeit, welche wir in diesem Kapitel vorstellen, kann als ein erster Schritt in diese Richtung verstanden werden.

Zum Schluss dieser Dissertation werfen wir einen Blick auf die Herausforderungen und Beschränkungen der aktuellen Forschung im Gebiet der komplexen dynamischen Systeme. Die hier vorgestellten wissenschaftlichen Beiträge zielen in diesem Zusammenhang darauf ab, eine Brücke zwischen den wohl bekannten, niedrigdimensionalen dynamischen Systemen und komplexeren und höherdimensionalen Systemen, wie sie Anwendung in den Neurowissenschaften oder der Robotik finden, zu schlagen. Zu guter Letzt werfen wir drei ambitionierte Fragen auf, aus welchen sich Möglichkeiten für zukünftige Forschungsrichtungen ableiten lassen.



# Abstract

The extension of the scope of dynamical systems theory to the study of complex high-dimensional systems, would contribute greatly to the understanding of the versatile dynamical behavior of various physical, biological, or economical phenomenon. Here, we present novel models, methods and applications of dynamical systems, our results being embedded in the long standing effort of bridging the gap between the theory of simple (low dimensional) and complex (high dimensional) nonlinear systems.

We begin with a general introduction to the field of dynamical systems theory, providing an overview of the basic concepts and the mathematical formalism, which is consistently employed throughout the following chapters. In the second part of **Chapter 1** we also discuss some more recent developments of the field, such as transient-state dynamics, multistability and degenerate attractors, which, being in the forefront of dynamical systems research, are exploited further in the present thesis.

In **Chapter 2**, we propose a novel class of prototype dynamical systems, formally corresponding to generalized Liénard-type equations with arbitrary dimensions, which allows for the construction of coexisting attractors in the phase space. In the endeavor of creating multistable systems in a controlled manner, we rely on two essential components: a potential function characterized by a certain number of local minima, and a generalized friction term (playing the role of drag in the system), being in turn functionally dependent exclusively on the potential. For a purely dissipative friction function, the minima of the potential correspond to stable fixpoints of the system, while energy uptake in their neighborhood leads to the generation of stable limit cycles. Changing gradually the area of dissipative and anti-dissipative regions a chaotic attractor is created, with geometrical properties which are reflecting the destabilized limit cycles.

To construct attractors at specified locations in the phase space, we introduce furthermore a generalized potential function, with a predefined number of local minima. Setting then both the height and the positions of minima one may place fixpoint, limit-cycle and chaotic attractors at arbitrary spatial coordinates. Considering 2- and 4-dimensional versions of the prototype dynamical system, in **Chapter 2**, we demonstrate that cascades of limit-cycle bifurcations can be generated in a

controlled manner. Finally, we speculate that adding an additional slow dynamics to the location or shape of minima, the metadynamics of attractors may also be investigated.

Following the idea of coupling slow variables to multistable systems, in **Chapter 3**, we investigate attractor neural networks with dynamic synapses. After discussing the role of well-defined activity states, we provide a brief overview of the mathematical models employed in the field. Considering clique-encoding attractor neural networks, with coexisting stable fixpoints of active cliques of excitatory neurons, we study the effect of short-term synaptic plasticity (STSP) on the network dynamics.

We show that the dynamical change of connection strengths, modeled here by the rules of STSP, may destabilize the fixpoint attractors. The generated oscillatory behavior, referred to as transient-state dynamics, is characterized by relatively long plateaus of activity. Studying first a four-neuron symmetric network, followed by larger networks of random excitatory connection topology, we show that the neural activity of transient states corresponds to the activity of the former attractor states without STSP, their duration being, however, determined by the time scales of plasticity.

In **Chapter 4** we introduce the field of locomotion robophysics, engaged in a quest for revealing general principles in the motion of cognitive artificial agents situated in a complex environment. We consider simple barrel- and sphere-shaped rolling robots, their motion being generated indirectly, via damped-spring actuators moving weights along internally fixed axes. The actuator of the barrel robot is controlled by a single proprioceptual neuron with internal adaption, while in case of the spherical robot, a network of three neurons is used with dynamic inhibitory connections governed by STSP.

The considered robots are fully embodied due to the feedback mechanisms of the closed-loop control scheme. We show that regular and chaotic locomotion patterns emerge even in case when no dynamics is expected in the subsystem of the isolated controllers. The observed set of motion patterns are self-organized, corresponding to stable limit-cycle and chaotic attractors in the combined phase space of controller, body and environment, being additionally degenerate in the plane of locomotion. The employment of this attractor picture allows for the interpretation of interactions with obstacles and other agents in terms of switching between coexisting states of the system.

The thesis is concluded with an outlook on the frontiers and challenges of present day research in complex dynamical systems, raising also a few ambitious questions to outline possible research directions for the future.

# Chapter 1

## General Background

*The next great era of awakening of human intellect may well produce a method of understanding the qualitative content of equations.*  
Richard Feynman. The Feynman Lectures on Physics (1963)

To understand the dynamical behavior of complex systems, described by a large number of variables, one has to extend the scope of dynamical systems theory, dealing typically with low dimensional systems [1]. In this thesis we argue that the development of new concepts and methods may allow to unveil simple dynamical principles behind complexity.

Dynamical systems approaches have been recently proposed to be a key tool in gaining a deeper understanding of diverse complex phenomena such as the activity patterns emerging in the brain [2, 3] or self-organized embodiment of biologically inspired robots [11, 19]. Further typical areas of study include complex networks [4] in general, the dynamics of recurrent neural networks [20] in particular, or the control of multistability [5] with a wide range of applications in different disciplines of science [6].

In this chapter we briefly discuss the basic concepts and methods of the field of dynamical systems, introducing the standard notation, which is then consistently used throughout the following chapters of the thesis. We start with the mathematical formalism we build on, when investigating the dynamics of more complex systems, such as neural networks and robots. This involves the introduction of concepts like flows and maps, attractors and their stability, and bifurcations. That is followed by some more recent results, concepts and methods suggested for the study of complex dynamical systems, discussing the importance of multistability, degenerate attractors, and transient-state dynamics.

## 1.1 On dynamical systems

The methods and concepts of dynamical systems theory provide an effective toolkit and a consistent language to investigate the behavior of various, typically low dimensional systems, characterized by variables, which may describe physical, chemical, biological, social or even economical quantities [21].

Complex systems are often modeled by nonlinear equations of motion, which are typically impossible to solve analytically. A dynamical systems description allows, however, for the characterization of the long term dynamical behavior (in terms of attractors) even for randomly chosen initial conditions, the understanding of the qualitative change of dynamics (due to bifurcations) when varying the control parameters, or determining the time-span a system remains predictable despite of the underlying locally irregular (chaotic) behavior, just to mention a few [1, 21].

For deterministic systems, the equations of motion uniquely determine the present state of a system only from the past states. However, dynamical processes in complex systems might also be subjected to the effects of noise. The presence of small noise levels typically results in the blurring of trajectories of deterministic dynamical systems, generally without a qualitative change of behavior. Stochastic, or noisy dynamical systems can show, nevertheless, non-trivial effects, such as transitions between stable deterministic states, or the excitation of otherwise damped internal oscillations [1]. Here, in this thesis, we mainly focus on deterministic systems, mentioning, however, the implications of potential noise sources where it is applicable.

### 1.1.1 ODEs and maps

Formally speaking, dynamical systems provide a mathematical description of the evolution of a systems' state forward in time [22]. Time here can be regarded both as a continuous  $t \in \mathbb{R}$  or discrete  $t \in \mathbb{N}$  variable. The state of the system is defined by the position of the phase point  $\mathbf{x} \in \mathbb{R}^n$  in phase space (also called state space), with  $n$  denoting the number of dimensions, spanned by the variables of the dynamical system,  $\mathbf{x} = (x_1, x_2, \dots, x_n)$ . Mathematically, the time evolution of the state, denoted by  $\mathbf{x}(t)$  or  $\mathbf{x}_t$  for continuous and discrete time systems respectively, can be described in two different ways.

*Continuous time systems:* are expressed in terms of sets of first order, ordinary differential equations (ODEs):

$$\dot{\mathbf{x}} = \mathbf{f}(\mathbf{x}), \quad \mathbf{f} = (f_1, \dots, f_n), \quad (1.1)$$

where the dot operator is denoting time derivative,  $\dot{\mathbf{x}} = d\mathbf{x}/dt$ , and  $\mathbf{f}$  is referred to as the right-hand-side (RHS) of the differential equation, with  $f_i : \mathbb{R}^n \rightarrow \mathbb{R}$ . If the system is deterministic a given initial condition  $\mathbf{x}(0)$  uniquely determines the

complete time evolution of the state, referred to as an orbit or a trajectory, tracing out a one-dimensional curve in the phase space of the system. The dynamics of the phase space is often termed as the flow, since it is analogous to the behavior of particles in the flow of some fluid.

*Discrete time systems:* a set of functions map the system's state between consecutive time-steps  $t$  and  $t + 1$ :

$$\mathbf{x}_{t+1} = \mathbf{m}(\mathbf{x}_t), \quad \mathbf{m} = (m_1, \dots, m_n). \quad (1.2)$$

where  $\mathbf{m}$  is called the map, with  $m_i : \mathbb{R}^n \rightarrow \mathbb{R}$ . The orbit generated by a map corresponds to a sequence of states,  $\mathbf{x}_0, \mathbf{x}_1, \mathbf{x}_2, \dots$ , which typically jump discontinuously in the allowed space of states.

Continuous time dynamical systems can, in principle, always be reduced to discrete time maps. This is most often done by the technique called Poincaré surface section. For that we introduce an  $n_P = n - 1$  dimensional hyperplane (typically defined by a constant  $x_i^P = c$  with  $c \in \mathbb{R}$ ), and register the coordinates  $\hat{\mathbf{x}}_t \in \mathbb{R}^{n_P}$  where the trajectory intersects the plane. Since consecutive intersection points are uniquely determined by the flow (1.1), we get an equivalent map,  $\hat{\mathbf{x}}_{t+1} = \hat{\mathbf{m}}(\hat{\mathbf{x}}_t)$ , termed as Poincaré map [22]. Another way to create a map is to sample stroboscopically the trajectory at times  $t_k = t + kT$  for  $k = 0, 1, 2, \dots$ , with a conveniently chosen sampling rate  $T$ . Denoting  $\mathbf{x}_t = \mathbf{x}(t_k)$ , we can define again a map of consecutive snapshot states. The usage of stroboscopic maps is more useful for the study of periodically driven motion [23].

*Autonomous systems:* do not explicitly depend on time, hence the law for future states is written in terms of the present state [24]. Formally this means that the time does not appear explicitly in the right-hand-side of the ODE (1.1) or of the map (1.2) defining the dynamics of the system.

*Nonautonomous systems:* correspond generally to driven or modulated systems, for which the RHS of the equations of motion are time dependent. Therefore, the actual state of the system, unlike for the autonomous case, depends on both the actual and the initial times,  $t$  and  $t_0$ , respectively, and not just on the elapsed time since starting  $t - t_0$  [25]. Note that this distinction is somewhat artificial, since any nonautonomous system, for which time  $t$  explicitly appears on the RHS of the ODE or map, respectively, can be written as an autonomous system by defining a new independent variable, describing the progress of time. Nevertheless, over the recent years, it has developed into a highly active research field, recognizably distinct from that of the classical autonomous systems [26].

Since most of the systems we deal with in the thesis are continuous time autonomous systems, we will use in the followings the formalism of ODEs introduced above, discussing however important properties of maps as well, where it is necessary.

### 1.1.2 Phase space contraction

For most dynamical systems of interest, trajectories do not evolve unrestrictedly towards infinity, but stay in a bounded region of the phase space, even if that is theoretically unlimited. It is then a natural question to ask how the phase space volume of an ensemble of state point “particles” evolves under the flow. For bounded trajectories one would expect non-expanding phase spaces, viz. always keeping the state points together.

To quantify the rate at which a given phase space volume is changing in a continuous time system, one can calculate the time derivative of the volume  $V(t)$  of an infinitesimal hypercube around point  $\mathbf{x}$ , subject to the flow  $\mathbf{f}$ . It is easy to show (see Sec. A.1 in the Appendix) that the phase space contraction rate  $\sigma(\mathbf{x})$  of continuous time systems is given by the divergence of the RHS function [22]:

$$\sigma(\mathbf{x}) = \nabla \cdot \mathbf{f}(\mathbf{x}) = \text{tr}(\mathbf{J}_{\mathbf{f}}(\mathbf{x})), \quad \frac{dV(t)}{dt} = \sigma(\mathbf{x})V(t), \quad (1.3)$$

which is equivalent to the trace of the Jacobian matrix of the flow  $\mathbf{f}$ :

$$\mathbf{J}_{\mathbf{f}} = \frac{\partial(f_1, \dots, f_n)}{\partial(x_1, \dots, x_n)} = \frac{\partial \mathbf{f}}{\partial \mathbf{x}}, \quad (\mathbf{J}_{\mathbf{f}}(\mathbf{x}))_{ij} = \frac{\partial f_i(\mathbf{x})}{\partial x_j}. \quad (1.4)$$

A negative contraction rate  $\sigma(\mathbf{x}) < 0$  corresponds to the exponential shrinking of the phase space volume  $V$ , while a change of sign, i. e.  $\sigma(\mathbf{x}) > 0$ , refers to the (exponential) expansion of  $V$ .

In case of maps a given phase space volume  $V_t$  at time  $t$  might change significantly by step  $t + 1$  within a single iteration. Considering a map  $\mathbf{m}$ , as defined by Eq. (1.2), the Jacobian matrix

$$\mathbf{J}_{\mathbf{m}} = \frac{\partial(m_1, \dots, m_n)}{\partial(x_1, \dots, x_n)} = \frac{\partial \mathbf{m}}{\partial \mathbf{x}}, \quad (\mathbf{J}_{\mathbf{m}}(\mathbf{x}))_{ij} = \frac{\partial m_i(\mathbf{x})}{\partial x_j}, \quad (1.5)$$

describes the how points move close to  $\mathbf{x}$ . More precisely, the absolute value of the Jacobian’s determinant gives the factor by which an infinitesimal volume shrinks or expands [22]:

$$\sigma(\mathbf{x}) = |\det(\mathbf{J}_{\mathbf{m}}(\mathbf{x}))|, \quad V_{t+1} = \sigma(\mathbf{x})V_t, \quad (1.6)$$

with  $\sigma(\mathbf{x})$  denoting again the contraction rate. A  $\sigma(\mathbf{x}) < 1$  corresponds to the local contraction, and  $\sigma(\mathbf{x}) > 1$  indicates the expansion of phase space.

In general the contraction rate  $\sigma(\mathbf{x})$  is a local quantity. There are, however, systems for which every point of the phase space is contracting/expanding due to the flow. As an example we consider the dynamics of a particle of unit mass:

$$\ddot{\mathbf{x}} + \gamma \dot{\mathbf{x}} + \nabla V(\mathbf{x}) = 0, \quad \begin{aligned} \dot{\mathbf{x}} &= \mathbf{v} \\ \dot{\mathbf{v}} &= -\gamma \mathbf{v} - \nabla V(\mathbf{x}) \end{aligned} \quad (1.7)$$

with  $\mathbf{x} = (x_1, x_2, x_3)$ , in the presence of velocity dependent friction forces,  $-\gamma\mathbf{v}$ , in the potential  $V(\mathbf{x})$ . The phase space contraction rate:

$$\sigma = \nabla \cdot \mathbf{f}(\mathbf{x}) = -\gamma, \quad (1.8)$$

is determined solely by the friction coefficient  $\gamma$ , and it can be considered, hence, the generalization of the change of the system's total energy:

$$\dot{E} = -\gamma|\mathbf{v}|^2, \quad E = \frac{|\mathbf{v}|^2}{2} + V(\mathbf{x}). \quad (1.9)$$

Based on this example, dynamical systems can be categorized according to the nature of the phase space contraction.

*Dissipative systems:* have a contracting phase space,  $\sigma(\mathbf{x}) < 0$ . For mechanical systems like Eq. (1.7) this corresponds to the presence of a friction force with  $\gamma > 0$  in the equations of motion, leading to the loss of total energy via dissipation,  $\dot{E} < 0$ . An overall contracting phase space might seem to be very restrictive in terms of how volumes of initial conditions are shaped via time evolution. It turns out, however, that contraction does not preclude the presence of stretching mechanisms, allowing for rather strangely shaped geometrical objects. This is possible if the stretching experienced in one direction is compensated by an even stronger contraction perpendicular to it [23].

*Conservative systems:* are corresponding to Hamiltonian systems, with  $\sigma(\mathbf{x}) = 0$ , characterized by constants of motion, where the loss of energy can be neglected. Returning to the example of the particle with unit mass, see Eq. (1.7), the frictionless case with  $\gamma = 0$  results in the conservation of energy,  $\dot{E} = 0$  and  $E = \text{const}$ .

*Expanding systems:* have a positive phase space contraction rate, i. e. expansion with  $\sigma(\mathbf{x}) > 0$ , everywhere in the phase space. That would correspond to an anti-dissipative friction term with  $\gamma < 0$ , due to energy uptake from some external source,  $\dot{E} > 0$ . Expanding systems have no bounded trajectories, leading to the infinite growth of the variables. Hence, in this case, most of the phenomena of general interest are only transient.

*Adaptive systems:* are characterized by the coexistence of dissipative and anti-dissipative regions of phase space [1]. Generalizing now the mechanical system (1.7), introducing a position dependent parameter  $\gamma = \gamma(\mathbf{x})$ , the sign of  $\gamma$  would regulate, hence, the different regions of phase space contraction/expansion. Adaptive systems turn out to be the most general case of complex systems, allowing for phases of energy dissipation, and also for energy uptake from the environment. In **Chapter 2** we introduce a new class of adaptive systems, similar to (1.7) but with a generalized mechanical potential, where the regions of energy uptake and dissipation can be controlled directly by changing the parameters.

### 1.1.3 Attractors

Considering the case of dissipative dynamical systems, with an overall contracting phase space, one could wonder where all the trajectories go as they are evolving under the flow. Due to the nonlinear nature of the functions involved in the dynamical description of many complex systems, a complete analytical treatment of the evolution of trajectories is often impossible. The study of the asymptotic behavior of typical orbits allows, however, for a geometrical characterization of the long term dynamics, leading to the concept of attractors.

*Attractors or attracting sets:* are bounded subsets of the phase space, to which many initial conditions evolve asymptotically as time increases (line and plane attractors are discussed separately in the context of degenerate attractors). The attractors are invariant under forward time translation, i. e. under the effect of the flow or the map [22]. This means that the evolution of all the points belonging to it, viz the attracting set, yields the same attractor. The union of all orbits which converge towards the attracting set is termed as the basin of attraction or attraction domain. A finite basin of attraction around the attractor affords dynamical systems to be stable against small perturbations. The phase point, already settled on the attractor, would deviate from it temporarily when noise, or a small perturbation is present, returning afterwards and staying on it as a result of forward invariance.

Dissipative systems, in contrast to conservative and expanding ones, are characterized by the presence of attractors in the phase space. The phase space of adaptive systems, though it is not as obvious as in the other cases, might also possess attractors. These attracting sets may be embedded in locally dissipative phase space regions, or more interestingly, may be stretched over different contracting and expanding zones as extended geometrical objects. In the latter case a self-organized energy balance is achieved by visiting both regions of energy uptake and dissipation [1, 7].

According to the above definitions, trajectories starting from initial conditions in the attraction domain converge to the attractor, tracing out its geometrical structure. Not all invariant sets are, however, attractors. Trajectories started exactly on non-attracting invariant sets remain “trapped” there, but deviate fast from them even under small perturbations. Other orbits with typical initial conditions may only trace them out temporarily, being repelled far away in the phase space. Since the variation of the system’s parameters can lead to the destabilization of attractors, it is important to study the regions of stability in the parameter space. It is interesting to note that close to the border of stability, even non-attracting invariant sets might play an important role in the behavior of complex adaptive dynamical systems, like agents exploring their environment [14, 15]. This aspect of the role of attractors for robotic behavior is emphasized in Sec. 4.3 of **Chapter 4**.

Attractors may be simple geometrical objects, such as points, lines and surfaces,

or more complicated fractal structures. One typically differentiates between four main types of attractors, in terms of their geometry. In the following a brief definition is given of the attractor types, together with the introduction of the formalism used for stability analysis.

*Fixpoints or equilibrium points:* are distinct invariant points of the phase space, denoted typically by  $\mathbf{x}^*$ , where the flow vanishes,  $\mathbf{f}(\mathbf{x}^*) = 0$ , or equivalently for maps, points, which are mapped into themselves,  $\mathbf{x}^* = \mathbf{m}(\mathbf{x}^*)$ . Hence, by definition, fixpoints are sets of dimension zero. To investigate the stability, the flow can be linearized at  $\mathbf{x} = \mathbf{x}^* + \delta\mathbf{x}$  with  $|\delta\mathbf{x}| \rightarrow 0$ :

$$\dot{\mathbf{x}} = \mathbf{f}(\mathbf{x}) \approx \mathbf{f}(\mathbf{x}^*) + \mathbf{J}_f(\mathbf{x}^*)\delta\mathbf{x} + \dots, \quad (1.10)$$

where  $\mathbf{J}_f(\mathbf{x}^*)$  denotes the Jacobian matrix, as defined by (1.4), evaluated at  $\mathbf{x}^*$ . In the first order approximation the time evolution of small perturbations of the fixpoint state is simply given by the solution of a linear ODE:

$$\dot{\delta\mathbf{x}} = \mathbf{J}_f(\mathbf{x}^*)\delta\mathbf{x}, \quad \delta\mathbf{x}(t) = \sum_{i=1}^n c_i \mathbf{v}_i e^{\lambda_i t}, \quad (1.11)$$

where  $\mathbf{v}_i \in \mathbb{C}^n$  and  $\lambda_i \in \mathbb{C}$  are respectively the eigenvectors and eigenvalues of the constant Jacobian  $\mathbf{J}_f(\mathbf{x}^*)$ , while the coefficients  $c_i$  are determined by the initial conditions. When all the eigenvalues have negative real parts,  $\text{Re}(\lambda_i) < 0$  for  $i = 1, \dots, n$ , the perturbation vanishes asymptotically,  $\delta\mathbf{x} \rightarrow 0$ . These fixpoints are called stable node/focus, when all eigenvalues are real/at least one eigenvalue is complex, respectively. However, due to the exponential time dependence, the existence of a single eigenvalue with positive real part,  $\text{Re}(\lambda_1) > 0$ , results in the growth of infinitesimal perturbations, making the fixpoint unstable. Fixpoints with both positive and negative eigenvalues are called of saddle type. The stability analysis of equilibrium points of maps is analogous to the one presented here, and it is briefly discussed in the next paragraph.

*Limit cycles and periodic points:* describe sustained periodic motions, characterized by a certain period  $T$ . In continuous time dynamical systems, limit cycles are isolated periodic orbits, defined by  $\mathbf{x}(t) = \mathbf{x}(t + T)$ , a set of dimension one, embedded in the  $n \geq 2$  dimensional phase space. Since limit cycles are typically closed orbits, using the Poincaré section technique presented in Sec. 1.1.1, but only registering intersection points in one direction, the periodic attractor reduces to a fixpoint  $\mathbf{x}_{t+1}^* = \mathbf{m}(\mathbf{x}_t^*) = \mathbf{x}_t^*$ , with  $\mathbf{x}_t^* \in \mathbb{R}^{n_P}$ , of the  $n_P = n - 1$  dimensional Poincaré map (dropping the hat notation,  $\mathbf{m} = \hat{\mathbf{m}}$ , for simplicity). The stability of the limit cycle hence can also be studied in terms of fixpoints of maps, using a linearization procedure analogous to Eqs. (1.10) and (1.11), but expressing the time evolution of the perturbation  $\delta\mathbf{x}_t \in \mathbb{R}^{n_P}$  as a linear mapping, with  $|\delta\mathbf{x}_0| \rightarrow 0$ :

$$\delta\mathbf{x}_{t+1} = \mathbf{J}_m(\mathbf{x}^*)\delta\mathbf{x}_t, \quad \delta\mathbf{x}_t = \sum_{i=1}^{n_P} c_i \mathbf{v}_i \lambda_i^t. \quad (1.12)$$

The eigenvectors and eigenvalues  $\mathbf{v}_i \in \mathbb{C}^{n_P}$  and  $\lambda_i \in \mathbb{C}$  respectively, correspond to the constant Jacobian  $\mathbf{J}_m(\mathbf{x}^*)$  (see Eq. 1.5) of the Poincaré map for point  $\mathbf{x}^*$ . The coefficients  $c_i$  are determined from the initial conditions. Fixpoints, and hence limit cycles, with all  $|\lambda_i| < 1$  are called stable. Eigenvalues  $|\lambda_i| > 1$  lead to deviations from the unstable or saddle type equilibrium states. The eigenvalues arising from the linearization of Poincaré maps are sometimes also termed as (Floquet) multipliers [24].

In case of multiple intersection points, viz. a finite number of points visited in a sequence,  $\mathbf{x}_t^* \rightarrow \mathbf{x}_{t+1}^* \rightarrow \dots \rightarrow \mathbf{x}_{t+p}^* = \mathbf{x}_t^*$ , we get a period  $p > 1$  orbit, which is in turn an equilibrium point of the  $p$ th iterate Poincaré map,  $\mathbf{x}_{t+p}^* = \mathbf{m}^{(p)}(\mathbf{x}_t^*) = \mathbf{x}_t^*$ . The Jacobian matrix of the map  $\mathbf{m}^{(p)}$  can now be expressed using the generalized chain rule as a product of the original Jacobians  $\mathbf{J}_m$ ,

$$\mathbf{J}_{\mathbf{m}^{(p)}}(\mathbf{x}_t^*) = \mathbf{J}_m(\mathbf{x}_{t+p-1}^*) \cdot \mathbf{J}_m(\mathbf{x}_{t+p-2}^*) \cdot \dots \cdot \mathbf{J}_m(\mathbf{x}_{t+1}^*) \cdot \mathbf{J}_m(\mathbf{x}_t^*), \quad (1.13)$$

evaluated at the  $p$  points of the orbit. This means that the stability of the limit cycle is a property of the periodic orbit as whole, not only of individual points [24]. Finally, we would like to stress that, although we have discussed above the stability of Poincaré maps, the stability arguments apply to maps in general as well.

Saddle type fixpoints or limit cycles of flows (or respectively of maps), are not stable, i. e. by using typical initial conditions they can never be approached asymptotically, but only transiently. There are, however, smooth manifolds of zero phase space volume, defined as the set of points  $\mathbf{x}$  which evolved forward/backward under the flow (map) approach the saddle, called unstable/stable manifolds. Since these manifolds have no volume extension, typical initial conditions do not start from them [23]. Close to the fixpoints and limit cycles the stable/unstable manifolds are tangent to subspaces spanned by the eigenvectors corresponding to the eigenvalues with negative/positive real parts, respectively [24].

*Torus attractors:* are characterized by more than one frequency, which form irrational, i. e. incommensurate, fractions. Therefore, the orbit of the flow can not close in itself, creating an invariant torus in the  $n \geq 3$  dimensional phase space. The dynamics on a torus is called quasiperiodic (it is not strictly periodic). While the power spectrum of periodic motion is characterized by delta peaks at the integer multiples of the fundamental frequency  $\omega_0 = 2\pi/T$ , in case of tori we find peaks at several different fundamental frequencies which are incommensurate [22]. Quasiperiodic motion plays a central role in Hamiltonian systems, occurring frequently in case of dissipative or adaptive dynamical systems as well.

The attractors discussed so far are simple geometrical structures: single points as fixpoints (sets of dimension  $D = 0$ ), closed curves as limit cycles (sets of dimension  $D = 1$ ), or closed ( $D < n$  dimensional) surfaces. It turns out, however, that invariant sets forming the attractors may also have self-similar fractal struc-

tures, called strange attractors, which are characterized by a non-integer fractal dimension,  $D \notin \mathbb{N}$ . Fractal structures, a term introduced by Mandelbrot [27], have strongly ramified surfaces and perimeters. Their surface area or perimeter length is increasing with resolution, hence one can not characterize their dimensionality in the traditional way. The fractal dimension provides a straightforward generalization for the concept of dimension by quantifying how the result of the measurement is scaling with resolution, and allowing fractional and irrational values as well [23]. The box-counting method, a relatively simple method to compute the fractal dimension of strange attractors emerging in dynamical systems is described briefly in the Appendix A.2.

*Chaotic attractors:* are invariant sets of complex, fractal structures, on which a never recurring, unpredictable sustained motion takes place. The fractal structure of the attractors is a result of the nonlinear equations of motion, which generate irregular dynamics, exhibiting sensitive dependence on initial conditions. Small changes or perturbations of the current trajectory lead to significantly different future states, making the prediction of the behavior impossible in the presence of any numerical or measurement error. This unpredictability manifests itself in the exponential divergence of perturbations (in a similar manner to perturbations close to unstable fixpoints, see Eq. 1.11) characterized by the maximal Lyapunov exponent  $\lambda_m$  of the system. The largest (maximal) Lyapunov exponent is defined in the limit of infinite time, which in the continuous time case reads as:

$$\lambda_m = \lim_{t \rightarrow \infty} \frac{1}{t} \ln \frac{|\delta \mathbf{x}(t)|}{|\delta \mathbf{x}(0)|}, \quad (1.14)$$

describing the logarithmic growth rate of initially infinitesimal perturbations  $\delta \mathbf{x}(t)$ , with  $\delta \mathbf{x}(0) \rightarrow 0$ . Note that  $\lambda_m$  is independent of the starting point  $\mathbf{x}$ , and also of the direction of the initial perturbation  $\delta \mathbf{x}(0)$  for all typical trajectories, hence it is a quantity characterizing the attractor itself. The attractor is defined to be chaotic if the maximal Lyapunov exponent is positive,  $\lambda_m > 0$  [22]. As we have seen in case of simple attractors, the stability of an orbit (on the attractor) is determined by the eigenvalues of the Jacobian matrix evaluated at the fixpoints or at the periodic points (see Eqs. (1.11), (1.13)). These quantities can be generalized for chaotic trajectories as well, by studying the exponential divergence of perturbations along non-typical, orthogonal initial directions  $\delta \mathbf{x}(0)$  using Eq. (1.14). This leads to the Lyapunov spectrum,  $\lambda_1 > \lambda_2 > \dots > \lambda_n$ , consisting of  $n$  Lyapunov exponents, with the largest one being equivalent to  $\lambda_m = \lambda_1$ . One can define the Lyapunov exponents  $\lambda_k$  analogously to Eq. (1.14) as discussed in Appendix B.3.

The limit  $t \rightarrow \infty$  used in Eq. (1.14) is rather impractical for the numerical computation of the largest Lyapunov exponent  $\lambda_m$ , since using finite initial displacements  $\delta \mathbf{x}(0)$ , the exponential growth of perturbations  $\delta \mathbf{x}(t)$  can only be observed over finite times, before reaching distances comparable to the size of the attractor. As a more practical approach one can consider instead an averaging over pairs of

trajectories  $\mathbf{x}_{1,2}(t)$  choosing initial conditions distributed on the attractor according to the natural distribution [23]. The maximal Lyapunov exponent can then be determined from the initial slope of the logarithmic distance,

$$\langle \ln |\mathbf{x}_1(t) - \mathbf{x}_2(t)| \rangle \approx \lambda_m t + \ln \delta_{12}, \quad (1.15)$$

averaged over many trajectory pairs  $\mathbf{x}_{1,2}(t)$  of very small initial separation  $\delta_{12} = |\mathbf{x}_1(0) - \mathbf{x}_2(0)| \ll 1$ . A good averaging over initial conditions of pairs of trajectories can be achieved by using a very long reference trajectory  $\mathbf{x}_1(t)$  and “pushing-back” the second orbit  $\mathbf{x}_2(t)$  to a suitably small initial distance  $\delta_{12}$ , whenever they get separated to a distance comparable to the size of the attractor [23]. There are many, more sophisticated methods in the chaos literature for determining the largest Lyapunov exponent for maps and flows, or for computing the full Lyapunov spectrum (for an overview see e. g. [28]).

Chaotic dynamics is defined as unpredictable due to the sensitive dependence on initial conditions. There are however partially predictable chaotic (PPC) attractors, characterized by positive Lyapunov exponents, nevertheless allowing for a rather high degree of predictability for exceedingly long time-scales [29]. The generated time-series can be hence sometimes very difficult to distinguish from a periodic behavior. In another work [29] (not discussed here in detail), we have introduced a novel method as a possible resolution of this problem, namely for distinguishing chaotic attractors and limit cycles, and discriminating further between strong and partially predictable chaos. Furthermore, in Sec. 4.3 of **Chapter 4** we present an example of PPC found in the locomotion of rolling robots, which allows for a smooth exploration of complex environments.

Finally, for investigating the dynamics of complex systems, it is often more convenient to change from one coordinate system to another. This is plausible since fixpoints of a dynamical system do not change their stability upon general coordinate transformations. More precisely, the eigenvalues of the Jacobians,  $\mathbf{J}_f$  or  $\mathbf{J}_m$ , characterizing the stability of fixpoints and periodic points, are invariant under these transformations [24]. As a consequence of that one can freely choose the coordinate system, viz the preferred variables to model a specific behavior. This is however not true for general points in the phase space. Thus, the volume contraction in some region of the phase space, characterized by the sum of eigenvalues, i. e. the trace of the Jacobian (see Eq. (1.3) in Sec. 1.1.2), can depend on the chosen coordinate system. In Appendix A.4 we provide a proof, discussing both continuous and discrete time dynamical systems.

### 1.1.4 Degenerate attractors and multistability

*Multistability:* the coexistence of multiple attractors offers a great flexibility for modeling complex dynamical behavior. Multiple stable states allow for switching between attractors as a result of controlled or noisy inputs, an indispensable property, to give a few examples, for modeling the survival of species in the ecosystem,

for implementing memory in neural networks, for understanding climate dynamics or the dynamical processes in social-political systems (see [5] for a recent review). Multistable systems may generally be very sensitive to perturbations [30], or to the change of initial conditions [31] and system parameters [32]. This sensitivity might be particularly pronounced in case of attractors with small basins of attraction, leading often to sudden switches to unexpected or previously unknown attractors. Such jumps can generate catastrophic events, such as climate changes, diseases or financial crises [33]. In Sec. 2.2 of **Chapter 2** we introduce a design procedure for constructing multistable dynamical systems by placing fixpoint, limit cycle or even chaotic attractors to predefined positions in the phase space.

In case of the most common dynamical systems there exist unstable manifolds, emanating from saddle fixpoints, which attract other trajectories and drive them to the corresponding attractors. The presence of these manifolds allows for a relatively easy identification of the existing attractors of a system. It has been shown, however, that multistability is often connected with the occurrence of so called hidden attractors, with attraction domains which are not close to any saddle points [34]. Therefore, hidden attractors typically have very small basins of attraction, making them difficult to reveal using traditional numerical approaches [35].

The size of the attraction domain is hence an important quantity, providing information about the probability of landing on one of the multiple attractors when random initial conditions are considered [36]. Following this idea, the basin stability concept has been proposed as a complementary quantity to characterize stability of states against arbitrary (possibly non-small) perturbations [37]. A similar method estimating the weakest perturbation capable of disrupting the dynamics is the stability threshold approach [38]. Using these quantities alongside with the traditional linear stability analysis, might enable a deeper understanding of many puzzling dynamical behavior observed in complex dynamical systems.

*Degenerate attractors:* form a continuum in the phase space of the dynamical systems [39, 40]. In the traditional view of classical dynamical systems theory, attractors are bounded geometrical objects, confined within a relatively restricted region of the phase space [21]. One can, nevertheless, also find even autonomous dynamical systems having a continuum of attractors, for which it takes an arbitrarily small perturbation to move within this manifold, also referred to as continuous attractors in the biological modeling literature [41].

One example of an attractor with infinite extension is provided by the problem of sliding on a slope [23]. This second order differential equation

$$\ddot{x} + \alpha\dot{x} + \frac{\partial V}{\partial x} = 0, \quad V(x) = -A \cos x - F_0 x, \quad (1.16)$$

describes sliding on a bumpy slope, which has an average tilting proportional to  $F_0$  and bumps of amplitude  $A$ . A skier is subject to a drag of  $-\alpha\dot{x}$ , making the sys-

tem dissipative (see the example of mechanical systems of this type in Sec. 1.1.2). There are an infinite number of stable and saddle fixpoints, but more interestingly a periodic attractor as well, corresponding to a stationary downhill sliding with a pulsating velocity [23]. The limit cycle is not a closed orbit, but it has a translational symmetry with respect to shifting by  $2\pi$ . This corresponds to a discrete degeneracy of the attractor. On the other hand, by the replacement  $x \rightarrow \varphi$  in Eq. (1.16) the degeneracy can be resolved, and one obtains the problem of a pendulum with a constant torque. Nonetheless, the viewpoint with the skier is rather instructive, since the concept of attractors with degeneracy turns out to be useful when studying locomotion in physical space. It allows for an insightful interpretation of interactions during physical motion in terms of the temporary abolition of translational symmetries [15]. This is discussed in more detail in **Chapter 4** in the context of robotic locomotion.

### 1.1.5 Transient states

In the previous sections we have discussed equilibria of dynamical systems of type  $\mathbf{f}(\mathbf{x}^*) = 0$ . The flow, by definition, vanishes at fixpoints, leading first to a slowing down, and ultimately to the complete stopping of the dynamics. There are, however, further special, non-fixpoint states in the phase space, i. e.  $\dot{\mathbf{x}} \neq 0$ , where we also see a remarkable slowing down of the flow.

*Transient states:* are distinct points or locally continuous manifolds in the phase space, attracting the flow only transiently. Trajectories approaching these manifolds hence slow down temporarily, staying in their close vicinity while moving gradually along them, which is then followed by a rapid jump to another quasi-stationary state [42]. The corresponding time-series representation of the dynamics is characterized by a sequential switching between steady-state plateaus, corresponding to well-defined states of the system [9].

Several models have been proposed, mainly in the context of cognitive and computational neuroscience, for generating transient-state dynamics. In the following paragraphs we discuss two classes of systems a bit more in detail, a system with external input and an autonomously active system. We note, nevertheless, that similar models are able to generate dynamic cluster patterns with coupled oscillators [43], or latching dynamics with infinite recursion [44].

Input information may in be encoded in dynamical systems via transient-state dynamics based on the winnerless competition principle [45]. The corresponding mathematical image of the phase space structure governing the dynamics relies on the existence of a stable heteroclinic channel, consisting of a chain of saddle (metastable) states which are connected by heteroclinic orbits. The sequence from the neighborhood of one saddle point to another one occurs, when the saddles are characterized by a single positive eigenvalue. Furthermore, the sequential dynam-

ics may be open ended in the sense that it does not repeat itself [46], or it may also be periodic, corresponding to a heteroclinic contour [47]. This general class of nonautonomous dynamical systems has been successful in modeling decision making processes [48] or the chunking dynamics required for short-term memory storage [49]. For a review of applications in modeling different brain functions see Ref. [50]. We note, however, that the heteroclinic connections, the building blocks of open heteroclinic channels and heteroclinic contours are not structurally stable, hence, these can only occur either for special parameter values or for systems of some specific form [3, 47].

Transient-state dynamics may also be produced in autonomous dynamical systems without heteroclinic connections, by coupling local, slowly adapting variables to a multistable system. In this view, transient-states correspond to slow manifolds or attractor ruins, generated from the original stable attractors, due to the coupling of the additional variables. In this context, clique encoding networks have been proposed as a possible model of attractor networks for generating transient-state behavior [9, 51]. The term clique encoding refers to the representation of information by the activity of a fully connected subgraph of nodes, which during the transient-state dynamics are sequentially reactivated. The dynamics of the slow variables may be defined in a top-down approach, via generating functionals encoding the information content of neural firing rates [52, 53]. Alternatively, biologically realistic synaptic plasticity rules may also account for the presence of slow local variables [51].

### 1.1.6 Bifurcations

The stability of solutions of ODEs and maps may change abruptly as a function of the control parameters. For example, when a fixpoint becomes unstable the behavior of the system changes suddenly, since the trajectory is either “pushed” to another attractor of the system or repelled to infinity, making the dynamics unbounded.

*Bifurcations:* of dynamical systems are qualitative changes of the dynamics produced by slowly varying parameters, which is accompanied by a topological change of the flow in the phase space [54]. Bifurcation theory studies and classifies these different phenomena arising from smooth shifts of the parameters, by analyzing the ubiquitous patterns of bifurcations. One may divide bifurcations in two principal classes [1]:

- Local bifurcations can be characterized by the changes in the local stability properties of fixpoints and limit cycles.
- Global bifurcations occur, on the other hand, when extended invariant sets of the system collide with each other, or with other equilibria of the phase space.

Bifurcations occur both in continuous and discrete-time systems. Here, we briefly discuss a subset of possible bifurcations of flows, the discrete-time counterparts being analogous to ones presented here.

*Saddle-node bifurcation:* is a local bifurcation in which two fixpoints collide and annihilate each other. The term saddle-node refers to the most often encountered case, involving the collision of a stable node and a saddle point. In a more general context it is also called a fold bifurcation. As it results in the complete disappearance of a previously stable state it often associated with hysteresis loops and catastrophic changes in the system [1].

*Pitchfork bifurcation:* the system transitions from one fixpoint to three fixpoints. In continuous-time dynamical systems pitchfork bifurcations occur generically in systems with symmetry. Depending on the stability of the fixpoints involved in the bifurcation, one may observe two distinct types. In case of supercritical pitchfork bifurcations a stable fixpoint is destabilized, while two stable symmetric states are created, generating a multistable system. In the subcritical case the opposite happens, an unstable fixpoint branching into one stable and two unstable ones.

*Hopf bifurcation:* is the birth of a periodic solution, when a focus type fixpoint switches its stability via a single pair of purely imaginary eigenvalues. In the supercritical case, a small amplitude stable limit cycle branches from the fixpoint, resulting in stable oscillations around the unstable equilibrium. In subcritical Hopf bifurcations a stable fixpoint is generated, surrounded by an unstable periodic orbit.

*Homoclinic bifurcation:* is a global bifurcation occurring when a limit cycle collides with a saddle point. When changing the bifurcation parameter the periodic orbit grows until it touches the saddle point, generating a homoclinic loop in which a stable and an unstable manifold unite in an orbit of infinite duration. When the parameter increases further, the limit cycle disappears completely.

*Period-doubling bifurcation:* corresponds to the creation or destruction of a limit cycle with twice the period of the original orbit, which is in turn destabilized. This local bifurcation of periodic orbits has a special status among other bifurcations, since it often occurs in a period doubling cascade as the parameter is varied further and further. The infinite sequence of doublings generally leads to the creation of a chaotic attractor, with a never recurring dynamics of infinite period. The chaotic attractor then consists of, among others, an infinite number of unstable limit cycles with different periods.

*Saddle-node of limit cycles:* is a local bifurcation in which two limit cycles collide and annihilate each other. Considering the Poincaré map of the periodic orbits, it reduces to a fold bifurcation of equilibria for maps.

In **Chapter 2** we introduce a prototype dynamical system which allows for the generation of all the here listed bifurcations. To demonstrate its versatile applicability, we present examples of Hopf, homoclinic and saddle-node bifurcations of limit cycles. Furthermore, we illustrate the (intermittent) dynamics of a chaotic attractor, generated via a sequence of period doublings.

### 1.1.7 Famous experimental setups

Finally, we present three examples of dynamical systems, which have also been investigated experimentally. Experimental physicists engaged in studying chaos in real systems often look for period-doubling cascades, since that is probably the most easily recognizable route to chaos for a dynamical system.

*Van der Pol oscillator:* was realized by Balthasar van der Pol with an electrical circuit, using active nonlinear circuit elements [55]. Using dimensionless variables, the system can be written as :

$$\ddot{x} - \epsilon(1 - x^2)\dot{x} + x = 0, \quad (1.17)$$

where the control parameter  $\epsilon$  is setting the frequency of the oscillations. In case of large damping with  $\epsilon \gg 1$  the system produces so called relaxation oscillations, characterized by a slow asymptotic behavior and sudden jumps to another value, which may be seen as a simple realization of transient-state dynamics.

*Duffing oscillator:* first studied in the experiment of Moon and Holmes [56], in which a steel beam is hanging vertically between two magnets fixed to the ground. Without external forces one would expect two stable states: the tip of the beam deflected toward one of the two magnets. A strain gauge attached to the beam is measuring the deflection, which is then converted to a time series signal. When the apparatus holding the steel beam is oscillating horizontally, one measures a rather irregular signal. A simple model explaining the irregular behavior was proposed, called nowadays the forced Duffing equation [22]:

$$\ddot{x} + \gamma\dot{x} + (x^3 - x) = g \sin(\omega t), \quad (1.18)$$

The first two terms correspond to the inertia, respectively velocity dependent friction, with friction coefficient  $\gamma > 0$ , while the third term represents the magnetic and elastic forces. The time dependent sinusoidal right-hand side corresponds to the shaking of the experimental setup with frequency  $\omega$ . When shaking is turned off,  $g = 0$ , there are two stable fixpoints  $x_{1,2}^* = \pm 1$ . The  $x^* = 0$  is an unstable equilibrium. Due to the dissipation the system tries to settle to one of fixpoints,  $x_{1,2}^* = \pm 1$ , however, due to the sinusoidal buffering it starts to oscillate aperiodically, leading to a chaotic behavior.

*Chua's circuit:* allows for many dynamical behavior seen in numerical simulations to be implemented in a rather simple manner [24]. It consist of an RLC circuit

of four linear elements (an inductor, a resistor, and two capacitors) and a nonlinear diode, which altogether can be modeled [57] with the following set of ODEs:

$$\begin{aligned}\dot{x} &= c_1(y - x - g(x)) \\ \dot{y} &= c_2(x - y + z) \\ \dot{z} &= -c_3y,\end{aligned}\tag{1.19}$$

where  $x$  and  $y$  represent voltages across the capacitors,  $z$  denotes the current on the inductor, and the linear sections of the  $g(x) = m_1x + (m_0 - m_1)(|x + 1| - |x - 1|)/2$  function, represent different voltage-current regimes of the diode. The  $g(x)$  function is the only non-linear term in the system. Chua's circuit, studied as a function of the  $c_3$  parameter, exhibits a double Hopf-bifurcation, leading to two coexisting limit-cycles, which begin a period-doubling cascade route to chaos. First, two separate chaotic attractors are created, which eventually merge in crisis.

## Chapter 2

# A new prototype system with multistability

Sándor, B., & Gros, C. (2015). *A versatile class of prototype dynamical systems for complex bifurcation cascades of limit cycles*. *Scientific Reports*, 5, 12316.

In **Chapter 1** we introduced the basic methods and concepts of dynamical systems and chaos theory, arguing that they need to be extended further for the study of higher dimensional complex adaptive systems. In this chapter we present a new approach for constructing multistable systems using a mechanistic design procedure.

First, we give a short introduction to prototype dynamical systems, pointing out that many of them fall under the same class of equations, and illustrating also how the control of energy balance can be used for generating bifurcations. Then, a new class of dynamical systems [7] is proposed, which may be used as prototypes for the modeling and investigation of complex bifurcation scenario of limit cycles and chaotic attractors, appearing in other higher dimensional and possibly more complex systems. Based on the idea of controlling the phase space regions of energy uptake and dissipation, we introduce a novel friction function, depending explicitly on the mechanical potential, which is in turn characterized by a finite number of local minima. Following the recipe of defining generalized potential functions, which allow for setting the positions and heights of the respective minima, one can design systems with a predefined number of different attractors in the phase space. Using double-well potential and polynomial friction functions, we demonstrate a few different scenarios of multistability by constructing their respective bifurcation diagrams. At the end of this chapter, an analytic proof of the limit cycle generation is given.

## 2.1 Introduction to prototype dynamical systems

In the field of dynamical systems theory prototype systems play the role of models, being generic but simple enough for (at least partial) analytic or straightforward numerical investigations. The dynamical behavior of prototype systems is primarily dominated by the main phenomenon of interest, and it can often be understood in an intuitive manner in terms of energy balance between dissipation and uptake, or symmetry properties of the systems [7].

Classical examples of prototype systems have contributed significantly to our understanding of many complex dynamical behavior. The van der Pol oscillator [1] has been used as a prototype for the study of the generation and control of relaxation-oscillations, whereas the logistic map and the Lorenz model [22] are probably the most well known discrete, respectively continuous time systems generating chaotic behavior. The periodically driven, i. e. non-autonomous versions of the van der Pol, and of the double-well Duffing oscillators have been investigated thoroughly, not only in numerical [58–60], but also in experimental studies (see Sec. 1.1.7) [22].

The normal forms of bifurcation analysis [1, 54, 61], are prototypes determining the local bifurcations in a system. The Takens-Bogdanov system [62, 63], to give an example, provides the normal form for both local, (saddle-node and Hopf), and global (homoclinic) bifurcations. Furthermore, the homoclinic bifurcation can also be interpreted in terms of the critical amount of energy uptake needed to overcome the potential barrier set by the saddle point [1, 7].

Several prototype systems showing interesting dynamical phenomena have been found by coincidence, or on a trial and error basis. The Lorenz equations, for example, have originally been derived for modeling thermal convection in the atmosphere, but with the discovery of the underlying unpredictable dynamical behavior, it has become a paradigm of chaotic dynamics [23]. On the other hand, the Rössler equations have already been designed with the intention of constructing a similarly behaving system to the Lorenz attractor, which is however easier to analyze qualitatively [64]. Continuing this line of work, in the past two decades a great deal of three and four dimensional chaotic attractors have been proposed leading to a classification between double-scroll [57, 65, 66] and multi-scroll [67] attractors. The deployment of this versatile zoo of chaotic systems lead to the elaboration of systematic construction methods in the dynamical systems literature. These methods involve however either the use of engineering feedback control approaches [66, 68], or of somewhat abstract concepts, such as switching between implicitly defined manifolds [67] or switching between slow and fast sub-systems [69].

Furthermore, most of the systems discussed so far do not enable the coexistence of multiple attractors. However, as it has been pointed out by several studies, mul-

tistability is essential for modeling many complex dynamical phenomena (see [5] for a recent review). The construction of dynamical systems with an arbitrary number of (chaotic or limit cycle) attractors has been a long standing problem. In the endeavor of identifying such cases several different mechanisms, including the coupling of sub-systems [70] or the use of delayed feedback [71], have been revealed, which may be involved in the generation of simultaneous attractors. On the other hand, it is also known that one can observe small parameter regions for low dimensional systems with multiple simple or strange attractors, a result of the inherent symmetries characterizing the equations of motion [72, 73].

In contrast to these approaches, we propose here a mechanistic design procedure, based on the generation of attractors via the interaction of generalized friction and potential functions, a method also accessible for modeling interdisciplinary problems [7]. The resulting versatile prototype systems are adaptive, allowing for an explicit control, with a single parameter, of the regions with energy uptake and dissipation. The availability of this control parameter enables the study and generation of complex bifurcation cascades of limit cycles advancing to a transition to chaos. Creating a predefined number of potential minima, one can, in principle, generate arbitrary many attractors, an appealing example for extreme multistability [70].

## 2.2 Recipes for multistability

In Sec. 1.1.2 we characterized adaptive systems by the coexistence of contracting and expanding phase space regions. In case of mechanical systems the dilatation of the phase space would correspond to energy uptake via anti-dissipative forces (compare Eqs. (1.8) and (1.9)). Hence, considering Liénard type equations,

$$\ddot{x} - f(x)\dot{x} + V'(x) = 0, \quad (2.1)$$

with generalized position dependent friction forces  $f(x)$ , one can realize different regions of energy uptake and dissipation along the potential landscape  $V(x)$ .

A well-known example of Liénard type adaptive systems is the Bogdanov-Takens system [1],

$$\begin{aligned} \ddot{x} - (x - \mu)\dot{x} + V'(x) &= 0, & \dot{x} &= y \\ \dot{y} &= (x - \mu)y - V'(x), \end{aligned} \quad (2.2)$$

describing the dynamics of a mass point in a potential well  $V(x) = x^3/3 - x^2/2$  in the presence of the linear friction function  $f(x) = x - \mu$ . As illustrated in the top left sketch of Fig. 2.1 the parameter  $\mu$  divides the potential in two regions, since the change of the total energy (1.9), and analogously the phase space contraction rate (1.8),

$$\dot{E} = (x - \mu)y^2, \quad \sigma(x) = x - \mu, \quad (2.3)$$

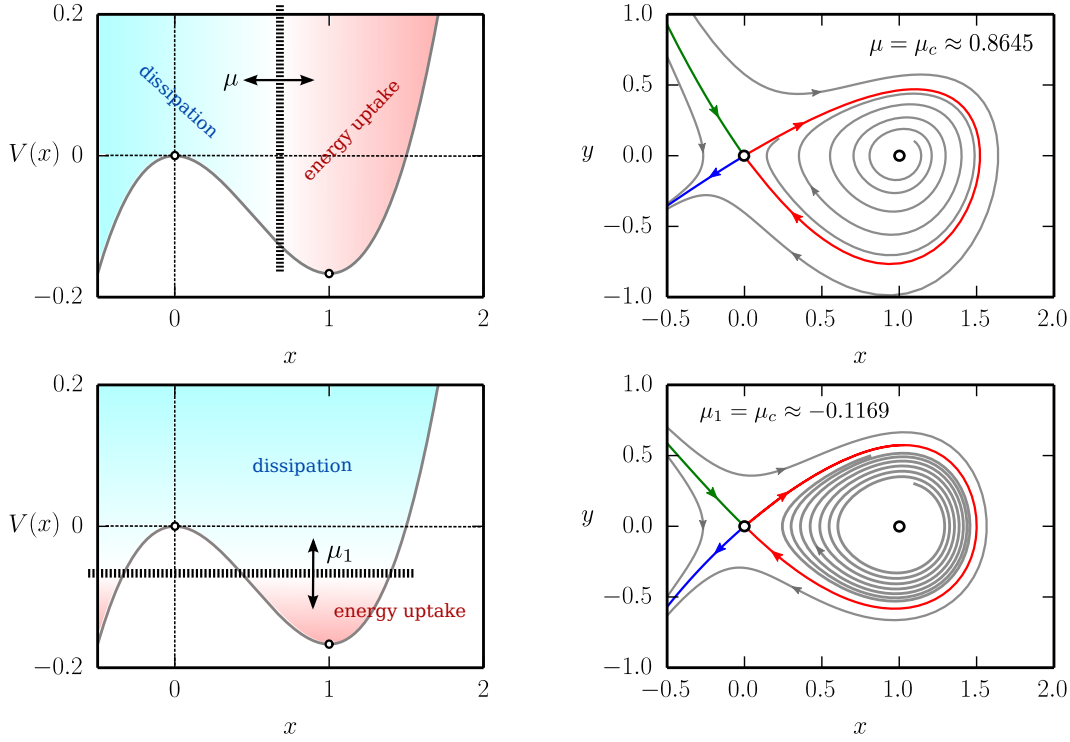


**Figure 2.1:** *The Bogdanov-Takens system (2.2) with the friction function  $f(x) = x - \mu$  (top row), and its generalized version (2.4) using  $f_1(x) = \mu_1 - V(x)$  (bottom row), compare Eq. (2.6). **Left column:** The color-coded regions of energy uptake and dissipation respectively of the potential function  $V(x) = x^3/3 - x^2/2$ , compare Eq. (2.3). **Right column:** The flow in the phase planes of the respective systems at the homoclinic bifurcation point  $\mu_c$ , showing typical trajectories by gray curves. The saddle points at  $(x_0^*, y_0^*) = (0, 0)$  and the repelling foci at  $(x_1^*, y_1^*) = (1, 0)$  are indicated by open circles. The red trajectory corresponds to the homoclinic loop, while on the opposite side of the saddle point the stable and unstable manifolds are shown by green and blue trajectories respectively.*

is negative, corresponding to dissipation (contraction), for  $x < \mu$ , while an energy uptake (dilation) is realized for  $x > \mu$ . Hence, the potential minimum at  $x_1^* = 1$  is a stable fixpoint of the system,  $(x_1^*, y_1^*) = (1, 0)$ , when  $\mu > x_1^*$ , being surrounded by a dissipative region. Decreasing the control parameter  $\mu$  the fixpoint is destabilized for  $\mu < x_1^*$ , becoming repelling due to the uptake of energy, leading to limit cycle oscillations. The amplitude of oscillations is increasing with the growth of the anti-dissipative region, reaching a critical value, with the mass point escaping via the local maximum  $x_0^* = 0$ , for  $\mu_c$ . The phase plane plot corresponding to  $\mu = \mu_c$  is shown in the top right panel of Fig. 2.1, illustrating when the limit cycle touches the saddle point  $(x_0^*, y_0^*) = (0, 0)$  in a homoclinic loop.

As the example of the Takens-Bogdanov system (2.2) has also demonstrated, a suitably chosen position-dependent friction function may allow for the generation

of limit cycle attractors, by controlling the relative extension of the dissipative and anti-dissipative regions of the potential well. In the following section we propose a generalization of the Liénard type equations (2.1) with potential functions having an arbitrary number of local minima.

### 2.2.1 A new class of prototype systems

The key mechanism in generating a sustained oscillatory behavior in the Takens-Bogdanov system is the destabilization of the local minima by manipulating the region of energy uptake. Here we propose a  $2d$ -dimensional generalization of the Liénard-type systems,

$$\ddot{\mathbf{x}} - f(V(\mathbf{x}))\dot{\mathbf{x}} + \nabla V(\mathbf{x}) = 0, \quad \begin{aligned} \dot{\mathbf{x}} &= \mathbf{y} \\ \dot{\mathbf{y}} &= f(V(\mathbf{x}))\mathbf{y} - \nabla V(\mathbf{x}), \end{aligned} \quad (2.4)$$

with  $d$  spatial coordinates  $\mathbf{x} = (x_1, x_2, \dots, x_d)$  and velocities  $\mathbf{y} = (y_1, y_2, \dots, y_d)$ , respectively. The friction function  $f(V(\mathbf{x}))$ , depending functionally only the mechanical potential  $V(\mathbf{x})$ , allows for a fine tuned control of the energy dissipation around the local minima:

$$\dot{E} = f(V(\mathbf{x}))|\mathbf{y}|^2, \quad E = \frac{|\mathbf{y}|^2}{2} + V(\mathbf{x}). \quad (2.5)$$

This class of prototype systems (2.4) is entirely general in the sense that any friction function of the type  $f(V)$  may be considered, in a combination with potentials  $V(\mathbf{x})$ , characterized by a certain number of local minima.

### 2.2.2 Polynomial friction functions

We demonstrate the wide range of realizable dynamical behaviors and bifurcation scenarios by considering the simplest class of friction functions  $f(V)$  entering Eq. (2.4), namely polynomials of increasing order:

$$\begin{aligned} f_1(V) &= -\alpha(V - \mu_1), \\ f_2(V) &= -\alpha(V - \mu_1)(V - \mu_2), \\ f_3(V) &= -\alpha(V - \mu_1)(V - \mu_2)(V - \mu_3), \end{aligned} \quad (2.6)$$

where the parameter  $\alpha$  is setting the effective strength of the generalized friction force. The zeros of the polynomials are set by the  $\mu_1 < \mu_2 < \mu_3$  control parameters, defining the points where dissipation changes to anti-dissipation or vice versa (compare Eq. (2.5)).

As a first example, we consider the  $d = 1$  version of the prototype system (2.4), together with the cubic potential  $V(x) = x^3/3 - x^2/2$ , and the first order friction term  $f_1(V)$  (as defined by Eq. (2.6)). The different regions of dissipation and energy uptake are defined now by the horizontal separation line, set by  $\mu_1$ , as illustrated in

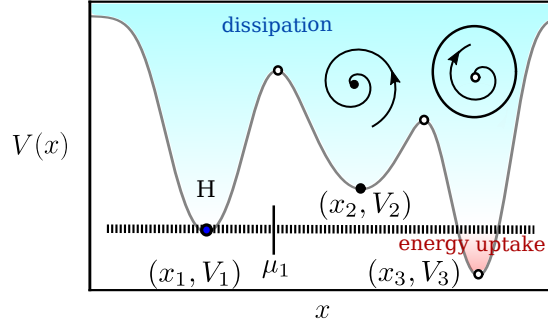


**Figure 2.2:** Sketch of a one-dimensional potential function  $V(x)$ , illustrating the different possible fixpoint types corresponding to the three minima of different depth ( $V_3 < V_1 < V_2$ ): Hopf-point at  $(x_1, V_1)$  (denoted by H), stable focus at  $(x_2, V_2)$ , and unstable focus at  $(x_3, V_3)$  surrounded by a region with energy uptake, when using the linear friction function  $f_1(V)$  characterized by the parameter  $\mu_1$  in Eq. 2.6. The corresponding flow in the  $(x, y)$  plane is depicted by the sketches above the minima.

the bottom left plot of Fig. 2.1. The resulting flow in the phase space is equivalent to the one of the Takens-Bogdanov system's (2.2), also leading to homoclinic bifurcation for the critical  $\mu_c$  (see bottom row of Fig. 2.1). Another example of prototype systems of type (2.4) is the well-known Van der Pol oscillator,

$$\ddot{x} - \epsilon(1 - x^2)\dot{x} + x = 0, \quad (2.7)$$

with a first order polynomial friction function  $f_1(V) = -\epsilon(2V - 1)$  and quadratic potential  $V(x) = x^2/2$ , where  $\epsilon$  is regulating the influence of the friction force.

Considering now the case of general  $d = 1$  dimensional potentials, it is easy to show that the local critical points of the potential function, i.e. where  $V'(x^*) = 0$ , are always fixpoints of the system (2.4) corresponding to the velocity  $y^* = 0$ . Calculating the corresponding eigenvalues  $\lambda_{1,2}$  of the Jacobian  $\mathbf{J}$ ,

$$\lambda_{1,2} = \frac{1}{2} \left( a \pm \sqrt{a^2 - 4d} \right) \quad \mathbf{J}(x^*, y^*) = \begin{pmatrix} 0 & 1 \\ -d & a \end{pmatrix}, \quad (2.8)$$

with  $a = f(V(x^*))$  and  $d = V''(x^*)$ , we see that maxima of the potential function, viz where  $V''(x^*) < 0$ , are always saddle points (cf. Fig. 2.1). Local minima, characterized by  $V''(x^*) > 0$ , turn into repelling foci, when dissipation changes to anti-dissipation,  $f(V(x^*)) = 0$ , generating a limit cycle as a result of a Hopf bifurcation, having a simple pair of purely imaginary eigenvalues  $\lambda_{1,2} = \pm i\sqrt{V''(x^*)}$  (see Eq. (2.8)). This is illustrated in Fig. 2.2 with a potential function  $V(x)$  characterized by three minima of different levels,  $V_3 < V_1 < V_2$ , and a linear friction function  $f_1(V)$ . When lifting the barrier (indicated by  $\mu_1$ ) separating the different regions, the fixpoint corresponding to the deepest minimum  $(x_3, V_3)$  is destabilized first, while the fixpoint at  $(x_2, V_2)$  is still stable. Since  $\mu_1 \approx V_1$ , the first minimum  $(x_1, V_1)$  is about to undergo a Hopf-bifurcation.

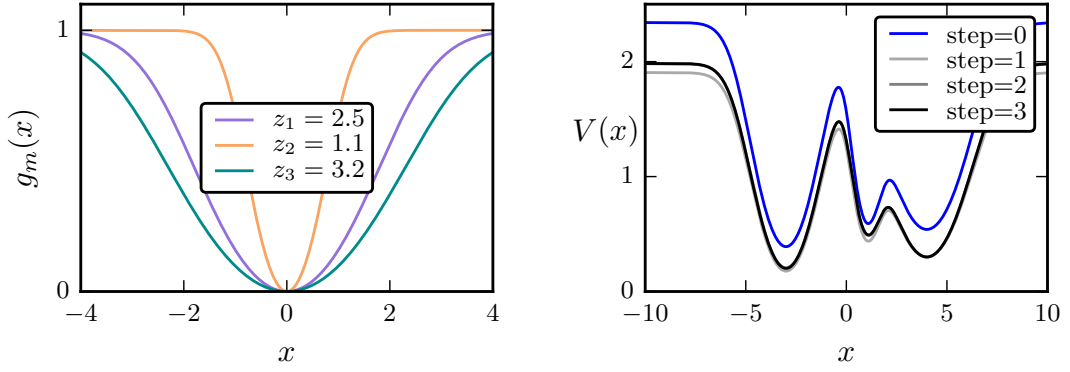


**Figure 2.3:** The construction of generalized potential functions (2.9). **Left:** Setting the width of the potential well by using different  $z_m$  parameters (see the legend) in the  $g_m(x) = \tanh(x^2/z_m^2)$  functions. **Right:** The self-consistent determination of the  $p_m$  parameters, defined by Eq. 2.10 for the potential  $V(x)$  with  $M = 3$  minima at  $x_{1,2,3} = -3/1/4$  and heights of  $V_{1,2,3} = 0.2/0.5/0.3$  respectively for the left/center/right one. Different colors correspond to consecutive iteration steps using Eq. (2.10), started from  $p_{1,2,3}^{(0)} = 1/1/1$  non-optimized values. Convergence is achieved after three steps,  $p_{1,2,3}^{(3)} = 1, 72/0.98/1.68$ , the relative change of  $p_m$  between steps 2 and 3 becoming smaller than  $10^{-2}$ .

### 2.2.3 Generalized potential functions

The type of the generated attractors can hence also be controlled by setting the depth  $V_m$  of the corresponding local minimum. An arbitrary number of local minima could also be constructed, in principle, by using higher order polynomials  $V(\mathbf{x})$ , these do not allow, however, for a direct regulation of the width and depth of minima.

Here, we propose an alternative set of generalized mechanical potentials, characterized by an  $M$  number of local minima with predefined positions and heights  $(\mathbf{x}_m, V_m)$ :

$$V(\mathbf{x}) = \prod_{m=1}^M \left( g_m(\mathbf{x} - \mathbf{x}_m) + \frac{V_m}{p_m} \right), \quad g_m(\mathbf{z}) = \tanh(|\mathbf{z}|^2/z_m^2), \quad (2.9)$$

where the  $z_m$  determine the half-widths of the respective wells (see the left plot of Fig. 2.3). The parameters  $p_m$  satisfy the

$$p_m = \prod_{k \neq m} \left( g_k(\mathbf{x}_m - \mathbf{x}_k) + \frac{V_k}{p_k} \right) \quad (2.10)$$

self-consistent condition with  $g_k(0) = 0$ , which can be verified via

$$V(\mathbf{x}_m) = \frac{V_m}{p_m} \prod_{k \neq m} \left( g_k(\mathbf{x}_m - \mathbf{x}_k) + \frac{V_k}{p_k} \right) = V_m. \quad (2.11)$$

Note that the local minima of the potential  $V(\mathbf{x})$  are the result of the zero points of the  $g_m(0) = 0$  functions (cf. Fig. 2.3), hence for deep and distinct wells, with  $z_j + z_k \ll |\mathbf{x}_j - \mathbf{x}_k|$ , the positions and heights are close to  $\mathbf{x}_m$  and  $V_m$  respectively. In Fig. 2.3 we show an example of the self-consistent determination of the  $p_m$  parameters for a potential function with three minima, i. e. starting with an initial guess for  $p_m^{(0)}$ , and iterating  $p_m^{(i+1)} \rightarrow p_m^{(i)}$  using the map defined by Eq. (2.10). The experience shows that a convergence corresponding a relative change of  $(p_m^{(i+1)} - p_m^{(i)})/p_m^{(i)} < 10^{-2}$  can generally be achieved in 3 – 4 steps.

## 2.3 Multistability and chaos in double-well potentials

To demonstrate how the multistability of attractors can be realized in the prototype system (2.4) we consider generalized potentials (2.9) in  $d = 1$  and  $d = 2$  dimensions.

### 2.3.1 Limit-cycle generation

First, we start by considering a simple  $n = 2$  dimensional (with  $d = 1$ ) system, as defined by (2.4), together with a double-well potential, using first/second/third order polynomial friction functions (2.6),  $f_1(V)/f_2(V)/f_3(V)$ , respectively (see Fig. 2.4). The local maximum of the potential at  $x_0 = 0$  is a saddle type fixpoint in all the three cases. The stability of the coexisting fixpoint attractors, corresponding to the two minima at  $x_{1,2} = \pm 1$  and  $V_{1,2} = 0$  can be controlled, on the other hand, by varying the bifurcation parameter  $\mu_1$  of the friction functions (2.6). The corresponding bifurcation diagrams, created by using numerical continuation methods [74], are presented in the right column of Fig. 2.4, showing the existing stable and unstable fixpoints or limit-cycles, together with the respective bifurcation points.

For the linear and quadratic friction functions,  $f_1(V)$  and  $f_3(V)$  respectively, we observe the generation of two coexisting limit cycle attractors via supercritical Hopf bifurcations. In case of  $f_1(V)$ , the limit cycles unite into a large amplitude cycle by a homoclinic bifurcation, while for a  $f_3(V)$  the more complex bifurcation cascade of limit cycles allows for three simultaneous attractors as well. On the other hand, with the quadratic friction term  $f_2(V)$ , two unstable cycles are created which are, later on, annihilated in a saddle-node bifurcation, when colliding with a large amplitude limit cycle.

Fig. 2.5 shows the phase plane plots with the different possible stable and unstable limit cycles, corresponding to the respective  $\mu_1$  parameters, as indicated by small arrows in top of the panels of Fig. 2.4. Coexisting stable limit cycles can be constructed in multiple ways: either as being localized in the separate minima of the potential, or being embedded in larger overarching attractors.

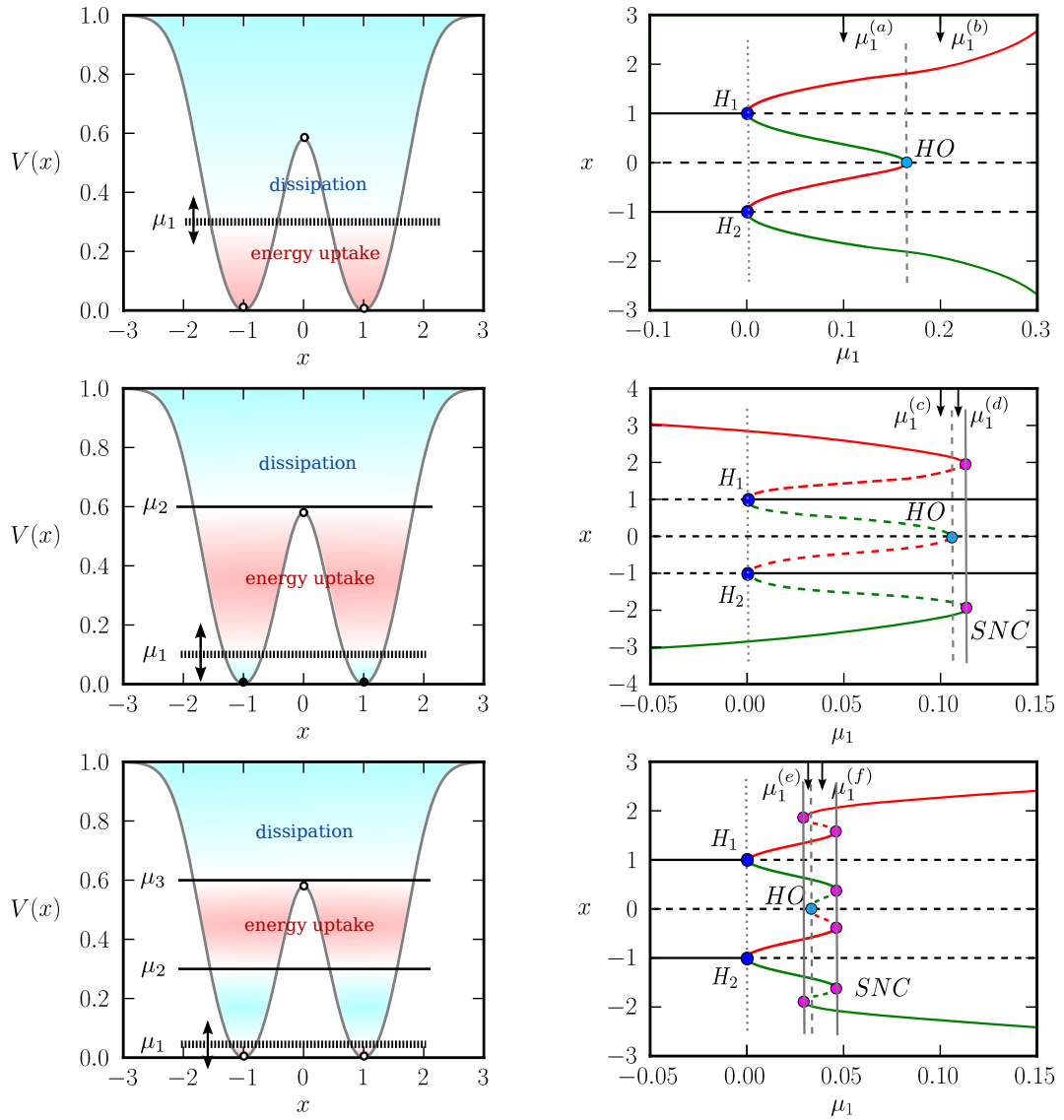


**Figure 2.4:** The prototype system (2.4) using the double well potential function (2.9) with  $x_{1,2} = \pm 1$ ,  $V_{1,2} = 0$ ,  $z_{1,2} = 1$  and  $p_{1,2} = 1$ , and the friction functions (2.6)  $f_1$  with  $\alpha = 1$  (row),  $f_2$  with  $\mu_2 = 0.6$  and  $\alpha = 5$  (middle row), and  $f_3$  with  $\mu_2 = 0.3$ ,  $\mu_3 = 0.6$  and  $\alpha = 5$  (bottom row). **Left column:** The double well potential function with the color-coded regions of energy uptake  $\dot{E} > 0$  and dissipation  $\dot{E} < 0$  corresponding to the three polynomial friction functions  $f_{1,2,3}$ . **Right column:** Bifurcation diagrams as a function of  $\mu_1$ , keeping the other  $\mu_i$  (when present) constant. Stable/unstable fixpoints (limit-cycles) are denoted by the dashed/continuous black (color) curves. For limit cycles the maximal/minimal amplitude of  $x$  is indicated by the red/green colors. The bifurcation points are denoted by filled color circles:  $H$  – Hopf-bifurcations,  $HO$  – homoclinic bifurcations,  $SNC$  – saddle node bifurcations of limit cycles. The dotted, dashed and continuous vertical gray lines are just guides for the eyes.

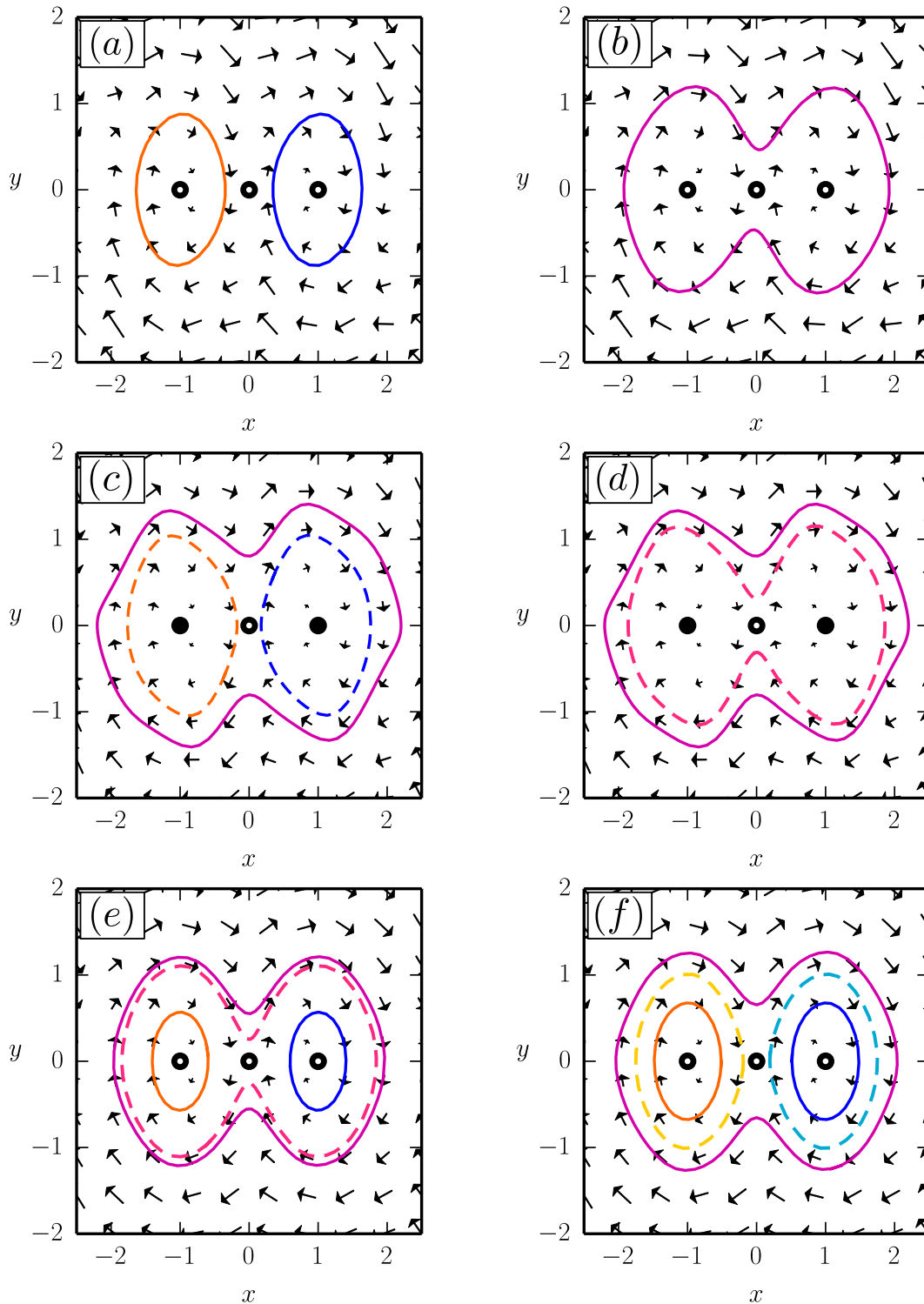


**Figure 2.5:** Phase plane plots of the systems presented in Fig. 2.4, using respectively the linear/quadratic/cubic friction functions (2.6)  $f_1(V)/f_2(V)/f_3(V)$  (top/middle/bottom row), corresponding to the  $\mu_1^{(a/b)} = 0.1/0.2$ ,  $\mu_1^{(c/d)} = 0.1/0.11$  and  $\mu_1^{(e/f)} = 0.032/0.04$  parameters, also indicated by the small arrows in the corresponding bifurcation diagrams of Fig. 2.4. Stable/unstable fixpoints (limit cycles) are shown again by filled/open circles (continuous/dashed curves). The direction and length of the arrows in the phase plane plots indicates the flow in the respective points.

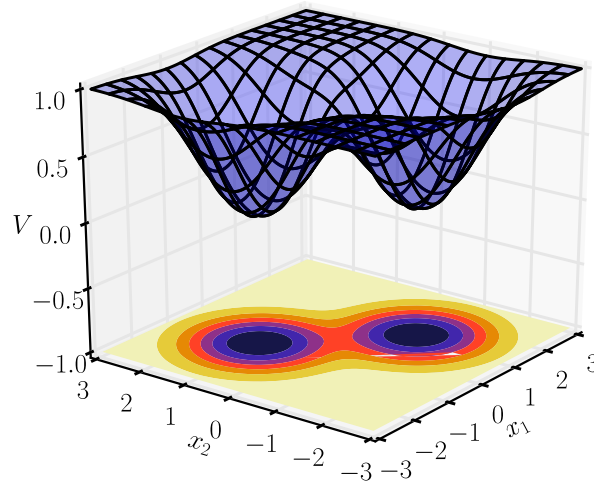


**Figure 2.6:** 3-dimensional illustration of the double-well potential  $V(x_1, x_2)$  defined by Eq. 2.12, with a color-coded projection to the  $(x_1, x_2)$  plane, indicating the depth of the minima (also used in Fig. 2.7). The minima of the potential  $V(\mathbf{x}_{1,2}) = 0$  at positions  $\mathbf{x}_1 = (+1, -1)$  and  $\mathbf{x}_2 = (-1, +1)$  are symmetrical with respect to both diagonals in the  $(x_1, x_2)$  plane.

We speculate, furthermore, that increasing the order of the polynomials used in the friction function (2.6), an unlimited set of nested limit cycles may be generated. One can on the other hand also create potentials with infinitely many minima, placed on a regular grid, or spread randomly along the  $x$  axis, hence, the prototype system provides an appealingly simple technique for realizing extreme multistability [70].

### 2.3.2 Generating chaos in the 4-dimensional system

More complex dynamics than limit cycle oscillations is not possible in 2-dimensional flows [22]. Hence, to generate chaos, we have to extend the dimensionality of the phase space. A natural generalization of the previous example, can easily be realized using Eq. 2.9, by considering now a  $n = 4$  dimensional system, with a symmetric potential function (with  $d = 2$ ),

$$V(\mathbf{x}) = g(\mathbf{x} - \mathbf{x}_1)g(\mathbf{x} - \mathbf{x}_2), \quad g(\mathbf{z}) = \tanh(4\mathbf{z}^2/9), \quad (2.12)$$

with two minima at  $\mathbf{x}_1 = (+1, -1)$  and  $\mathbf{x}_2 = (-1, +1)$ , together with  $V_{1,2} = 0$ , and  $z_{1,2} = 1.5$ , shown also in Fig. 2.6. Note that the potential (2.12) is symmetric with respect to both diagonals in the  $(x_1, x_2)$  plane, hence due the structure of Eq. (2.4) the solutions of the system have to be symmetry related. Namely, if  $(x_1, x_2, y_1, y_2)$  is a solution, then

$$\begin{pmatrix} x'_1 \\ x'_2 \\ y'_1 \\ y'_2 \end{pmatrix} = \mathbf{S}_{1,2} \begin{pmatrix} x_1 \\ x_2 \\ y_1 \\ y_2 \end{pmatrix}, \quad \begin{pmatrix} x''_1 \\ x''_2 \\ y''_1 \\ y''_2 \end{pmatrix} = \mathbf{S}_{3,4} \begin{pmatrix} x_1 \\ x_2 \\ y_1 \\ y_2 \end{pmatrix} \quad (2.13)$$

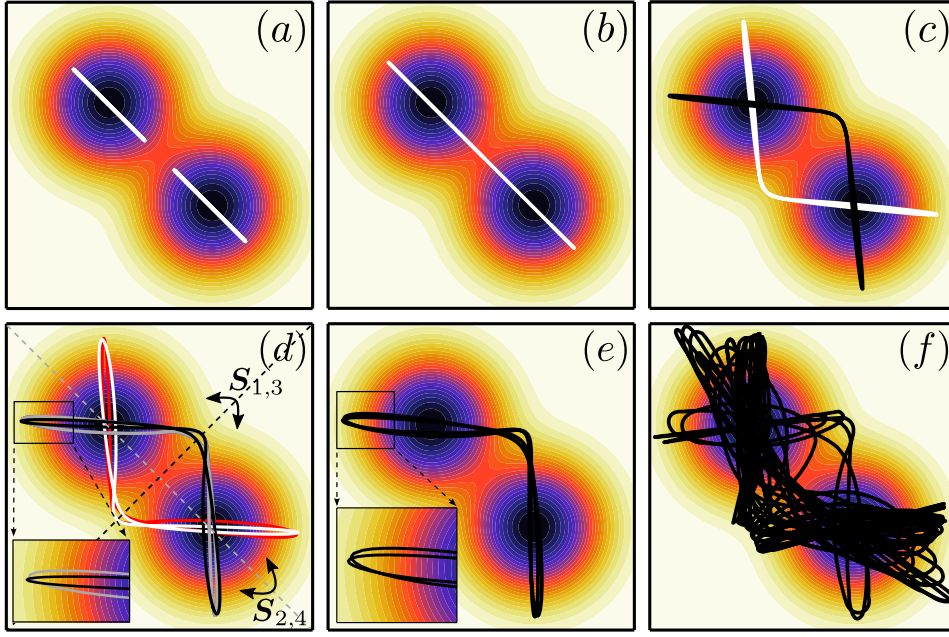


**Figure 2.7:** Trajectories of stable limit cycles and chaotic attractors of the prototype system (2.4) with a two-dimensional symmetric double-well potential  $V(\mathbf{x})$ , defined by Eq. (2.12) (color coded as in Fig. 2.6), and with linear friction term  $f_1(V)$  setting  $\alpha = 1.5$  in Eq. (2.6). The parameter  $\mu_1$  is increased through the values 0.1, 0.15, 0.25, 0.265, 0.2698, 0.3 for the panels from (a) to (f). The two limit cycles in panel (a), aligned exactly along the diagonal, merge in a large amplitude cycle in (b), analogously to the case of the 2-dimensional prototype system (compare Fig. 2.5). In plot (c) we see however the appearance of two symmetry related orbits, splitting further in (d) into four limit cycles, which can mapped into each other by the symmetry operations  $\mathcal{S}_{1,2}$  and  $\mathcal{S}_{3,4}$  (2.14). In panel (e) only one of the four period-doubled limit cycles is shown, as indicated in the inset. In (f) a short segment of a chaotic orbit is given.

are also solutions, where  $\mathcal{S}_{1,2}$  and  $\mathcal{S}_{3,4}$  are denoting reflections with respect to the diagonals in the  $(x_1, x_2)$ , respectively both in the  $(x_1, x_2)$  and in the  $(y_1, y_2)$  planes:

$$\mathcal{S}_{1,2} = \begin{pmatrix} 0 & \pm 1 & 0 & 0 \\ \pm 1 & 0 & 0 & 0 \\ 0 & 0 & 1 & 0 \\ 0 & 0 & 0 & 1 \end{pmatrix}, \quad \mathcal{S}_{3,4} = \begin{pmatrix} 0 & \pm 1 & 0 & 0 \\ \pm 1 & 0 & 0 & 0 \\ 0 & 0 & 0 & \pm 1 \\ 0 & 0 & \pm 1 & 0 \end{pmatrix} \quad (2.14)$$

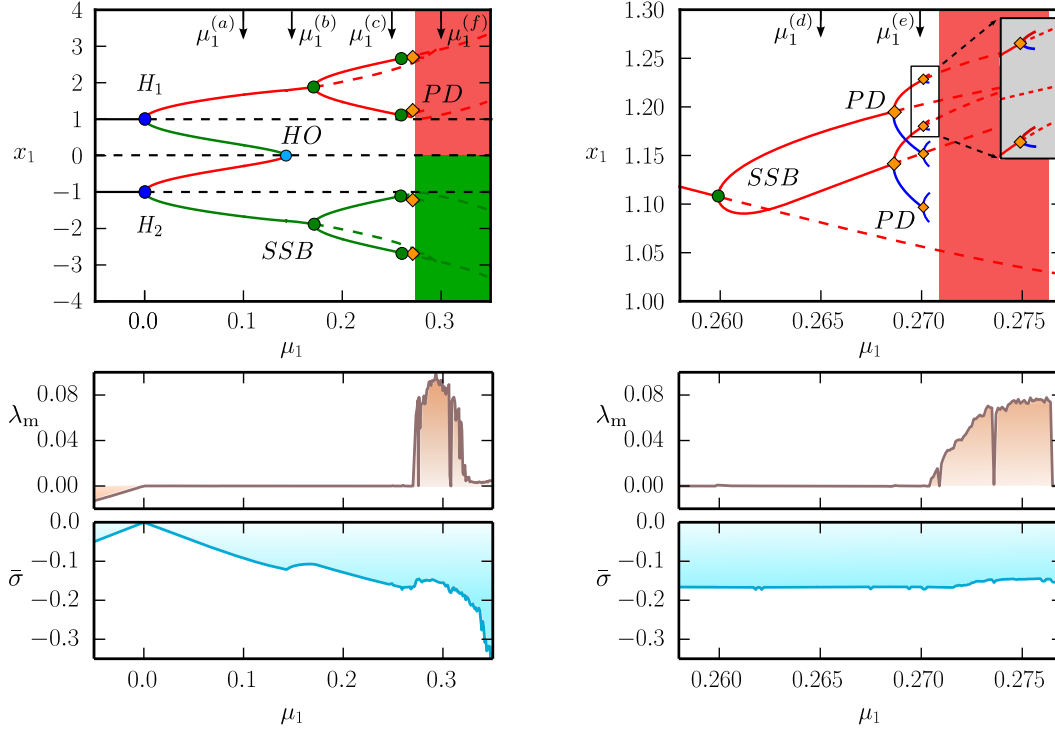
Here, we present an in-depth study of the generation of attractors using a simple linear friction function  $f_1(V)$  with  $\alpha = 0.5$ , as defined by Eq. (2.6). The possible limit cycle and chaotic solutions, projected to the  $(x_1, x_2)$  plane in Fig. 2.7, are shown for increasing values (given in the caption) of the  $\mu_1$  control parameter. To understand the generation of these attractors a detailed bifurcation diagram, see

Fig. 2.8, has been constructed using numerical continuation methods [74].

The transitions between the limit-cycles, respectively chaotic attractor, illustrated in panels (a)–(f) of Fig. 2.7, correspond to a series of bifurcations, as indicated in Fig. 2.8:

- The fixpoints at the minima of the potential function are stable for  $\mu_1 < 0$ , being destabilized via the supercritical Hopf bifurcations  $H_1$  and  $H_2$  for  $\mu_1^{(H)} = 0$ , generating two small amplitude limit cycles along the diagonal (see Fig. 2.7(a)). Note that, due to the degeneracy of the Hopf-point (explained in the following section), there exist two other limit cycles, perpendicular to former ones, which are however unstable for most of the interval, hence not shown here. See Fig. B.2 in the Appendix for details.
- The limit cycles merge in a homoclinic saddle bifurcation  $HO$  at  $\mu_1^{(HO)} \approx 0.143$ . The resulting large amplitude orbit stays, however, for a range of parameters on the diagonal  $x_2 = -x_1$  (see Fig. 2.7(b)).
- At  $\mu_1^{(SSB)} \approx 0.171$  the symmetry of the limit cycle – reflection with respect to the  $x_2 = -x_1$  diagonal – is spontaneously broken, which is followed by another symmetry breaking bifurcation at  $\mu_1^{(SSB)} \approx 0.260$ , destroying the remaining symmetries corresponding to the reflections about  $x_2 = x_1$  (see Figs. 2.7(c, d)). The resulting four cycles are hence related via the  $S_{1,2}$  and  $S_{3,4}$  operations.
- Increasing the control parameter  $\mu_1$ , we observe a series of period doubling bifurcations. Due to the inherent symmetries of the system, the period-doubling of the four attractors occurs simultaneously, the first one at  $\mu_1^{(PD)} \approx 0.268$  (in Fig. 2.7(e) showing only one of the obtained double period limit cycles), followed by the second one at  $\mu_1^{(PD)} \approx 0.270$  (see the inset of Fig. 2.8).
- The period-doubling bifurcations lead to a transition to chaos for  $\mu_1 > \mu_1^{(\text{chaos})} \approx 0.2705$  (see Fig. 2.7(f) for a trajectory segment on the attractor). Note that the saddle point of the potential function corresponds to the  $V(0, 0) = 0.505$  height, hence the appearance of chaos is not directly related to that.

To identify the chaotic region more precisely, we have evaluated the maximal Lyapunov exponent  $\lambda_m$ , as defined by Eq. (1.15), for the corresponding parameter interval in the bottom row of Fig. 2.8. Asymptotic convergence to fixpoints is indicated by  $\lambda_m < 0$ , while the dynamics along limit cycles is characterized by  $\lambda_m = 0$ . The chaotic region, with the sensitivity to initial conditions reflected by  $\lambda_m > 0$ , is interrupted by many periodic windows, where the exponent drops to zero again. For the numerical computation of  $\lambda_m$  we used the method described in



**Figure 2.8:** The 4-dimensional prototype system (2.4) with the symmetric double-well potential (2.12) and linear friction function  $f_1(V)$  fixing  $\alpha = 1.5$  in Eq. (2.6). **Top row:** Bifurcation diagram, with the small arrows indicating the respective  $\mu_1$  parameters used to obtain the phase plane plots presented in Fig. 2.7. Notations are as for Fig. 2.4: black (color) continuous/dashed curves – stable/unstable fix-points (limit cycles),  $H$  and  $HO$  – Hopf and homoclinic bifurcations,  $SSB$  and  $PD$  – spontaneous symmetry breaking and period-doubling bifurcations of limit cycles. The red/green curves indicate the maximal/minimal  $x_1$  values of the respective oscillations. The chaotic dynamics for  $\mu > 0.2705$  is indicated by the red and green shaded regions. The second branch of limit cycles emerging from the destabilized minima are not shown here (see Fig. B.2 in the Appendix). The right diagram presents a blow-up of the period-doubling transition to chaos, showing only the first two  $PD$  points (see the gray inset with a zoom-in to the second period-doubling). After period doubling the second largest amplitude is shown by the blue curves. **Bottom row:** The maximal Lyapunov exponent  $\lambda_m$  (see Fig. B.3 for the computation) and the average contraction rate  $\bar{\sigma}$  (defined by Eq. (2.15)), for the corresponding  $\mu_1$  parameter intervals. The parameter stepsize used of the left plot is  $\Delta\mu_1 = 0.001$ . Further periodic windows, emerging in the chaotic region, with  $\lambda_m = 0$ , are revealed when increasing the resolution by a factor of ten, as in the right diagram, corresponding to the zoom-in. The average contraction rate is negative,  $\bar{\sigma} < 0$ , for the whole interval investigated here.

Sec. 1.1.3, with the actual implementation presented in Sec. B.3 in the Appendix.

The here studied prototype system (2.4) is adaptive, hence locally contracting and expanding regions are alternating along the trajectories. Therefore, we introduce the average contraction rate  $\bar{\sigma}$ , to assess the overall behavior of phase space volumes in the asymptotic limit. That is the average of local contraction rates  $\sigma(\mathbf{x})$  (see Eq. 1.3) along a set of trajectories  $\Gamma_i$  over the attractor:

$$\bar{\sigma} = \left\langle \frac{1}{L_i} \int_{\Gamma_i} \nabla \cdot \mathbf{f} ds \right\rangle, \quad \sigma(\mathbf{x}) = \nabla \cdot \mathbf{f}, \quad (2.15)$$

with  $L_i = \int_{\Gamma_i} ds$  denoting the length of the orbit, and with  $\mathbf{f}$  the respective right-hand side of the ODE (2.4). As we can see in the bottom panels of Fig. 2.8, the overall phase space is contracting,  $\bar{\sigma} < 0$  for the whole parameter interval. For  $\mu_1 < 0$  the stable fixpoints at the minima of the potential are enclosed by a finite dissipative region, hence  $\bar{\sigma} < 0$ . However, in case of the periodic and chaotic dynamics for  $\mu_1 > 0$ , with the trajectory visiting locally expanding phase space regions as well, the  $\bar{\sigma} < 0$  indicates a non-trivial phase space contraction on the attractors [1, 61].

The maximal Lyapunov exponent  $\lambda_m$  and the average contraction rate  $\bar{\sigma}$  are both quantities characterizing the dynamics of an attractor. In case of multistability, detached attractors allow generally for a distinct set of  $\lambda_m$  and  $\bar{\sigma}$  values. We note, however, that due to the symmetries  $\mathbf{S}_{1,2}$  and  $\mathbf{S}_{3,4}$  of the system, one can assign here the same maximal Lyapunov exponent and average contraction rate to each of the coexisting limit cycle or fixpoint attractors for a given  $\mu_1$ .

Inspecting the plot of the Lyapunov exponent in Fig. 2.8 a bit more in detail, we find that at the end of the chaotic region,  $\lambda_m$  drops drastically, staying however positive. The corresponding time-series and phase plane plots, shown in Fig. 2.9 unveil an intermittent underlying dynamical behavior, where periodic-like time-windows with exceedingly slow oscillations are interposed between the chaotic intervals. The intermittent quasi-regular oscillations appear when the trajectory revisits the destabilized limit-cycles, embedded into the chaotic attractor along the  $(-1, 1)$  diagonal (compare the phase plane projections shown in the right panel of Fig. 2.9 and panel (c) of Fig. 2.7, respectively).

## 2.4 Hopf bifurcations in the prototype system

In the previous sections we have discussed 2- and 4-dimensional examples of prototype systems (2.4) with double-well generalized potential functions (2.9). As we have seen, the key mechanism for generating limit-cycle oscillations is the control of energy uptake and dissipation around the minima of the potential. This view allows for a mechanistic understanding of how the limit cycle attractors are created.

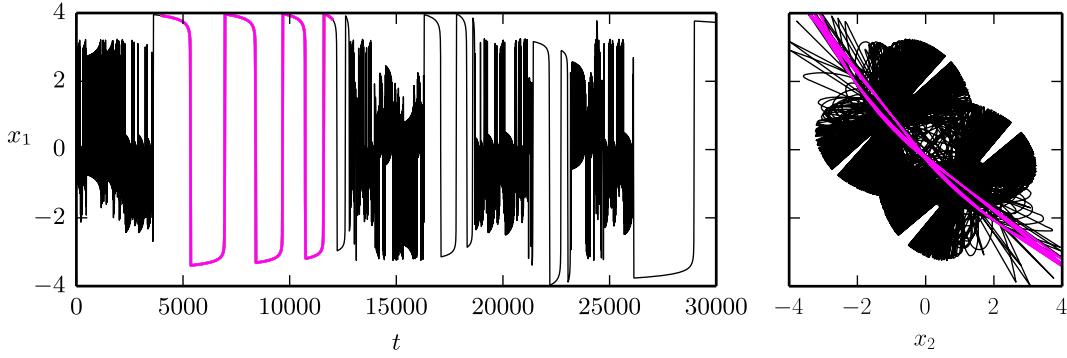


**Figure 2.9:** *Intermittent chaotic dynamics for the same system and parameters as in Fig. 2.8, setting now  $\mu_1 = 0.34$ . **Left:** Periodic-like window, indicated by the magenta color in the time-series plot of the  $x_1(t)$  variable. Note the different time-scales involved. **Right:** Phase space projection of the same trajectory to the  $(x_1, x_2)$  plane. The time window of the slowly oscillating dynamics, corresponding to the  $t_p = [4 \cdot 10^3, 12 \cdot 10^3]$  interval from the left is indicated here by the orbit-segment of the same color.*

Here, we provide an analytical proof of the Hopf bifurcations in case of general  $2d$ -dimensional prototype systems. In particular, we show that the energy uptake around the minima leads to the destabilization of the stable focus-type fixpoints, via turning them into repelling foci.

The fixpoints  $\mathbf{p}^*$  of the prototype system defined by Eq. (2.4) correspond to local minima and maxima of the potential function  $V(\mathbf{x})$  and vanishing velocity  $\mathbf{y}$ ,

$$\mathbf{p}^* = (\mathbf{x}^*, \mathbf{y}^*), \quad \mathbf{y}^* = 0, \quad \left. \frac{\partial V(\mathbf{x})}{\partial x_i} \right|_{\mathbf{x}^*} = 0.$$

The stability of the fixpoints (see Sec. 1.1.3) is determined by the eigenvalues of the Jacobian matrix  $\mathbf{J}$ , which can be expressed in terms of block matrices:

$$\mathbf{J}(\mathbf{p}^*) = \begin{pmatrix} \mathbf{O}_d & \mathbf{I}_d \\ -\mathbf{H}_d & a\mathbf{I}_d \end{pmatrix}, \quad (2.16)$$

where the friction function is denoted by  $a = f(V)$ . The  $\mathbf{O}_d$  and  $\mathbf{I}_d$  are  $d$ -dimensional zero and identity matrices, respectively, while  $\mathbf{H}_d$  defined by

$$(\mathbf{H}_d(\mathbf{x}^*))_{ij} = \left. \frac{\partial^2 V(\mathbf{x})}{\partial x_i \partial x_j} \right|_{\mathbf{x}^*} \quad (2.17)$$

is the Hessian matrix of the potential  $V(\mathbf{x})$ , evaluated at the respective critical point  $\mathbf{x}^*$ . Note that the Hessian  $\mathbf{H}_d$  is a symmetric matrix, hence all of its eigenvalues are real,  $\gamma_i \in \mathbb{R}$ . Furthermore, it can be used to determine whether a critical point is local maximum, local minimum, or a saddle point. If the Hessian is positive/negative definite at  $\mathbf{x}^*$ , the critical point is an isolated local minimum/maximum. On the other hand, if the Hessian has both positive and negative

eigenvalues  $\gamma_i$  then  $\mathbf{x}^*$  is a saddle point of the function.

The eigenvalues of the Jacobian  $\mathbf{J}$  are the solutions of the equation:

$$\det(\mathbf{J} - \lambda\mathbf{I}_{2d}) = \begin{vmatrix} -\lambda\mathbf{I}_d & \mathbf{I}_d \\ -\mathbf{H}_d & (a - \lambda)\mathbf{I}_d \end{vmatrix} = \det(-\lambda(a - \lambda)\mathbf{I}_d + \mathbf{H}_d) = 0, \quad (2.18)$$

where we used the properties of square block matrices. Introducing the notation

$$\gamma = \lambda(a - \lambda), \quad (2.19)$$

the determinant may be reduced to the

$$\det(\mathbf{J} - \lambda\mathbf{I}_{2d}) = \det(\mathbf{H}_d - \gamma\mathbf{I}_d) = \prod_{i=1}^d (\gamma - \gamma_i) = 0 \quad (2.20)$$

characteristic polynomial, expressed in terms of the  $d$  eigenvalues  $\gamma_i$  of the Hessian matrix. Solving Eq. (2.19), the  $2d$  eigenvalues of the Jacobian  $\mathbf{J}$  can be given as

$$\lambda_i^\pm = \frac{1}{2} \left( a \pm \sqrt{a^2 - 4\gamma_i} \right). \quad (2.21)$$

Therefore, the stability of the fixpoints  $\mathbf{p}^*$  is determined by the eigenvalues of the Hessian and by the friction function  $a = f(V)$ :

- Saddles and local maxima of the potential function  $V(\mathbf{x})$ , characterized by (at least one)  $\gamma_i < 0$ , are saddle-type fixpoints of the dynamical system (2.4), always having a corresponding positive eigenvalue  $\lambda_i^+ > 0$ .
- Local minima of the potential, with  $\gamma_i > 0$ , are stable fixpoints when energy is dissipated around them, viz. for negative friction function  $a = f(V(\mathbf{x}^*)) < 0$ .
- Hopf-bifurcation occurs, with  $\lambda_i^\pm = \pm i\sqrt{\gamma_i}$ , when the friction term changes sign, viz. for  $a = f(V(\mathbf{x}^*)) = 0$ .

Stable oscillations can hence be generated by the destabilization of the fixpoint attractors, via smoothly changing from dissipation to energy uptake in the neighborhood of the minima, using locally decreasing friction functions,  $f'(V(\mathbf{x}^*)) < 0$  (compare Fig. 2.4 and 2.8).

Note that for higher dimensional systems with  $d \geq 2$  the Hopf bifurcation is degenerate [54], since all pairs of eigenvalues are crossing the imaginary axis simultaneously,  $\text{Re}(\lambda_i^\pm) = 0$ . Hence, birth of higher dimensional tori or of multiple limit cycles may be expected [75]. This is the case for the 4-dimensional prototype system as well, the generated second branch of limit cycles is, however, only stable in the closed vicinity of bifurcation, as shown in Appendix B.

## 2.5 Discussion

In this chapter, we introduced a new class of prototype dynamical systems (2.4), which allows for the creation of coexisting fixpoint, limit-cycle and chaotic attractors. The phase space of the generalized Liénard-type system is spanned by the  $d$ -dimensional coordinates  $\mathbf{x}$  and the corresponding velocities  $\mathbf{y}$ . The generation of multiple attractors is achieved by controlling the regions with energy uptake and dissipation. Considering potential functions  $V(\mathbf{x})$  with multiple local minima, limit-cycle and chaotic attractors may be created by the destabilization of the fixpoints corresponding to the minima of the potential, via introducing a region with energy uptake in their neighborhood. That is possible when the generalized friction function  $f(V)$  depends explicitly on the potential  $V$ .

It is generally considered a difficult task to construct dynamical systems with a predefined number of attractors, placed in predefined regions of the phase space [69]. As a partial solution of this problem, we proposed a generic class of potential functions (2.9), characterized by a fixed number of local minima, with preset positions and heights. Using the friction term  $f(V)$  one may determine the type of the attractors corresponding to each of the minima of the potential, by suitably setting the relative height of the minima.

Using simple double-well potentials with one, respectively two spatial dimensions, we have shown that a whole cascade of limit cycle bifurcations can be produced either via defining alternating regions of energy uptake and dissipation, or, as in the case of the 4-dimensional prototype system, via symmetry breaking and period-doubling bifurcations leading to chaos. In case of the chaotic attractor, intermittent dynamics has also been observed. We have shown that the generation of limit cycles via destabilizing the fixpoint attractors does not depend on the particular shape of the potential function. The only requirement is the existence of a finite number of local minima. Hence, one could consider for example the biquadratic version

$$V(\mathbf{x}) \rightarrow (\mathbf{x} - \mathbf{x}_1)^2 (\mathbf{x} - \mathbf{x}_2)^2 \quad (2.22)$$

of the double-well potential (2.12). We have not studied in detail the bifurcation diagram of the system, we have checked, however, that it would lead to qualitatively similar scenario to the one presented in Fig. 2.8. We found that when using the linear friction function  $f_1(V)$ , as defined by Eq. (2.6), for increasing values of the control parameter  $\mu_1$ , spatially separated, merging, and symmetry breaking limit cycles can also be observed. Furthermore, for extended regions with energy uptake in the potential well (2.22) chaotic behavior can also be generated.

Multistable systems play an important role in modeling several complex phenomena, ranging from neural dynamics and chemical reactions, to climate dynamics and social systems [5]. Chaotic systems with coexisting attractors has been proposed as reliable random bit generators, but also allow for the experimental study

of chaotic synchronization [67]. The here proposed prototype system (2.4) not only allows to generate multistability, but it also enables the control of the relative position of the attractors (in the  $x$  subspace), either via keeping them spatially separated or embedding limit cycles and stable fixpoints in each other. Furthermore, as a future perspective we note that the metadynamics of the attractors [76] may also be investigated by adding a (maybe slow) dynamics to the positions  $x_m$  or the heights  $V_m$  of the minima.

The behavior of complex systems is often modeled by dynamical systems, for which the equations of motion are derived from higher order generating principles [77, 78]. These methods involve the construction of a general potential or energy functional [79, 80], the equations of motion then being defined in terms of a gradient decent rule [81]. When the dynamics is derived from a single global objective function, the resulting ODE corresponds to a gradient system, for which no complex attractors can exist, other than stable fixpoints [1]. To allow more complicated dynamics, such as regular or chaotic oscillations, one may consider additional equations of motions derived from a second generating functional, inducing objective function stress [52]. The prototype system (2.4) may hence provide an alternative solution for by-passing this problem, due to the inherent inertia of the dynamics, resulting from the mechanistic design procedure. Introducing regions of energy uptake and dissipation by suitably chosen friction functions  $f(V)$ , complex dynamics may be generated in a controlled manner, which is in turn also shaped by the energy functional.



## Chapter 3

# Transient-state dynamics in neural networks

Sándor, B., & Gros, C. (2017) *Complex activity patterns generated by short-term synaptic plasticity*. ESANN 2017 Proceedings, ISBN 978-2-87587-038-4.

One of the most intriguing unsolved problems of present-day science concerns the understanding of the nervous systems as a complex adaptive dynamical system [1]. The dynamical modeling of neural networks raises however new challenges for the field of classical dynamical systems theory [8].

In this chapter we argue however that investigating the repertoire of dynamical behaviors of the nervous system and the key ingredients in generating these specific dynamics may provide a complementary approach to the computational neuroscience methodology [82]. Furthermore, it might also lead to the development of new valuable methods for the field of nonlinear dynamics. In this context, we introduce here a new class of recurrent neural networks producing transient-state dynamics [9] without time dependent external stimuli. We show that short-term synaptic plasticity [10] may play an important role in generating transient-states lasting from several hundreds of milliseconds to seconds.

We start by presenting briefly the main challenges in studying the brain in terms of dynamical systems theory, discussing also the concept of transient-state dynamics as a typical behavior in several cognitive processes [3]. Furthermore, the standard models of rate encoding neurons and short-term synaptic plasticity are also introduced. That is followed by the bifurcation analysis of the system as a function of a constant global input, allowing for a deeper understanding of how the transient states and the former attractors of the network are related. Finally, we present examples of transient-state dynamics in larger random networks, corresponding either to regular limit-cycle oscillations or to chaotically fluctuating activity patterns.

### 3.1 Introduction to the modeling of neural networks

Computational neuroscience, a field engaged in investigating the nervous system by means of computational modeling, relies on several different tools and methods of other scientific disciplines, such as biophysics, information theory, dynamical systems, machine learning, etc. The dynamical modeling of the brain has a long standing history with many interesting results, however, traditional methods of dynamical systems theory are limited in their applicability when it comes to the understanding of the nervous system.

On one side, the brain has to deal with a great deal of input signals, hence further developments of non-autonomous dynamical systems theory [25] is required. On the other side, even single neurons might show very complex dynamical behaviors [83, 84]. Hence, an effective modeling of neural networks is difficult due to several reasons: a huge number of variables and control parameters exist only with a partial knowledge of their importance and role, and the general principles governing the dynamics as well as the network structure (the connectomics of the brain) are also not fully known (for a review of dynamical principles in neuroscience see Refs. [8] and [85]).

As a possible resolution for the latter problem several different generating functionals have been proposed to derive the equations defining the network dynamics in a top-down manner. Promising results have been achieved based on the optimization of the firing rate distributions [52, 81], or on the stationarity principle using the Fisher information [86, 87]. Furthermore, other objective functions, such as the free energy for the surprise minimization [79, 88], or the predictive information [89] for generating explorative and playful behavior with autonomous robots [12] have also been considered. Bottom-up approaches, focusing on the local biophysical and biochemical processes involved in the signal transmission or in the homeostasis of neurons have also been successful in building phenomenological models which can accurately reflect many experimental findings [90, 91].

The success of either modeling approaches depends on the universality of the underlying principles governing the dynamical behavior of biological neural networks. The methods of dynamical systems theory may help in unveiling these guiding laws by finding the common features even in seemingly different models [82]. Autonomous neural systems are typically dissipative, allowing hence for the presence of attractors which in turn provide robustness against noise. Attractors also guarantee some degree of structural stability for small parameter variations, while bifurcations leading to dynamical switching between different behaviors may serve as implementations of higher order control mechanisms [84]. Furthermore, input driven neural networks typically use phenomena such as synchronization, intermittency or resonance [8]

### 3.1.1 Transient-states for cognitive processing

The most well-known cognitive-type models are multistable Hopfield-type networks [92, 93], characterized by an energy function with many local minima, allowing hence for multiple coexisting fixpoint attractors. In the framework of associative memory [94], the idea behind the “computation with (fixpoint) attractors” concept is based on the transformation of a given input signal, defining some initial condition, to a desired output corresponding to a fixpoint attractor. Though attractor networks with stable fixpoint states have been successful in modeling associative memory related cognitive phenomena, further developments and alternative concepts are required for understanding neural processing mechanisms characterized by a spatiotemporal dynamics [3].

Experimental results suggest that sequences of transient states, ones in which no stable fixpoint equilibrium is reached, may better describe the behavior of neural networks [95–97]. For example, the resting state network dynamics, i. e. when the brain is not performing any particular task, shows slowly fluctuating spatiotemporal patterns of consistently activated and deactivated brain regions [2]. Neural ensembles of the sensory cortex also produce centrally generated dynamic sequences of states, evoked by natural stimuli. Furthermore, these state sequences predict sensory stimuli better than other techniques not using this information [98]. Persistent reverberations in selective neural populations, corresponding to metastable activity states, are considered to be the neural correlates of working-memory, also observed during decision making tasks [50,99]. Finally, place cells in hippocampus [100] and the high vocal center neurons of songbirds [101] also exhibit sequential dynamics.

These transiently activated states, lasting typically from several hundreds of milliseconds to seconds [8, 98], can generally be seen as dynamical images of interacting “brain modes” or “states of mind” [102]. Understanding the temporal evolution of these states is hence crucially important for the modeling of information flows in the brain (for a review of information flow dynamics see Ref. [103]).

Several neural network models have been proposed for generating transient-state dynamics, as discussed in Sec. 1.1.5 of **Chapter 1**. In the presence of incoming input signals, viz. in the nonautonomous case, the dynamics may be non-stationary, hence attractors may never be reached exactly [3, 50]. In this case, sequential switching between transient states may be constructed based on the idea of following a heteroclinic channels [45] or contours [47] connecting saddle type fixpoints or limit cycles in the phase space. For autonomous systems, transient-state dynamics corresponds to a single complex, periodic or chaotic attractor in the full state space of the network. One may hence consider attractor networks coupled to slow, local variables [9]. Due to the additional slow dimensions, the former attractors reduce to slow manifolds, acting like transiently attracting states [42].

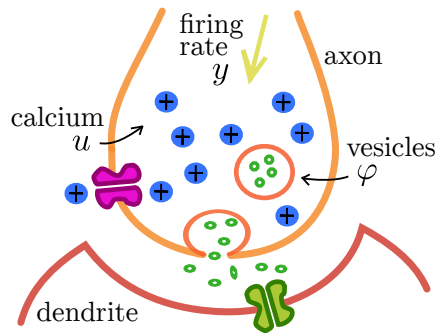


**Figure 3.1:** Sketch of a chemical synapse, showing the presynaptic bouton of the axon, the synaptic cleft and the post-synaptic dendrite. Illustrated is the release of neurotransmitters from the vesicles  $\varphi$ , a process triggered by the increase of  $\text{Ca}^{2+}$  concentration  $u$  as a result of the elevated presynaptic neural firing rate  $y$ .

This metastability may also be interpreted in terms of a dynamically changing attractor landscape [104].

Here, we follow the latter approach in generating transient-state dynamics in autonomous recurrent neural networks. In particular, we incorporate short-term synaptic plasticity in the network, which plays an important role in the behavior of biological neural systems [10]. Hence, in the following section we provide a brief summary of the terminology employed in the field, which is followed by the introduction to the mathematical models used for constructing the differential equations governing the dynamics of the individual neurons and their interactions in a network.

### 3.1.2 Neurons and synaptic plasticity

Neurons are responsible for the integration and transmission of electrical and chemical signals in the nervous system [105]. This information transmission is realized via synapses, which are electrical or chemical connections between the axon of the sender (presynaptic), and the dendrite of the target (postsynaptic) neuron. Here we focus on chemical synapses, which use neurotransmitters (amino acids, peptides) in order to allow the transmission of signals. For an illustration of a chemical synapse see the sketch in Fig. 3.1.

Neurotransmitters are stored in synaptic vesicles, which are gathered above the membrane of the presynaptic boutons (axonal swellings). When the neuron generates an action potential, the voltage gated calcium channels open. Since the concentration of  $\text{Ca}^{2+}$  ions is much higher outside of the cell than inside, calcium flows into the terminal. As a result of that, among many other processes, neurotransmitters are released and diffused across the synaptic cleft where they bind to the corresponding receptors in the membrane of the dendrite.

Depending on the type of the released neurotransmitters the postsynaptic neurons may be influenced either in an excitatory (glutamate neurotransmitters) or inhibitory (GABA neurotransmitters) way [106]. The dendrites of neurons typically gather incoming pulses from thousands of other neurons. If the integrated excitatory influence is greater than the inhibitory one, the postsynaptic neurons will also fire, generating their own action potential.

The connections between neurons are not static, as time evolves new synapses are created, furthermore, their effectiveness is also varying. The synaptic efficacy measures the impact of a firing presynaptic neuron on the activity of the postsynaptic one. Synaptic plasticity refers, hence, to the process of changing synaptic efficacy or synaptic strength. Other quantities, corresponding to intrinsic parameters in neurons, may also be time-dependent. The adaption of internal parameters is referred to as internal plasticity. Several different plasticity mechanisms are known to exist, some are characterized by time scales of seconds, while others may have long lasting effects. Long-term depression and long-term potentiation, mainly occurring at excitatory synapses [107], are plasticity mechanisms lasting minutes or more [108]. More recent experimental developments have shown, however, that the effects of short-term plasticity can only be observed on reasonably shorter time scales [109]. The different forms of synaptic plasticity are believed to play a crucial role in learning and in cognitive processes related to short- and long-term memory.

*Short-term synaptic plasticity (STSP)* refers to the phenomenon in which the effective synaptic strength, viz. the synaptic efficacy is transiently affected by the history of the presynaptic activity [109, 110]. Elevated presynaptic firing may have two opposite effects on the signal transmission properties of synapses. Due to the synaptic signaling, the influx of  $\text{Ca}^{2+}$  ions into the presynaptic axon terminal increases the release probability of neurotransmitters, resulting in a short-term facilitation. On the other hand, this leads to depletion of neurotransmitters, as show by Fig. 3.1, stored in the vesicles of the presynaptic bouton [111]. The two phenomena have been observed in various cortical regions and for different animals, showing a great diversity in properties and in the way they interact both in excitatory [112] and inhibitory [113] synapses. The time scale of the STSP dynamics is an important inherent property, determining whether short-term facilitation or depression is the dominating behavior [114]. The induced modifications are temporary, lasting from hundreds to thousands of milliseconds, hence, in a persistent absence of presynaptic activity, the synaptic efficacy returns to its baseline level. Therefore, the term transient synaptic plasticity may better describe the actual phenomenon.

### 3.1.3 Rate-encoding neurons and the full-depletion model

For modeling purposes of neural dynamics, the firing, viz. the activity of a neuron can typically be quantified in two ways [115]. When the precise timing of each emitted spike is of relevance for the phenomena under investigation, i. e. when

the important time scales are of the order of a few milliseconds, the generation of individual spikes has to be modeled. These models of neurons we may term as time-encoding neurons. In case of longer time scales, the neural activity can be represented by the firing rate of the individual neurons, which corresponds to the frequency of the emitted spikes. Rate-encoding neurons are generally imagined as point neurons. Alternatively, one may compute the average firing frequency of spiking neural populations and represent by the firing rate an ensemble activity .

As a simple model for rate-encoding point neurons we consider nonlinear firing-rate response curves [105]. The activity of a neuron, represented by the normalized (dimensionless) firing rate  $y \in [0, 1]$ , is given here by a nonlinear transformation,

$$y = y(x) = \frac{1}{1 + e^{a(b-x)}}, \quad (3.1)$$

of the internal state  $x$  of the neuron, associated with the membrane potential  $x$  [116]. The function (3.1), also called as transfer or activation function, has a sigmodial shape, characterized by two intrinsic parameters [105]. The threshold  $b$  determines the transition point from low activity to high activity level, as illustrated by Fig. 3.2, while the gain  $a$  is setting the slope of the function at  $x = b$ . The dynamics of the membrane potential  $x$  is regulated by the incoming inputs from the other neurons [116]:

$$\dot{x} = -\Gamma x + \sum_i \omega_i y_i, \quad (3.2)$$

where  $\omega_i$  is the synaptic strength connecting to neuron  $i$ . Excitatory and inhibitory inputs can be modeled by positive  $\omega_i > 0$ , respectively negative  $\omega_i < 0$  weights. In the absence of input, with  $y_i = 0$ , the membrane potential relaxes to zero on a time scale defined by the leak-rate  $\Gamma$ . We note that other transfer functions, e. g.  $y(x) = \tanh(x)$ , are also employed in the field [105, 117].

According to Dale's principle, the outgoing synapses of neurons are either excitatory or inhibitory [106]. In the computational modeling of neural networks this constraint is often lifted, allowing for both type of connections. This can be considered a simplification of cases, when there is a third neuron involved in the signal transmission, mediating the type of the influence (e. g. the first neuron is exciting an inhibitory neuron, which in turn then inhibits another one).

Similarly to the quantification of the neural activities, in the computational and theoretical modeling of neural plasticity mechanisms two major approaches have been developed, which are aligned along the rate-encoding, respectively the time-encoding directions. The early time plasticity rules have been mostly proposed in terms of firing rates, such as the famous Hebb's rule [118], the Oja's rule [119], or the BCM rule [120]. The plasticity mechanisms which effectively depend on the exact timing of individual spikes, such as spike-timing dependent plasticity, can however only be described on the level of time-encoding rules [121, 122].

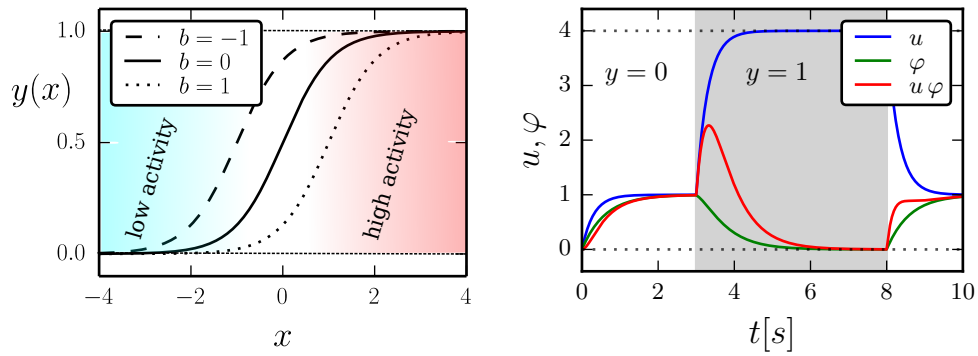


**Figure 3.2:** Transfer function and the dynamics of the full-depletion model (3.3). **Left:** The sigmoidal-shaped transfer function  $y(x)$ , defined by Eq. (3.1), for  $a = 1$  and different threshold values  $b$ . The low- and high-activity regions are color-coded respectively with blue and red gradients for visualization purposes. Note that the maximal activity is normalized to unity,  $y(x) \in [0, 1]$ . **Right:** The relaxational dynamics of the calcium  $u$  and neurotransmitter concentration  $\varphi$ , together with the effective synaptic weight factor  $u\varphi$ , as a function of time as defined by the full-depletion model (3.3) for  $U_{\max} = 4$ ,  $T_u = 300$  ms and  $T_\varphi = 600$  ms. For high / low presynaptic activity, with  $y = 1$  (in the gray shaded interval) /  $y = 0$  (otherwise) respectively, the target levels are  $u \rightarrow U_{\max} / 1$  for the calcium and  $\varphi \rightarrow 0 / 1$  for the neurotransmitter concentration.

Hereinafter, we turn our attention to the modeling of short-term synaptic plasticity with rate-encoding neurons, discussing a minimal set of differential equations able to capture the essential dynamical behavior observed in experiments. The first phenomenological model incorporating both effects of the increased release probability of neurotransmitters and their depletion in time has been proposed by Tsodyks and Markram [114, 123]. Recently, it has been employed in several studies of neural network modeling, showing a wide range of complex phenomena [124, 125].

The *full-depletion model*, a modified version of the original Tsodyks-Markram rules for presynaptic plasticity, allows for the complete exhaustion of neurotransmitters [51]. As discussed in Sec. 3.1.2 short-term synaptic plasticity is regulated mainly by the dynamical interaction of three quantities: the amount of  $\text{Ca}^{2+}$  ions in the presynaptic terminal  $u$ , entering via the voltage-gated calcium channels as a result of the elevated presynaptic activity  $y$ , and the fraction of available neurotransmitters  $\varphi$  to be released to the synaptic cleft. Here, the interaction of incoming spikes, calcium flow and neurotransmitter release is formulated in terms of a relaxational dynamics:

$$\begin{aligned} \dot{u} &= \frac{U(y) - u}{T_u} & U(y) &= 1 + (U_{\max} - 1)y \\ \dot{\varphi} &= \frac{\Phi(y, u) - \varphi}{T_\varphi} & \Phi(y, u) &= 1 - \frac{uy}{U_{\max}} \end{aligned} \quad (3.3)$$

to the respective target functions  $U(y)$  and  $\Phi(y, u)$ , and characterized by the respective time scales  $T_u$  and  $T_\varphi$ .

Note that for prolonged high presynaptic activity, the target functions reduce to  $U(1) = U_{\max}$  and  $\Phi(1, U_{\max}) = 0$ , where  $U_{\max}$  defines to the maximal  $\text{Ca}^{2+}$  level. On the other hand, in case of low activity  $U(0) = 1$  and  $\Phi(1, 1) = 0$ , hence, the model (3.3) allows for a direct control of the long term dynamics. Similarly to the Tsodyks-Markram rules [125], the effective synaptic weight is determined by the product of the two variables,

$$\omega^{\text{eff}}(t) = \omega u(t)\varphi(t). \quad (3.4)$$

The dynamics of the model is shown in the left plot of Fig. 3.2, illustrating the behavior for high and low activity time intervals, as discussed above. In the high activity region the synaptic transmission is transiently facilitated, in terms of the  $u\varphi$  product reaching a factor of two increase, which is followed by the a depression phenomena, with  $u\varphi \rightarrow 0$ , corresponding to the full depletion of neurotransmitters. Therefore, the model allows even the complete blocking of signal transmission corresponding to an effective decoupling of neural interaction.

We note, however, that setting the  $T_u$  and  $T_\varphi$  parameters in Eq. 3.3 according to the experimentally determined [112, 113] parameters of the Tsodyks-Markram model [114], we find a similar dynamical behavior albeit on a longer time scale. Therefore, a biologically more realistic simulation may be realized by optimizing the parameters for a better matching between the  $u(t)\varphi(t)$  curves generated by the full-depletion model (see Fig. 3.2) and the ones corresponding to the experimental measurements. Since we are interested in the generation of transient-state dynamics by using STSP in a recurrent neural network, we do not aim for the exact reproduction of the experimental finding.

## 3.2 Transient-state dynamics generated by STSP

It has been proposed already that dynamic synapses may be used to extend attractor neural networks for representing time-dependent stimuli [126, 127]. Short-term facilitation is believed to play an important role in working memory, since the presynaptic calcium level provides a cheap memory buffer for up to thousands of seconds [124]. Since there is evidence for short-term synaptic plasticity between locomotor network interneurons, it is suspected to be an important functional component of spinal cord networks [128], where synaptic depression may be involved in the maintenance and modulation of motor programs [129]. In the context of artificial systems, STSP can generate complex behavior patterns, which may be used as motions primitives [15, 130]. This latter aspect will be demonstrated in detail in **Chapter 4** by constructing autonomously active simulated robots.

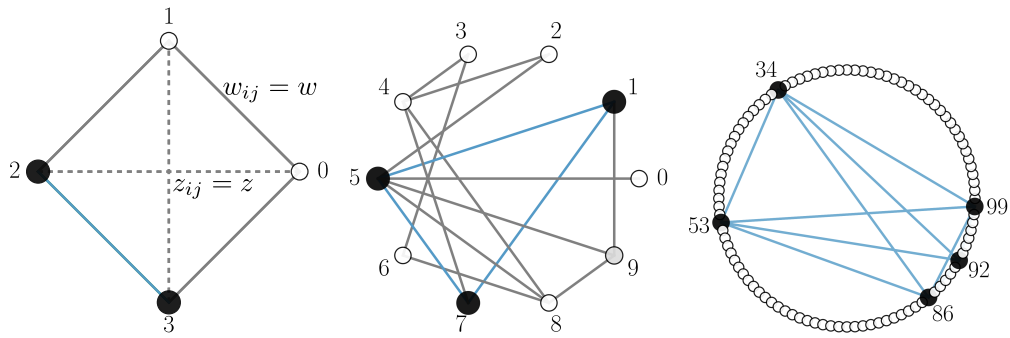


**Figure 3.3:** Sketches of the networks of  $N = 4/10/100$  neurons (left / middle / right) illustrated with one active clique (black nodes connected by blue lines). Shown are the connections (excitatory  $w_{jk}$  and inhibitory  $z_{jk}$  / only excitatory / only of the active clique). Active / inactive nodes are depicted by filled / open circles, and excitatory / inhibitory links by continuous / dashed lines. The numbers correspond to the index of the respective nodes.

### 3.2.1 Attractor networks with clique encoding

Here, we consider attractor neural networks [131] characterized by multiple co-existing attractor states, corresponding to active excitatory cliques of neurons. We show that the presence of short-term synaptic plasticity can destabilize these fixpoint attractors, generating transient-state dynamics in terms of emerging limit cycles and chaotic attractors [51].

Clique encoding is based on the idea that fully connected excitatory subnetworks can stabilize themselves via their mutual excitation [9]. To demonstrate this, we consider recurrent networks with a complementary excitatory-inhibitory graph topology, i. e. a fully connected network, where the bidirectional connections between any two neurons  $j$  and  $i$  is either excitatory or inhibitory, denoted here as  $w_{ij} > 0$  and  $z_{ij} < 0$  respectively. No self-connection is allowed  $w_{ii} = z_{ii} = 0$ .

Three examples of such network structures, respectively with  $N = 4/10/100$  nodes, are presented in Fig. 3.3. The  $N = 4$  neuron network consists of a ring of excitatory connections with  $w_{i,i+1} = w$ , while the inhibitory ones are connecting the second order neighbors with  $z_{i,i+2} = z$  (assuming periodic boundary conditions for the indexes). It is, hence, characterized by a  $C_4$  rotational symmetry.

The  $N = 10$  and  $N = 100$  site networks are constructed, on the other hand, by creating an Erdős-Rényi random graph [1, 132] of excitatory links with connection probability  $p = 0.3$ , adding the inhibitory links afterwards as complementary to get a fully connected structure. The advantage of using clique encoding networks is the high number of possible cliques. For Erdős-Rényi-type random graphs, the number

of cliques consisting of  $K$  nodes is statistically given by [1]

$$\binom{N}{K} p^{K(K-1)/2} (1 - p^K)^{N-K}, \quad (3.5)$$

where the first term denotes the number of  $K$ -combinations, and  $p$  is the probability of any two nodes being connected. As a straight-forward application of Eq. (3.5), we see that statistically there are about 2.6 cliques of size 3 for a  $N = 10$  site random network with  $p = 0.3$ . Note that the same calculation for  $N = 100$  nodes would yield almost 307 cliques. These simple examples also illustrate the high number of all possible cliques for networks consisting of millions of neurons.

Considering rate-encoding neurons and employing Eqs. (3.2) and (3.1) for the activity dynamics and the transfer function respectively, together with the network structures presented above, we find that the systems are multistable (cf. Sec. 1.1.4; for the similar Hopfield-networks see [92, 131]). The stable fixpoint attractors of the networks correspond to active neurons with  $y_i \approx 1$ , which form cliques in terms of their excitatory connections. Examples of such active cliques are shown in Fig. 3.3. Note that the formation of single active cliques is possible whenever the inhibitory connections are stronger  $|z_{ij}| \gtrsim 2w_{ij}$ . In this case the members of an active clique are mutually exciting each other, while suppressing the activities of neurons to zero. For more balanced excitatory-inhibitory connections with  $|z_{ij}| \approx w_{ij}$ , the stable fixpoints turn into co-activated clique states.

Short-term synaptic plasticity may be added now to the network by replacing the previously static synaptic weights in Eq. (3.2) with the dynamic ones, as defined by Eq. (3.4). To simplify the system, we assume that all neurons are characterized by the same parameters, including the STSP ones. Generally, every synapse, connecting neuron  $j$  to neuron  $i$ , is characterized by two presynaptic variables,  $u_{ij}$  and  $\varphi_{ij}$ . Note, however, that their dynamics, defined in Eq. (3.3), is only influenced by the presynaptic activity  $y_j = y(x_j)$  (cf. Fig. 3.1). Therefore, as a result of the common driving signal, all outgoing connections of neuron  $j$  get synchronized in the asymptotic limit, allowing for a simplified notation,  $u_{ij} \rightarrow u_j$  and  $\varphi_{ij} \rightarrow \varphi_j$ . To further reduce the complexity of the problem, here, we keep the excitatory connections static, hence the effective synaptic weights may be written as:

$$w_{ij}^{\text{eff}}(t) = w_{ij}, \quad z_{ij}^{\text{eff}}(t) = z_{ij} u_j(t) \varphi_j(t). \quad (3.6)$$

The number of STSP variables scales linearly with the number of neurons, in contrast to many other forms of synaptic plasticity, which are affected by both pre- and postsynaptic activities.

Hence, the full dynamical system governing the activity of  $N$  neurons with STSP spans a  $n = 3N$  dimensional phase space:

$$\begin{aligned}\dot{x}_i &= -\Gamma x_i + \sum_{j=0}^{N-1} (w_{ij} y_j + z_{ij} u_j \varphi_j y_j) + I \\ \dot{u}_i &= \frac{U(y_i) - u_i}{T_u} \\ \dot{\varphi}_i &= \frac{\Phi(y_i, u_i) - \varphi_i}{T_\varphi},\end{aligned}\tag{3.7}$$

where the target functions  $U(y_i)$  and  $\Phi(y_i, u_i)$  are defined as in Eq. (3.3). The additional parameter,  $I$ , denoting a constant global input to the network, will be used as a control parameter of the system.

The phase space of system (3.7) is infinite in the membrane potential variables  $x_i$ . It is, however, sometimes more convenient to work with bounded spaces. Hence, one may also define the system in terms of the firing rates  $y_i$ , by rewriting the membrane potential dynamics as  $\dot{y}_i$ . Note that despite the nonlinear activation functions  $y(x)$  this results in an equivalent dynamical systems, preserving the invariant sets, the attractors, as well as their stability. Therefore, we use the firing rates  $y_i$  and the membrane potentials  $x_i$  interchangeably in the explanation of results. For a detailed proof and discussion of the effects of nonlinear transformations in terms of stability and invariant quantities see Appendix A.

Due to the additional STSP variables, the original fixpoint attractors, corresponding to active cliques of excitatory connections (as illustrated in Fig. 3.3), may either be destabilized or completely destroyed. In case of a slow STSP dynamics, with  $\dot{\varphi}_i \ll \dot{x}_i$  or  $\dot{u}_i \ll \dot{x}_i$ , the former attractors correspond, however, to slow-manifolds (complex piece-wise smooth hypersurface segments) embedded to the full  $n = 3N$  dimensional phase space [42]. The trajectory may, hence, approach these metastable states, slowing down only temporarily in their neighborhood [9]. Since the dynamical system (3.7) is autonomous, with a negative phase space contraction rate, defined by Eq. (1.3),

$$\sigma = \nabla \cdot \mathbf{f} = \sum_i \left( \frac{\partial \dot{x}_i}{\partial x_i} + \frac{\partial \dot{u}_i}{\partial u_i} + \frac{\partial \dot{\varphi}_i}{\partial \varphi_i} \right) = -\Gamma - \frac{1}{T_u} - \frac{1}{T_\varphi} < 0,\tag{3.8}$$

with  $\mathbf{f}$  denoting the RHS of (3.7), the system is strictly dissipative. This is true when self-connections are not allowed,  $w_{ii} = z_{ii} = 0$ , as for the clique encoding networks considered here. Therefore, the long-term behavior of system (3.7) is characterized by attractors (cf. Sec. 1.1.2).

In Fig. 3.4 we present two limit-cycle attractors for the case of the symmetric  $N = 4$  site network. We find that during these oscillations, 2-neuron cliques are re-activated sequentially, corresponding either to a back-and-forth switching of active

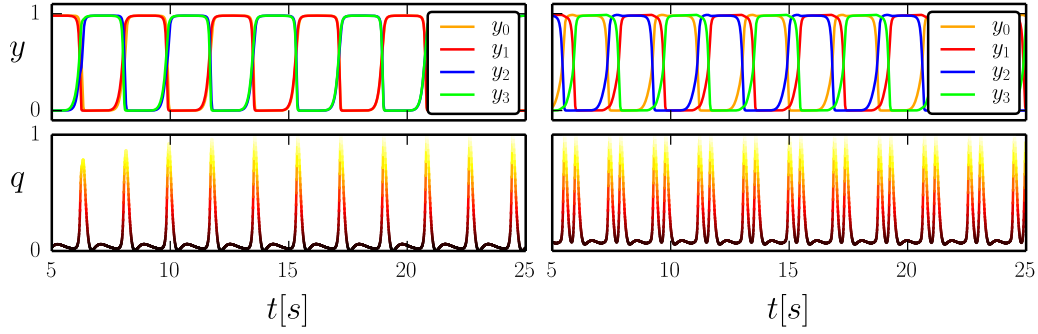


**Figure 3.4:** *Transient-state dynamics in the  $N = 4$  site symmetric network (see the left graph of Fig. 3.3). **Top:** The activity  $y_i$  of the neurons as function of time showing two examples of limit cycle solutions: with switching (left) and with traveling wave (right) dynamics. **Bottom:** The corresponding normalized speed  $q$ , see Eq. (3.9), of the flow. The parameters are  $\Gamma = 10 \text{ s}^{-1}$ ,  $a = 1$ ,  $b = 0$  for the neurons, and  $w = 40 \text{ Hz}$ ,  $z = -100 \text{ Hz}$ ,  $T_u = 300 \text{ ms}$ ,  $T_\varphi = 600 \text{ ms}$ ,  $U_{\max} = 4$  for the synapses, with no input  $I = 0$ .*

states, or to a traveling-wave-like propagation of an activity bump (similar to the one found in [127]):

$$[2, 3] \rightarrow [0, 1] \rightarrow \quad \text{and} \quad [2, 1] \rightarrow [1, 0] \rightarrow [0, 3] \rightarrow [3, 2] \rightarrow ,$$

where we indicated in brackets the indexes of neurons forming the transiently active cliques in the respective cycles.

The dynamics presented in Fig. 3.4 is characterized by plateaus of activities in the time-series of firing-rates  $y_i$ . The trajectory slows down in phase space, as it approaches these transient states. This slowing down can be quantified by calculating the speed of the flow  $q$ ,

$$q = Q/Q_{\max}, \quad Q = |\mathbf{f}(\mathbf{v})|^2, \quad \dot{\mathbf{v}} = \mathbf{f}(\mathbf{v}), \quad (3.9)$$

where  $\mathbf{v} = (\mathbf{x}, \mathbf{u}, \varphi)$  and  $\mathbf{f}$  is denoting the RHS of Eq. (3.7), while  $Q_{\max}$  is just a normalization factor, corresponding to the maximal absolute speed  $Q$  on the attractor. The former clique attractors of the network act as metastable states, where the normalized speed is approaching zero,  $q \rightarrow 0$  (see the bottom plot of Fig. 3.4). On the other hand,  $q$  peaks sharply when switching from one transient state to another.

### 3.2.2 Bifurcation analysis of the symmetric network

The  $N = 4$  site symmetric network is one of the smallest networks exhibiting transient-state dynamics. Additionally, due to its symmetric network structure, it also allows for a detailed bifurcation analysis. Combining analytical and computational methods we study the existing attractors as a function of a constant global

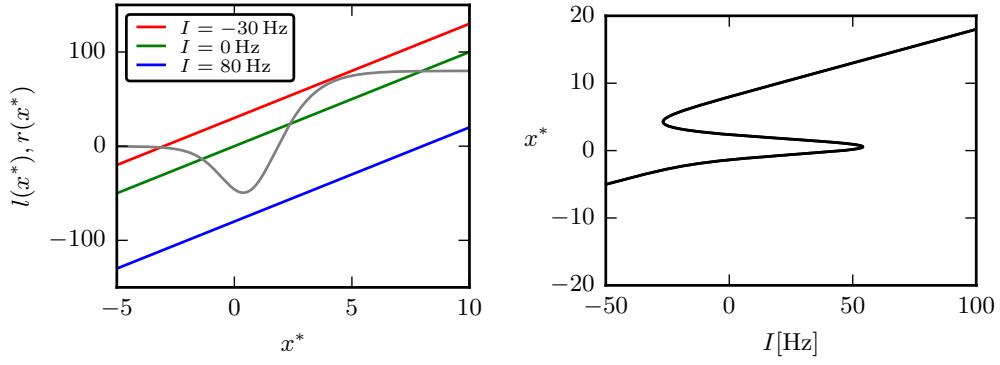


**Figure 3.5:** Symmetric solutions of Eq. (3.7) for the  $N = 4$  site network, illustrated in Fig. 3.3. **Left:** Graphical solution of the nonlinear fixpoint equation (3.10), showing the left- and right-hand-side functions,  $l(x^*)$  (gray curve) and  $r(x^*)$  (color lines) respectively, as defined by Eq. (3.11), for three different values of the input  $I$ . Note that  $l(x^*)$  is a linear function of  $I$ . The other parameters are as for Fig. 3.4. **Right:** The fixpoint solutions  $x^*$  corresponding to the intersection points of the curves plotted on the left, as a function of the input strength  $I$ . For  $I \in [-27 \text{ Hz}, 54 \text{ Hz}]$  three coexisting solutions are possible.

input, denoted by  $I$  in Eq. (3.7).

As the network is characterized by a  $C_4$  symmetry, first we look for the corresponding symmetric solution, i. e.  $x_i(t) = x^*$ ,  $u_i(t) = u^*$  and  $\varphi_i(t) = \varphi^*$  for all  $i \in \{1, 2, 3, 4\}$ . Fixpoint solutions of this type must fulfill the following set of nonlinear equations (cf. Eq. (3.7)):

$$\begin{aligned} \Gamma x^* - I &= (2w + zu^*\varphi^*) y^* \\ u^* &= 1 + (U_{\max} - 1)y^* \\ \varphi^* &= 1 - u^*y^*/U_{\max}. \end{aligned} \quad (3.10)$$

where  $y(x^*) = y^*$ . Note that the second and third expressions can be plugged into the first one, reducing the problem to one nonlinear equation. Denoting by  $l(x^*)$  and  $r(x^*)$  respectively the left- and right-hand-side functions of the first equation,

$$l(x^*) = \Gamma x^* - I, \quad r(x^*) = (2w + zu^*\varphi^*) y^*, \quad (3.11)$$

one may solve the problem graphically, looking for their intersection points, as illustrated by the left plot of Fig. 3.5. For low and high values of the control parameter  $I$  one finds a single fixpoint, while for intermediate input strengths, including  $I = 0$ , three fixpoint solutions are possible (see the right diagram of Fig. 3.5).

The solution illustrated in Fig. 3.5 already hints to some possible saddle-node bifurcations at the bending points of the S-shaped curve. On the other hand, as demonstrated by Fig. 3.4 for  $I = 0$  there are two further limit-cycle attractors in the phases space. To examine the stability of the fixpoints and investigate other possible

solutions and bifurcations of Eq. (3.7), we use numerical continuation methods [54].

The full bifurcation diagram of the  $N = 4$  site network as a function of varying input current  $I$  is presented in Fig. 3.6. The skeleton of the fixpoint curve is given by the symmetric solution of Eq. (3.10), as shown in Fig. 3.5. The lower / upper segments of this S-shaped curve are stable fixpoints, corresponding to states when all the neurons are active / inactive, with  $y(x^* > 2) \approx 1$  and  $y(x^* < -2) \approx 0$  (cf. Fig. 3.2), also called as up- and down-states. For intermediate input strengths  $I$  the symmetric solution breaks up into two branches via a Pitchfork bifurcation, corresponding to the active-clique states discussed previously. Note that the  $C_4$  symmetry allows for four such cliques, with the active neurons being  $[0, 1]$ ,  $[1, 2]$ ,  $[2, 3]$  and  $[3, 0]$  respectively. In the  $x_0(I)$  projection, used for Fig. 3.6, the  $[0, 1]$  and  $[3, 0]$  cases correspond to the upper, while the  $[1, 2]$  and  $[2, 3]$  states to the lower fixpoint branches.

The active-clique states lose their stability at  $I \approx -7.7$  Hz in a pair of supercritical Hopf-bifurcations, generating two small-amplitude limit cycles. That is followed by a series of limit-cycle bifurcations, involving homoclinic and saddle-node bifurcations of cycles, leading finally to the large-amplitude transient-state dynamics presented in Fig. 3.4. To understand this parameter region of small amplitude oscillations one may consider the 2-dimensional prototype system together with the double-well potential function, introduced in **Chapter 2**, which was designed to exhibit an analogous cascade of limit-cycle bifurcations (see Sec. 2.3.1 and compare the bottom-right diagram of Fig. 2.4). Since the here considered system is  $n = 12$  dimensional, we find an intermediate region of chaotic behavior as well (cf. Fig. C.1 in Appendix C).

The transient-state dynamics shown in Fig. 3.4 is realized in the form of stable limit cycles, while the fixpoints, corresponding to the stable-clique states in the absence of STSP, turn into saddle-focus-type equilibria (see the dashed lines in the right diagram of Fig. 3.6). These are, however, embedded in a slow manifold, composed of the fixpoints of the  $\dot{x}_i$  subsystem, in the limit of infinitely slow  $\dot{u}_i$  or  $\dot{\varphi}_i$  dynamics [42]. Therefore, the trajectory may approach the attracting parts of the slow manifold, never reaching them due to the finite  $T_u$  and  $T_\varphi$  time scales. In this sense the here presented approach is different from the ones based on the construction of heteroclinic channels [45], as discussed in Sec. 1.1.5. Furthermore, the saddle-focus points also disappear for  $I > 60$  Hz, providing an example of transient-state dynamics without saddles.

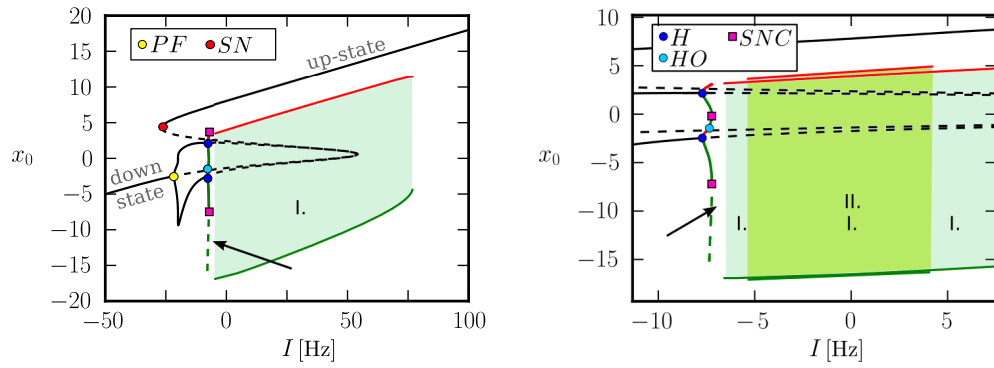


**Figure 3.6:** Bifurcation diagram of the  $N = 4$  site network, showing the  $x_0$  component of the solutions, as a function of the input strength  $I$ . **Left:** The fixpoint and limit-cycle solutions, as well as the bifurcations for the full interval range, also shown in Fig. 3.5. **Right:** A zoom-in to the parameter region with Hopf-bifurcations. The solid (dashed) black curves denote stable (unstable) fixpoints, solid (dashed) red/green lines correspond to the maximal/minimal amplitudes of stable (unstable) limit cycles. The filled color circles and squares indicate bifurcation points:  $PF$  - Pitchfork,  $SN$  - saddle-node,  $H$  - supercritical Hopf,  $HO$  - homoclinic, and  $SNC$  - saddle-node bifurcation of limit cycles. The two green shaded intervals denote the stability regions of the switching (I.) and of the traveling wave (II.) limit cycle solutions. The arrow points to a parameter window with chaotic dynamics (see Appendix C). The stable segments of the S-shaped symmetric solution curve, denoted as “up-state” and “down state”, correspond to fully active and fully inactive networks (cf. Fig. 3.5). The parameters are the same as for Fig. 3.4.

### 3.2.3 Complex activity patterns in random networks

To enable the investigation of the emergence of transient-state dynamics as we add STSP to the network, we also implement a simple binary parameter  $\nu \in \{0, 1\}$  in the target functions for the calcium and neurotransmitter levels (cf. Eq. (3.3)):

$$\begin{aligned} U(y) &= 1 + (U_{\max} - 1)y\nu \\ \Phi(y, u) &= 1 - \frac{uy}{U_{\max}}\nu, \end{aligned} \quad (3.12)$$

which allows for the switching off of STSP, with  $\nu = 0$ , even in the presence of presynaptic activity  $y_i > 0$ . In larger size random networks we demonstrate that the previously presented transient-state dynamics is not an artifact of the symmetrical network topology, but it is a generic behavior emerging when STSP is added to attractor network models.

The network structures discussed so far have been characterized by symmetric weight matrices,  $\omega_{ij} = \omega_{ji}$ , with  $\omega = w, z$ , both for excitatory and inhibitory synapses. To demonstrate that the presented results apply to non-symmetric

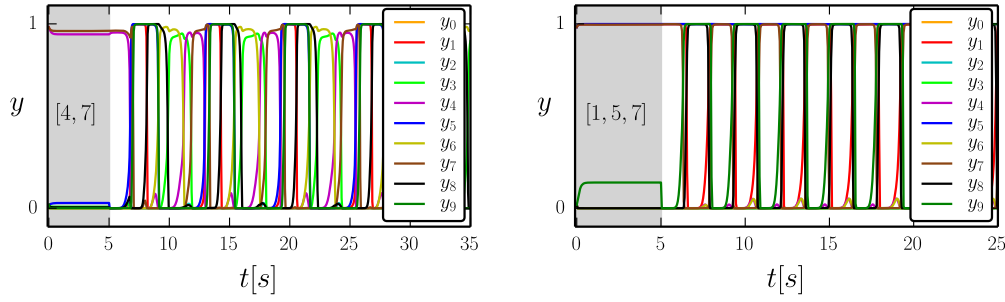


**Figure 3.7:** Time-series of firing rates  $y_i$  of the  $N = 10$  site random network, showing two coexisting limit-cycle solutions. STSP is turned off, by setting  $\nu = 0$  for the synaptic target functions (3.12), in the first 5 seconds, as indicated by the respective gray-shaded areas. **Left / right:** The initially activated cliques consist of neurons  $[4, 7]$  /  $[1, 5, 7]$ , respectively. The parameters are  $a = 0.4$ ,  $b = 0$ ,  $\Gamma = 10 \text{ s}^{-1}$ ,  $I = 0$ ,  $w = 80 \text{ Hz}$ ,  $z = -200 \text{ Hz}$ ,  $\sigma_w = \sigma_z = 10 \text{ Hz}$ , together with  $T_u = 21 \text{ ms}$ ,  $T_\varphi = 706 \text{ ms}$ , and  $U_{\max} = 4$ .

$\omega_{ij} \neq \omega_{ji}$  couplings as well, we add a static perturbation to the synaptic strengths:

$$\omega_{ij} = \omega_{ij}^0 + \eta_{ij}^\omega, \quad \omega_{ij}^0 = \begin{cases} \omega, & \text{if } i \text{ and } j \text{ are connected} \\ 0, & \text{otherwise} \end{cases} \quad (3.13)$$

where  $\omega = w, z$  denotes the average value of the excitatory, respectively of the inhibitory weights, while the  $\eta_{ij}^\omega$  static perturbations correspond to normally distributed random variables centered around zero with standard deviations  $\sigma_\omega$ . Hence, we keep with (3.13) the complementary structure of excitatory and inhibitory connections, while the exact synaptic efficacy of the synapses will, however, differ for every pair of neurons.

Finally, we now consider the  $N = 10$  and 100 site random networks depicted in Fig. 3.3, and solve the system (3.7) together with the new STSP target functions (3.12) and the perturbed synaptic weights (3.13). Furthermore, here we use experimentally determined STSP time-scale parameters, setting  $T_u = 21 \text{ ms}$  and  $T_\varphi = 706 \text{ ms}$ , according to the in-vitro measurements of inhibitory (GABAergic) interneurons in neocortical slices of rats somatosensory cortex [113].

Starting with the  $N = 10$  neuron network, in Fig. 3.7 we present two coexisting limit-cycle attractors. The generated transient-state sequences are indicated by plateaus of high-activity states (with  $y_i > 0.8$ ), corresponding to cliques of active neurons:

$$[4, 7] \rightarrow [1, 5, 7] \rightarrow [1, 5, 9] \rightarrow [5, 8, 9] \rightarrow [6, 8] \rightarrow [3, 6] \rightarrow [3, 4] \rightarrow ,$$

on the left, and

$$[1, 5, 7] \rightarrow [1, 5, 9] \rightarrow [5, 8, 9] \rightarrow [1, 5, 9] \rightarrow [1, 5, 7] \rightarrow ,$$

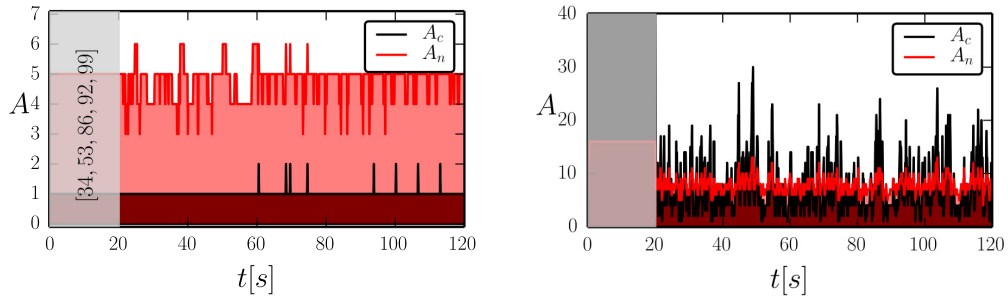


**Figure 3.8:** The activity of the  $N = 100$  site random network, showing the number of active neurons  $A_n$  with  $y_i > 0.8$  (red curve), respectively of the active cliques  $A_c$  (black curve). STSP is turned off,  $\nu = 0$  for the first 20 seconds, corresponding to the grey-shaded interval. **Left:** Strong inhibition,  $w/|z| = 1/5$ , allows for a single activated clique of 4-6 neurons at all times. For the here selected initial state  $A_n = 5$  and  $A_c = 1$ , where the active neurons are [34, 53, 86, 92, 99], cf. Fig. 3.3. **Right:** The excitatory-inhibitory balance  $w/|z| = 1$ , leads to a chaotic fluctuation of co-activated cliques, with  $A_n = 16$  and  $A_c = 41$  when STSP is turned off. Other parameters are  $I = 0$ ,  $a = 0.4$ ,  $b = 0$ ,  $\Gamma = 10 \text{ s}^{-1}$ ,  $w = 100 \text{ Hz}$ ,  $\sigma_w = \sigma_z = 10 \text{ Hz}$ ,  $T_u = 21 \text{ ms}$ ,  $T_\varphi = 706 \text{ ms}$ ,  $U_{max} = 4$ .

on the right, respectively. Despite the perturbed weight matrices (3.13), for switched-off STSP with  $\nu = 0$ , the attractors of the system remain to be the activated cliques of excitatory connections, as indicated by the gray-shaded time intervals in Fig. 3.7. The time-series of patterns, generated by transient-state dynamics with STSP, when  $\nu = 1$ , may be selected via the initially activated clique-states, i. e. on the initial conditions in the  $n = 3N$  dimensional phase space, separated into different attraction-domains of the respective limit cycles. Which particular cliques belong to such a limit cycle depends, however, on the specific synaptic weight configurations (3.13).

Limit cycles are not the only possible realizations of transient-state dynamics. In Appendix C we show an example of chaotic oscillations in the symmetric 4-site network. One may expect that chaotic behavior also appears when the network structure is perturbed, especially in the limit of large random networks. In Fig. 3.8 we see examples of chaotic-like sequential switching in terms of the number of activated cliques. As we emphasized in Sec. 3.2.1, when inhibition is significantly stronger than excitation, information items may be encoded by single active cliques of neurons (see the left plot of Fig. 3.8). The generated sequence of patterns corresponds then to the chaotic switching between the high number of possible states, cf. Eq. (3.5).

In case of a more balanced competition of excitatory vs. inhibitory inputs, the co-activation of several cliques is possible (see the gray-shaded interval in the right plot of Fig. 3.8 with  $A_c = 41$  active cliques), allowing for a highly unpredictable fluctuation, not only in terms of the active cliques, but also in the total number

of firing neurons. Whether this behavior is the result of a strange attractor, or of long-lasting transients still remains to be checked. That is only possible by running simulations encompassing longer and longer total time intervals. Furthermore, one may also employ tests for chaos [29] to rule out the existence of exceedingly long periodic windows, which may not be detectable in the time-series of activities. We have checked that the presented behavior persist even after 1000 seconds of total simulation time, a time scale which is larger than many cognitive processes. On the other hand, even transient chaos may easily turn into a permanent one when noise is added to a system [133, 134]. Therefore, looking for the strange attractor in a 300-dimensional system may not be relevant when chaotic behavior persists for a long time, even without external noise.

### 3.3 Discussion

In this chapter we have presented a simple neural network model for generating transient-state dynamics. Following the idea of adding local slow variables to attractor networks [9], we have argued that short-term synaptic plasticity (STSP) provides natural candidates for these auxiliary variables [51]. Considering networks of different sizes we have demonstrated that STSP may transform stable fixpoints of multistable systems into attractor ruins, leading to the emergence of transient-state dynamics, characterized by a sequential switching between well-defined states of the system.

We have shown that the observed transient-state dynamics is stable in the sense that it corresponds to limit cycle and chaotic oscillations. The phase space of the system is contracting, the presence of small noise would, hence, only affect the duration and the order of appearance of these metastable states. The presented model is also not sensitive to small variations of parameters, nor to the particular wiring of the networks. We examined the effect of a constant global input to the topology of the phase space, and we have shown that only strong input can push the system close to bifurcation points, and that this global input may be used to suppress the state switching behavior, and force it back to the original attractor states of the network.

The proposed mechanism for generating transient-state dynamics does not rely on the construction of heteroclinic channels, which are not stable structurally and only occur, hence, for systems of a special form [3]. Therefore, we believe that the here presented principle may be more relevant for modeling biological neural networks, which are generally characterized by several different time scales. Finally, the example of the investigated symmetric network suggests that these two, seemingly very different approaches (slow variables vs. heteroclinic channels) might lead to systems with similar features, especially in the limit when special symmetries are present in the system. New concepts and methods need to be developed by investigating further slow-fast dynamical systems to gain a deeper

understanding of the underlying dynamical mechanisms [42, 53]

For demonstrating that STSP may play an important role in the generating spatio-temporal patterns involved in many cognitive processing phenomena, we considered clique encoding neural networks, where excitatory and inhibitory connections form complementary structures. This topology allows for an exceedingly high number of possible states, corresponding to active cliques of excitatory connections, being biologically also plausible. There are experimental evidences for transiently active assemblies of strongly connected excitatory neurons, called cell assemblies, which underlie several cognitive operations in the brain via creating specific hierarchical organizations, regarded as the neural syntax. Furthermore, their dynamically changing (due to STSP for example) constellations of synaptic weights, denoted as “synapsembles” are thought to be involved in the modulation and linking of the constituents of the neural syntax (for review of cell assemblies and synapsembles see [135]). As specific applications of sequential pattern generation via short-term synaptic plasticity, we discuss here two model systems, there are, however, a big deal of other possible phenomena where STSP may be involved [136].

The role of short-term synaptic plasticity has been investigated in the context working-memory (WM) models as well [137]. In working-memory tasks, information has to be stored for several seconds for further processing purposes [138]. It has been shown, that STSP is able to explain the irregular persistent activity measured in the prefrontal cortex during WM tasks [124, 136, 139]. Using STSP, the question of the capacity of working-memory, in terms of stored memory items has also been addressed [140]. Nevertheless, other neurocomputational models of working memory also exist [141].

Centrally generated rhythms can serve many functions in biological systems, including movement generation for locomotion, breathing and swallowing. Central patterns generators (CPG) are small biological neural networks that produce rhythmic patterns are a result of simple signals, without requiring continuous sensory information [142]. The here presented small neural networks may, hence, also be interpreted in terms of central pattern generators, since they are stable even in the absence of external input, and the duration of states is comparable to the length of movement segments needed for locomotion [129]. In **Chapter 4** we provide a proof of this concept, by implementing simple neural controllers, modulated by short-term plasticity, to generate motions primitives for simulated robots.



# Chapter 4

## Robots as complex dynamical systems

Sándor, B., Jahn, T., Martin, L., & Gros, C. (2015). *The Sensorimotor Loop as a Dynamical System: How Regular Motion Primitives May Emerge from Self-Organized Limit Cycles*. *Frontiers in Robotics and AI*, 2, 31.

Martin, L., Sándor, B., & Gros, C. (2016). *Closed-loop robots driven by short-term synaptic plasticity: Emergent explorative vs. limit-cycle locomotion*. *Frontiers in Neurorobotics*, 10, 12.

A field strongly related to computational neuroscience and to brain research, in general, is artificial intelligence. The areas like cognitive artificial systems and autonomous robots aim to synthesize the results and methods of neuroscience, cognitive sciences and complex systems to develop new paradigms for creating autonomously operating artificial systems and robots. In this spirit, we extend here the application areas and concepts of dynamical systems theory to the study of robotic locomotion, also linking together the results of the previous chapters.

We start by introducing the field of locomotion robophysics [11], and contrasting it to traditional approaches of robotics. Investigating the behavior of simple cylindrical and spherical shaped rolling robots within the LPZRobots simulation environment [12] we show that even a minimal control mechanism can lead to generation of complex motion patterns. The “nervous system” of the robots consist of a single, respectively three proprioceptual neurons, measuring the actual positions of the actuators. The activity of the neurons is further modulated by internal, and respectively short-term synaptic plasticity mechanisms, similarly to the neural networks presented in **Chapter 3**. The resulting behavior primitives correspond to limit-cycle and chaotic attractors in the overarching phase space of internal and external variables. We find that the interactions with other robots or obstacles may lead to a switching between coexisting attractors, a striking consequence of the multistability discussed in **Chapter 2**.

## 4.1 Introduction to locomotion robophysics

General robotic locomotion is considered to be a particularly difficult task, since it aims to endow robots with the ability to navigate and transport themselves autonomously from place to place in complex environments. For this, robots need to interact with the external world via their own body and incorporate the feedback in a closed-loop control scheme [11].

Traditional approaches to locomotion robotics focus on defining specific tasks, and then optimizing the performance of robots for successful and fast task completion. This can be achieved either via classical control theory [143], using open-loop control, e. g. with central pattern generators [142], or by considering closed-loop schemes with feedback [144]. Withing this scheme, machine learning techniques, like deep learning algorithms [145, 146], have been successful in controlling devices to locomote on relatively complex terrains [147, 148]. These approaches are lacking, however, the understanding of the dynamics of the robot when interacting with the surrounding environment. Hence, one can not expect the robots to always perform well, when being exposed to locomote autonomously in a diversity of environments, without understanding the dynamical system consisting of the controller, body and environment [11].

Locomotion robophysics aims to provide a general framework for the systematic study of simplified robotic architectures in controlled environments, to formulate and test new theoretical models for autonomous locomotion [11]. Its goal is, hence, not necessarily the optimization of procedures for successful task completion, but rather the understanding of the principles governing the interactions with the environment. The broad exploration of parameter space for simplified devices with a minimal geometric and control design can also lead to a deeper understanding of the mechanisms needed for optimal performance. Furthermore, the experimental investigation of the principles of locomotion in a diversity of possible environments, e. g. the self-propulsion in highly dissipative media [149], can help in testing and refining the theoretical predictions.

There is a growing agreement in the field of robotics that ideas originated from biology and physics in general, or more specifically from fields at their intersection, complex systems and self-organization, can strongly benefit the design and construction of autonomous robots. In this context, it has been argued that the behavior of an agent is not simply the outcome of an internal, top-down-type control, but rather the result of self-organization and emergence in complex dynamical systems [19]. The behavior of robots should be seen as the dynamical and reciprocal coupling of brain, body and environment.

*Embodiment:* the possible motions of agents are shaped, constrained and also defined by their very own body and the way that interacts with the environment [13].

This information may be used then to distribute the control and processing not only among the parts of its “brain”, but also to its musculoskeletal system. The embodied perspective provides an alternative approach for tackling the challenges raised by the wide variety of complex environments. This idea is employed in the field of soft computing and morphological computation, which rely on the contribution of the body to cognition and control of artificial and natural agents [150]. In this view, robots should exploit the material properties of their body, reducing with that the need for computation (e. g. using elastic materials might be beneficial above stiff materials, since the latter one requires more complex control to avoid more risky collisions) [151], a phenomena also referred to as compliance.

Several complementary principles have been proposed for designing control mechanisms which allow or even generate embodiment. On one side one may rely on self-organized behavior generation [80] guided by information theoretical objective functions [152], such as predictive information [89], surprise minimization [88], or homeokinesis [12]. In these cases, higher order principles may be postulated in terms of generating functionals [86], which are then used to derive learning and adaptation rules for the artificial neural networks controlling the robot. On the other side, embodied agents may also be created via evolutionary robotics, where optimized neural controllers are selected via evolutionary processes [153].

As a bottom-up approach, similarly to the case of dynamical modeling of neural networks discussed in Sec. 3.1, complex dynamics may also be generated via employing phenomenological models of biological neural processes. In the framework of bio-inspired robotics [19], short-term synaptic plasticity (STSP) has been proposed to be used for sculpting rhythmic motor patterns [128]. In **Chapter 3** we have introduced the main bio-physical processes contributing to the transient modification of synaptic efficacy, arguing also that STSP proves to be involved in several motor control related processes, such as the selection of motor patterns and their modulation [129]. Short-term plasticity mechanisms similar to STSP have already been investigated in the context of robotic locomotion as well, indicating that even very simple neural networks may allow for a build-up of stable gaits [130].

Along these lines, we further reduce the complexity of the neural controllers, considering first a single neuron with internal adaption [14], which is then followed by a three-neuron network, modulated by short-term synaptic plasticity rules [15]. Implementing these controllers in simple rolling robots, we investigate the resulting dynamical behaviors in terms of the emerging attractors in the full space of the “brain”, body and environment.

The earliest dynamical systems type of approaches to robotic locomotion have already a twenty years long history. Among those one has to mention the pioneering work of Randall Beer as first step towards developing a consistent dynamical systems theory as a general theoretical framework for the synthesis and analysis

of agent-environment interactions [82]. This view has been since pushed forward by several people. Nonlinear dynamical systems have been considered for goal-directed movement generation, by learning trajectories [154] via computing with fixpoints [155] and with continuous attractors [41]. Alternatively, one may design dynamical systems which allow for self-exploration, viz. a self-organized behavior for autonomous robot development [156].

It has been shown that efficient locomotion can also be achieved by embedding the control and learning mechanisms in a single dynamical system, rather than keeping the traditional separation between controller and learning algorithm [157]. Considering, hence, the full sensorimotor loop as an overarching dynamical system [158] the embodiment and situatedness of agents, may be studied in terms of the emerging stable attractors in the phase space of the internal neural circuitry, body and environment [159]. While these works are pointing in the right direction consider only relatively complex controllers (see [160, 161] for some more recent examples), we believe, hence, that the investigation of even more simplified robots, behaving in some minimal environment, may unveil further aspects and features of the underlying dynamical principles.

In the next sections we follow this idea for pushing forward the dynamical systems view in locomotion robophysics. We propose that embodiment may be defined in terms of the topological differences between the attractors generated only by the controller, viz. when being detached from the body, and the self-organized attractors in the overarching phase space of the full sensorimotor loop. We present a novel interpretation of the robot-environment interactions in terms of switching between attractors and attractor ruins. Hence, we believe that our dynamical systems approach to robophysics can provide an intellectual complement to the engineering and computer science type approaches of traditional robotics.

To investigate the dynamics generated by the here considered simple neural controllers, we use the LPZRobots simulator software package [12]. The library comes with a realistic physics simulator in which the user defines the environment, the obstacles, the agents and so on. The physical simulation steps are performed iteratively using the Open Dynamics Engine kernel [162], while the graphical visualization is created by the Open Scene Graph [163]. The physics simulation is based on the rigid body dynamics of objects, which may be connected by different joints, constraining the relative motion of the connected objects. All objects follow the principles of Newtonian mechanics with gravitation, different types of inertial forces, static and kinetic friction, drag, and so on. At collisions the interactions are modeled as a superposition of elasticity, friction and slipping. The equations of motion are integrated iteratively using a semi-implicit (first order) Euler method.

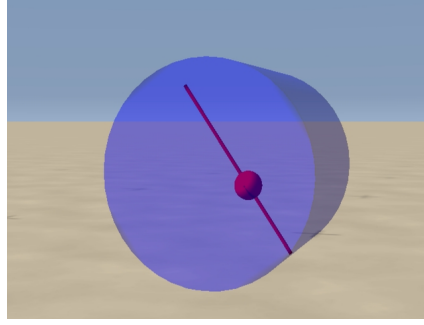


**Figure 4.1:** Snapshot of the barrel robot placed on a flat ground in the LPZRobots physics simulation environment [12]. The red ball is moved along the rod by an actuator, which in turn is controlled by a single neuron (see Fig. 4.2). The movement of the ball leads to a rolling dynamics, as a result of the gravitational and inertial forces.

## 4.2 The sensorimotor loop as a dynamical system

In the previous section we argued for the need of detailed studies of minimal robots and simple environments. Here, considering a cylinder-shaped barrel robot, controlled by a single proprioceptive neuron, we investigate the full sensorimotor loop as an overarching dynamical system composed of the “brain”, body and environment [14]. For designing the controller, we use a simple theoretical neuron model, presented in **Chapter 3**, while for the interpretation of results we rely on the concepts introduced in **Chapter 1**.

The perfect cylinder-shaped architecture, as shown in Fig. 4.1, allows for a rather constrained dynamics. When placing the robot on a flat horizontal surface the dynamics is mainly confined to a straight rolling in the initially specified direction. Since the environment and the full dynamics is invariant under translations, i. e. we would get the same dynamics in every point of the physical space, the two-dimensional physical plane can be reduced to a single axis. We note that the robot is also able to jump in the vertical-direction, we minimize, however, this effect as much as possible by suitably chosen parameters.

### 4.2.1 One-neuron controller with internal adaption

The locomotion of the robot is generated indirectly, by moving an internal weight on a rod fixed along the diameter of the cylinder-shaped body. The “brain” of the robot, controlling this dynamics, consists of a single rate-encoding neuron characterized by a sigmoidal transfer function  $y(x)$  (see Sec. 3.1.2):

$$y(x, b) = \frac{1}{1 + e^{a(b-x)}}, \quad \dot{b} = \varepsilon a(2y - 1), \quad (4.1)$$

with a slowly adapting threshold  $b(t)$ , on a time scale defined by the adaption rate  $\varepsilon$ . The gain  $a$  is fixed. To simplify the system, we first consider the case of instantana-

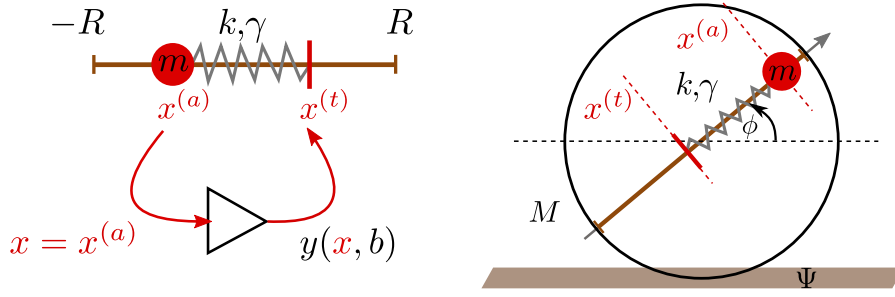


**Figure 4.2:** Sketch of the barrel robot (cf. Fig. 4.1) together with the one-neuron controller. **Left:** The controller of the robot with the damped spring actuator. The “brain” of the robot, a proprioceptual neuron (triangle) with internal adaption dynamics (4.1), receives as input the actual position  $x^{(a)} \in [-R, R]$  of the ball (red filled circle). The output firing rate  $y(x, b)$  of the instantaneous neuron with membrane potential  $x = x^{(a)}$  determines the target position  $x^{(t)}$  for the weight of mass  $m$ , defined by Eq. (4.2). The actuator then moves the ball along the rod (brown axis), with the force determined by a PID controller (4.3), simulating the dynamics of a damped spring (4.4), with constant  $k$  and damping  $\gamma$ . **Right:** The rolling robot, composed of a barrel of radius  $R$  and mass  $M$  (black circle), with the one-rod controller forming an angle  $\phi$  with the horizontal (dashed line). The locomotion is dissipative due to the rolling friction, which is proportional to the velocity of the barrel  $v_b = R\omega = R\dot{\phi}$  (without slipping) via friction constant  $\Psi$ .

neous neurons, which may be seen as the limit of an infinitely fast neural dynamics in Eq. (3.2), where the membrane potential  $x$  is following instantaneously the incoming inputs, i. e.  $\dot{x} \rightarrow 0$ . The internal adaption  $\dot{b}$  in Eq. (4.1) is regulating the firing rate  $y$  of the neuron, by increasing (decreasing) the threshold  $b$  for high (low) activities (cf. Fig. 3.2). Thus, for any constant input  $x(t) = x$ , the threshold dynamics  $\dot{b}$  would lead to a stable equilibrium by  $b \rightarrow x$  and  $y \rightarrow 1/2$ . We note that the process of internal adaption (4.1) may also be motivated by information theoretical considerations, optimizing the distribution of the output firing rates [77, 81].

For controlling the dynamics of the robot, the neuron receives a single sensory input reflecting the state of its own body, namely the actual position  $x^{(a)}$  of the ball along the rod (see Fig. 4.2). Transferring this input through the activation function  $y(x)$  of the neuron, the a new target position generated for the ball is defined as:

$$x^{(t)} = 2R \left( y(x, b) - \frac{1}{2} \right), \quad (4.2)$$

where  $x = x^{(a)}$ , due to the instantaneous internal dynamics of the membrane potential, and  $R$  denotes the radius of the barrel. Note that  $x^{(t)} = \pm R$  for  $y = 1/0$ , respectively.

The actuator moving the ball of mass  $m$  is implemented as a PID controller, provided by the LPZRobots simulation environment [12]. The estimated force

$F = m\ddot{x}^{(a)}$  needed for shifting the ball from its actual position  $x^{(a)}$  to the new target position  $x^{(t)}$  is, hence, given by the sum of three terms (proportional, integral and derivative terms):

$$F = g_P(x^{(t)} - x^{(a)}) + g_I \int_0^t (x^{(t)} - x^{(a)})dt + g_D \frac{d(x^{(t)} - x^{(a)})}{dt}, \quad (4.3)$$

with the respective  $g_P$ ,  $g_I$  and  $g_D$  weighting coefficients. By setting  $g_I = 0$  in our simulations, the system consisting of the moving ball controlled by Eq. (4.3), reduces to a (driven) damped spring-block equation (cf. Fig. 4.2):

$$m\ddot{x}^{(a)} = -k(x^{(a)} - x^{(t)}) - \gamma \frac{d(x^{(a)} - x^{(t)})}{dt} + F_{\text{in}}, \quad (4.4)$$

with  $k = g_P$  and  $\gamma = g_D$ . The  $F_{\text{in}}$  term denotes the forces resulting from the interaction with the environment. When considering the moving robot, the gravitational pull and the inertial forces are included in  $F_{\text{in}}$ . On the other hand, for  $F_{\text{in}} = 0$ , the system (4.4) describes the dynamics of the ball of mass  $m$  in isolation from the body and the physical environment.

Due to the velocity dependent friction with  $\gamma > 0$  the damped-spring system (4.4) is dissipative. The energy supply is provided by the internal adaption (4.1), which may hence be considered the “engine” of the robot. With a fixed threshold  $b(t) = b$ , the ball is always pushed to one of ends of the rod,  $x^{(a)} \rightarrow x^{(t)} = \pm R$ , since  $y(x = R) \approx 1$  and  $y(x = -R) \approx 0$ . The adaption (4.1) generates, however, an internal stress, always trying to keep the activity around  $y = 1/2$ . Hence, by adjusting the target position  $x^{(t)}$  continuously, it provides the energy dissipated by the physical motions.

By fixing the body of the robot, we investigate first the system composed of the one-neuron controller (4.1) and the actuator (4.4). Since the robot can not roll, the angle between the rod and the horizontal direction is constant  $\phi = \phi_0$ . The combined dynamical system is hence three-dimensional:

$$\begin{aligned} \dot{x} &= v \\ \dot{v} &= -\Omega^2(x - x^{(t)}) - \beta(v - \dot{x}^{(t)}) - g \sin(\phi_0) \\ \dot{b} &= 2\varepsilon a(y - 1/2) \end{aligned} \quad (4.5)$$

where  $\Omega^2 = k/m$ ,  $\beta = \gamma/m$  and  $x = x^{(a)}$ , while the time derivative of the target position depends on the internal adaption:

$$\dot{x}^{(t)} = 2Ra y(1 - y)(v - \dot{b}). \quad (4.6)$$

The term  $-g \sin(\phi_0)$ , corresponding to the tangential component of the gravitational acceleration  $g$ , can be transformed away by a simple coordinate shift:

$$x \rightarrow x - g/\Omega^2 \sin \phi_o, \quad b \rightarrow b - g/\Omega^2 \sin \phi_o, \quad (4.7)$$

resulting in a topologically equivalent system. It is easy to see that, in the absence of the gravitational term, the system has a trivial fixpoint at  $(x^*, v^*, b^*) = (0, 0, 0)$ . The corresponding stability region of the fixpoint can be determined (cf. Sec. 1.1.3) by computing numerically the eigenvalues of the Jacobian of system (4.5). We find that, for a critically damped spring with  $\beta = 2\Omega$ , and together with the  $\Omega^2 = 200$ ,  $R = 1$  and  $p = 1$  parameters, the fixpoint is stable for  $a \lesssim 1.78$  when  $\varepsilon = 1$ , termed as the off mode of the barrel. This state is destabilized at the supercritical Hopf bifurcation curve indicated in the  $(\varepsilon, a)$  phase diagram of Fig. 4.3. Hence, for larger gain  $a$  the system exhibits stable limit-cycle oscillations (similarly to a self-coupled neuron with intrinsic adaption [76, 164]), referred to as the on mode of the engine.

## 4.2.2 Embodiment as self-organized motion

In Sec. 4.1 we argued that, in complex environments, embodied agents may be more effective than robots, for which the feedback of the environment is not incorporated in the movement generation procedure. Here, we demonstrate that the feedback resulting from the body-environment interaction is essential for the dynamics of our (one-neuron controlled) barrel robot, since there would be no motion if the sensorimotor loop was interrupted.

We consider now robots with radius  $R = 1$  and mass  $M = 1$  in the LPZRobots physics simulator, keeping the parameters of the controller and actuator the same as for Eq. (4.5). We place the robots in a simple environment, consisting of a flat ground surface, as shown in Fig. 4.1. Due to the static friction the barrel is rolling without slippage, with a translational velocity  $v_b = R\omega$ , determined by the angular velocity  $\omega = \dot{\phi}$ , compare Fig. 4.2. The rolling drag  $\propto \Psi v_b$  is characterized by the rolling friction coefficient  $\Psi = 0.3$ . The gravitational acceleration is set to  $g = 9.81$ . In the simulations a step size of 0.001 is used which generates robust results for the selected parameter sets. For the sake of simplicity, we present here the parameters and variables in dimensionless units, with SI units being implied. A complete list of parameter values, together with the corresponding units is however given in Appendix D.

We have seen that the controller-actuator system (4.5) is characterized by two stable states corresponding to the on and off modes of the engine. Considering now the barrel robot without restricting its motion, one may expect, hence, no rolling behavior in the off mode of the engine, since the  $(x^*, v^*, b^*) = (0, 0, 0)$  state is also a stable fixpoint of the full system. The numerical simulations performed in the LPZRobots environment yield, however, surprising results. While, the off mode corresponds indeed to a non-rolling stable fixpoint of the barrel robot, we find that rolling behavior may additionally be achieved for a wide parameter domain. Furthermore, partially coexisting rolling modes, together with the on mode oscillations of the engine have also been found. In Fig. 4.3 we indicate the experimentally

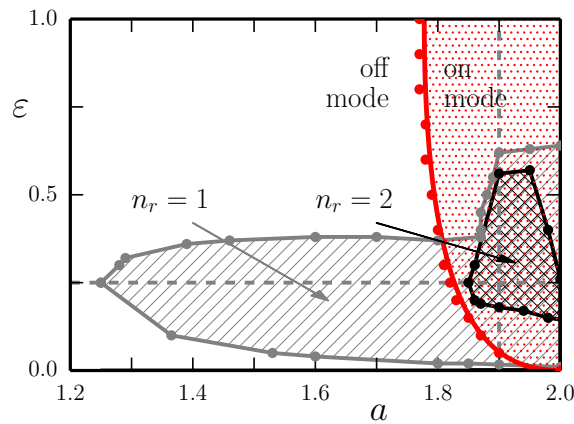


**Figure 4.3:** Phase diagram of the barrel robot, as a function of the gain  $a$  and adaption rate  $\varepsilon$ . The red, gray and black dots enclosing the dotted, single- and cross-hatched regions respectively, are obtained via the LPZRobots simulation package. The red solid line separating the on and off modes, follows from the stability analysis of one-neuron controlled actuator system (4.5), for a fixed but otherwise arbitrary angle  $\phi = \phi_0$ . The dashed vertical and horizontal lines indicate the respective cuts at  $\varepsilon = 0.25$  and  $a = 1.9$  used for the bifurcation diagrams shown in Fig. 4.5. *Non-rolling mode:* The red dots indicate the Hopf-bifurcation curve, where a stable limit cycle is generated, denoted here as on mode, corresponding to the oscillation of the ball along the vertically settled rod, without a rolling motion of barrel. Outside the red dotted region, the system (4.5) has a single stable fixpoint, hence the “engine”, see Eq. (4.1), may only operate in a self-organized manner when the barrel is already moving.

*Rolling modes:* The hatched regions enclosed by the solid gray / black lines mark the parameter domain allowing for  $n_r = 1 / n_r = 2$  self-organized limit cycles respectively, where the barrel is rolling with a finite average velocity  $\langle v_b \rangle$ . For the dynamics of the rolling modes see Fig. 4.4. In this dynamical systems approach, the rolling behavior found in the off mode of the engine may be seen as a signature of embodiment. The stationary and the drifting back-and-forth modes (see Fig. 4.6) are not shown to avoid overcrowding. The parameters  $\Omega^2 = k/m = 200$ ,  $\beta = \gamma/m = 2\Omega$ , for the actuator,  $R = 1$ ,  $M = m = 1$  for the barrel, and  $g = 9.81$ ,  $\Psi = 0.3$  for the environment have been kept constant.

found stability regions and the number of rolling modes in the  $(\varepsilon, a)$  phase diagram. Furthermore, examples of corresponding time series and phase-plane plots are shown in Fig. 4.4.

The on mode of the engine coincides with the 0:1 mode of the barrel robot, where no rolling is resulting from the oscillation of the ball (cf. left column of Fig. 4.4) along the vertically settled rod. This is possible due to the velocity dependent rolling friction force of the barrel,  $v_b = R\dot{\phi}$ . As discussed in the previous section, the gravitational term, in this case with  $\phi_0 = \pi/2$ , does not effect the

stability region of the limit cycle, hence the numerically computed Hopf curve and the measurement points from the simulation overlap (see the red dots and red line in Fig. 4.3). The vertical position of the rod is, however, reflected by the non-symmetric  $x(t)$  oscillations in Fig. 4.4. The limit cycle corresponding to the 0:1 mode is embedded in the higher dimensional phase space of the full dynamical system. It only spans, nevertheless, the  $(x, v, b)$  subspace corresponding to the controller-actuator system (4.5), since in the absence of rolling the other variables are not changing in time,  $\dot{\omega} = 0$  and  $\dot{\phi} = 0$ . In this sense the 0:1 mode of the barrel robot and on mode of the engine are indeed equivalent.

The embodiment of the robots [11] is demonstrated by the emergence of self-organized rolling modes solely as a result of the environmental context [14]. The rolling behavior is realized via limit cycles, generated in the overarching phase space of the controller, body and environment, as indicated by their projections to the  $(v_b, x)$  plane shown in Fig. 4.4. The found rolling modes may be characterized by the relative frequency of the rolling and the oscillation of the ball, the 1:1 and 1:3 modes denoting, hence, one, respectively three oscillations along the rod per one rolling of the barrel. These limit cycles are, furthermore, degenerate in the physical space, due to the previously discussed translational symmetry. Therefore, the locomotion modes of the barrel robot may be seen as a self-sustained motion on degenerate attractors.

Thanks to these self-organized modes the robot is able to function for a wide range of parameter settings. Rolling modes may coexist with the on mode of the engine, see Fig. 4.3), the presence of stable oscillations in the actuator-controller system (4.5 is, however, not a requirement for the locomotion of the barrel robot. Rolling dynamics can also be achieved in the off mode, where the engine kicks in via the closed sensorimotor loop if the rolling motion has been started from outside. External momentum is then transferred to the damped spring system via the inertial forces  $F_{in}$  in Eq. (4.4). In case of the 1:1 mode, this external kick may be seen, from a dynamical systems point of view, as pushing the phase point to the basin of attraction of the corresponding limit cycle. This result also illustrates that the engine is not overpowering the behavior of robot.

Another example of situatedness [165] is provided by the parameter domain with  $n_r = 2$  rolling modes, which are found additionally to the 0:1 mode. The coexistence of several stable modes can be interpreted in terms of behavioral primitives, allowing for different motion patterns for the same control parameters (see the three coexisting limit cycles in Fig. 4.4), indicating the sign of multifunctionality [166]. Therefore, the robot may easily switch to another motion primitive, changing qualitatively its behavior, when interacting with the environment.

In Fig. 4.5 we present two bifurcation diagrams corresponding to different parameter cuts of the phase diagram shown in Fig. 4.3, indicating the average rolling

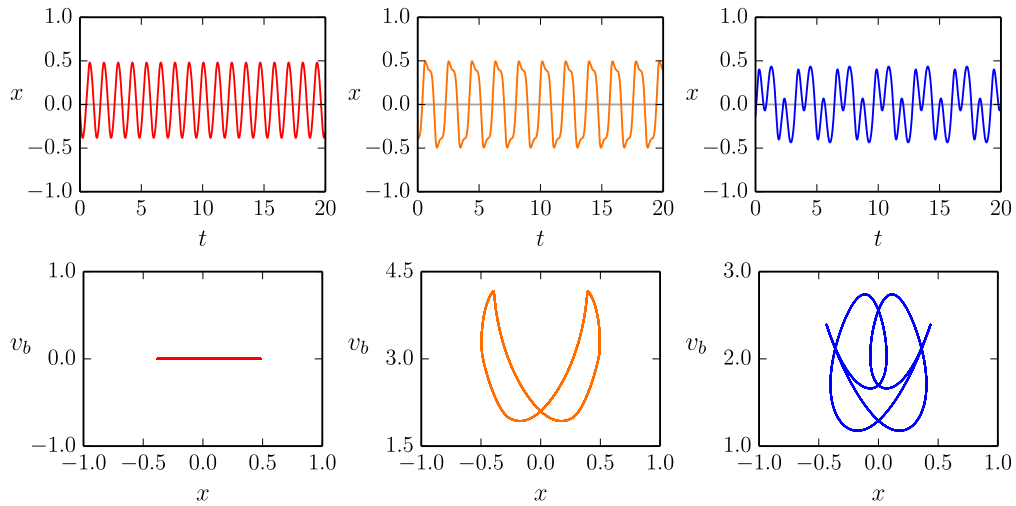


**Figure 4.4:** *The rolling and non-rolling modes of the barrel robot shown in Fig. 4.1. **Top row:** The time series  $x(t) = x^{(a)}(t)$  of the actual position of the ball along the rod. The gray line at  $x = 0$  is just a guide to eye. **Bottom row:** The corresponding  $(x(t), v_b(t))$  phase-plane projections of the trajectories, compare Fig. 4.2. The velocity of the barrel is  $v_b(t) = 0$  for the non-rolling 0:1 mode (left column) and  $v_b(t) > 0$  for the rolling 1:1 and 1:3 modes (middle and right columns), respectively. The adaption rate and the gain are  $\varepsilon = 0.25$  and  $a = 1.9$ , respectively, as indicated by the intersection point of the dashed gray lines in the phase diagram shown in Fig. 4.3. The other parameters are kept unchanged.*

speed  $\langle v_b \rangle$  as a function of the selected control parameters, the adaption rate  $\varepsilon$  and the gain  $a$ , respectively. The stability domains,  $\varepsilon \in [0.018, 0, 55]$  for the 1:1 and  $\varepsilon \in [0.19, 0, 55]$  for the 1:3 modes, are terminated (presumably) by saddle-node bifurcations of limit cycles (similarly to the one presented in the bottom plot of Fig. 2.4). Comparing the two plots of Fig. 4.5, the low-velocity rolling mode (green dots) is continued either by the 1:1 mode (as in the left panel) or by the 1:3 mode (right panel). This might look contradicting, nevertheless, it is possible since the saddle-node curves are oblique in the  $(\varepsilon, a)$  plane, while the considered cuts being perpendicular to each other (see Fig. 4.3).

Thanks to the avoided pitchfork bifurcation [1], the locomotion speed can be increased continuously,  $\langle v_b \rangle \propto \sqrt{\varepsilon}$ , when shifting slowly the adaption rate from the low-velocity region to the 1:1 mode, while keeping the gain constant, at  $a = 1.9$ . In the very small adaption rate domain,  $\varepsilon < 0.018$ , we find, however, another cascade of limit-cycle bifurcations, where small variations of the control parameter may lead a qualitative change of the behavior. For adaption rate  $\varepsilon = 0.017$ , a back-and-forth rolling motion has been unveiled, where the barrel is swinging around the initial coordinate. Due to the relatively small stability domain of this mode, a finite but otherwise very small change of the adaption rate  $\varepsilon$  may induce a switch in the rolling direction. Noisy internal parameters would lead, hence, to an explorative

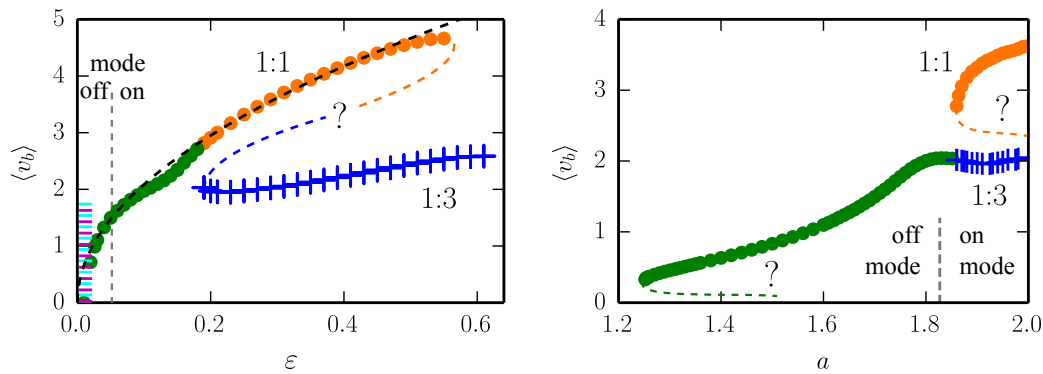


**Figure 4.5:** Bifurcation diagrams of the self-organized rolling modes. The average rolling speed  $\langle v_b \rangle$  for the 1:1 and 1:3 modes (measured along the parameter cuts shown by the dashed lines in Fig. 4.3) indicated by the green/orange dots and the blue crosses, respectively. The orange/blue/green curves labeled by question marks are added by hand to denote the presumably existing unstable limit cycles, which annihilate the rolling modes at their stability boundaries. The border between the on and off modes, corresponding to the Hopf bifurcation point in system (4.5) is denoted by the vertical dashed lines. **Left:** The bifurcation diagram as a function of the adaption rate  $\varepsilon$  for  $a = 1.9$ . The color hatching indicates the region of small adaption rates and low-velocity rolling, together with the additional back-and-forth mode, as discussed in Fig. 4.6. The dashed black curve is a fit to the average speed,  $\langle v_b \rangle \propto \sqrt{\varepsilon}$ . **Right:** Bifurcations as a function of the gain  $a$  for  $\varepsilon = 0.25$ . The parameters are as for Fig. 4.3.

behavior, since the direction selection depends only on the timing of otherwise (directionally) neutral perturbations (see Fig. 4.6).

The here presented rolling modes correspond to self-organized limit cycles in the phase space of the brain, body and environment. Considering barrel robots with two perpendicular actuators, each of them controlled independently by separate neurons, we have found several other rolling modes as well (see Ref. [14] for more details). These modes may be seen as generalized versions of the 1:3 mode, with many oscillations of the weights during one revolution of the barrel. Therefore, we assume that barrel robots allow for limit-cycle attractors of arbitrary complexity.

The one-dimensional locomotion of the considered barrel robots is, however, not convenient for the study of interactions with complex environments. In the following section, we consider robots with spherical body, which allows for two-dimensional meandering dynamics on a flat plane. Placing then several robots and obstacles in one arena, we focus on the dynamical description of their interactions in terms of the previously introduced attractor picture of motion primitives.

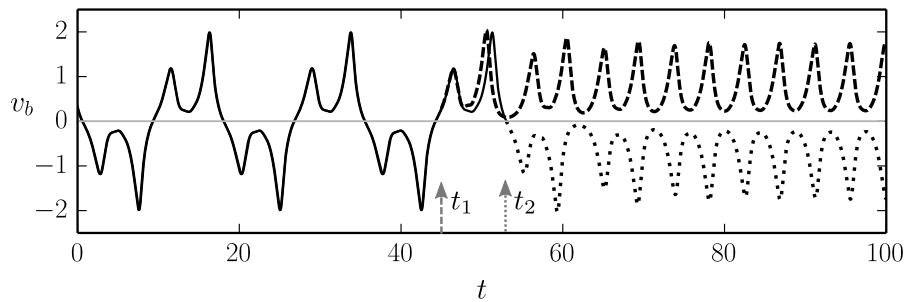


**Figure 4.6:** *Direction-selection in the locomotion of the barrel robot. The time series of the rolling speed  $v_b$  is shown, for  $a = 0.19$ , in the low-velocity parameter region. The two superimposed runs use identical initial conditions, started in the back-and-forth mode, found for  $\varepsilon = 0.017$  (see the color hatching in Fig. 4.5). In the first 40 time units, the barrel exhibits a symmetrical swinging behavior, with a vanishing average speed  $\langle v_b \rangle = 0$ . The two scenarios of direction selection are triggered by the discontinuous change of the adaption rate to  $\varepsilon = 0.02$  (corresponding to the 1:1 rolling mode) in different phases of the swinging motion. In the first run,  $\varepsilon$  is changed at time  $t_1 = 45$ , resulting in a rolling to the right, with  $\langle v_b \rangle > 0$  (dashed line). In the second run, rolling in the opposite direction, with  $\langle v_b \rangle < 0$ , is induced at time  $t_2 = 53$  (dotted line). The other parameters are as for Fig. 4.3. For the corresponding animation see the supplementary material of Ref. [14].*

### 4.3 Degenerate attractors and symmetry breaking

In this section we increase the complexity of the investigated robots in several ways. First of all, by considering spherical robots, the dynamics is not constrained anymore to one-dimensional rolling, thus, more complex behavioral patterns can be generated. Furthermore, to keep the internal symmetry of the system, we construct three perpendicular actuators, each of them controlled by a single proprio-sensory neuron. Finally, based on the results of **Chapter 3**, we connect the neurons by dynamical synapses, characterized by short-term synaptic plasticity (STSP) [114]. The resulting robot serves, hence, as a proof of concept to show that STSP may be used to generate self-organized motor patterns [15].

We now briefly discuss the architecture of the robot. Note, however, that as it is a generalized version of the barrel robot, we mainly focus on the presentation of the neural controller. In that, we rely on the content of the previous chapters and sections. In particular, we refer to the introductory sections describing the dynamics of neural networks and short-term plasticity mechanisms, see Sec. 3.1.3 We only repeat, hence, the necessary formula and terminology for a better readability.

#### 4.3.1 Sensorimotor loop with short-term synaptic plasticity

The simulated spherical robot is illustrated in Fig. 4.7. The rolling motion is generated in a similar manner to the case of the barrel robot (cf. Sec. 4.2.1). Three

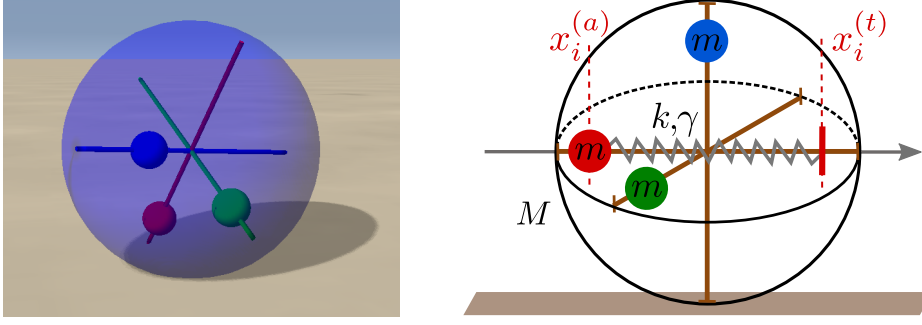


**Figure 4.7:** Spherical robot with three actuators. **Left:** A snapshot of the robot in the LPZRobots simulation environment [12], placed on a flat ground surface. **Right:** A sketch of the spherical robot of body mass  $M$ . The three weights of individual masses  $m$  (red, green and blue) move along perpendicular rods without interference. The vertical dashed lines indicate the actual position  $x_i^{(a)}$  of the  $i$ -th (here red) weight along the the axis attached to the rod (gray arrow). The damped spring actuator, with spring constant  $k$  and damping  $\gamma$ , then pulls the ball towards the target position  $x_i^{(t)}$ , determined by the the output of a controlling neuron (cf. Fig. 4.8).

independent weights are moved along perpendicular rods without interference (they do not collide in the center of the sphere). As a result of the gravitational and inertial forces acting on the weights, the sphere starts to turn, leading finally to a rolling dynamics.

The actuators moving the balls of mass  $m$  along the respective rods are implemented via the built-in PID controllers (see Sec. 4.2.1) in the LPZRobots library [12]. When setting the integral term to zero, the dynamics reduces to a damped spring-block system, compare Eqs. (4.3) and (4.4), with damping  $\gamma$  and spring constant  $k$ . The actual  $x_i^{(a)}$  and target positions  $x_i^{(t)}$  of the  $i$ -th weight are measured with respect to the local coordinate axis attached to the respective rods (see the right panel of Fig. 4.7).

Analogously to the controller of the barrel robot, compare Eq. (4.2), the target position of the  $i$ -th weight,

$$x_i^{(t)} = 2pR \left( y(x_i) - \frac{1}{2} \right), \quad x_i^{(t)} \in [-pR, pR]. \quad (4.8)$$

is determined by the output  $y(x_i)$  of a single rate encoding neuron, (see Fig. 4.8) characterized by the sigmoidal transfer function,

$$y(x_i) = \frac{1}{1 + e^{a(b-x_i)}}, \quad (4.9)$$

with gain  $a$  and threshold  $b$ . The  $p \in [0, 1]$  scaling factor is used to limit the effective sliding range of the ball within the radius  $R$  of the sphere.

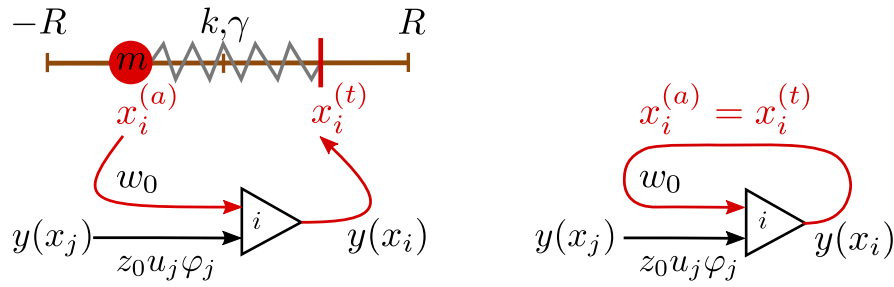


**Figure 4.8:** The controller of the three-axis spherical robot, illustrated in Fig. 4.7. **Left:** Sketch of the sensorimotor loop, showing only one of the three,  $i = 1, 2, 3$ , neuron-controlled actuator modules. Each actuator, consisting of a weight of mass  $m$  and a damped spring, with spring constant  $k$  and damping  $\gamma$ , is controlled by a single neuron. Neuron  $i$  receives the actual position  $x_i^{(a)} \in [-R, R]$  of the  $i$ -th weight as excitatory input,  $w_0(x_i^{(a)} + pR)/(2pR)$ , with  $p \in [0, 1]$ . The inhibitory input  $-z_0 u_j \varphi_j y(x_j)$  coming from the other two neurons,  $j \neq i$ , is modulated by short-term synaptic plasticity, via Eq. (4.11). The target position  $x_i^{(t)}$  for mass  $i$ , defined by (4.8), is then determined by the activity of the corresponding neuron  $y(x_i)$ . **Right:** The network of the controller neurons, with  $i = 1, 2, 3$  (showing only one module), when the feedback of the environment is short-cut via  $x_i^{(a)} = x_i^{(t)}$ . The neurons are coupled to each other via inhibitory synapses with STSP, each of them having additionally an excitatory self-coupling, compare Eq. (4.12).

In order to investigate the hypothesis that short-term synaptic plasticity can be used for motor pattern generation, we consider neurons  $i = 1, 2, 3$ , modeled as rate-encoding leaky integrators, characterized by an internal variable  $x_i$ , associated with the membrane potential. The actual position of the  $i$ -th weight is measured now indirectly (in contrast to the instantaneous neurons used for the barrel robot), the corresponding neuron receiving it in form of an excitatory input,  $(x_i^{(a)} + pR)/2pR \in [0, 1]$ , scaled by the respective synaptic weight  $w_0 > 0$ . A closed-loop control, with neurons only receiving excitatory input, would, however, push the weights to the positive end of the rod,  $x_i^{(a)} \rightarrow pR$ . Since STSP may be effectively used to destabilize fixpoint attractors as added to the inhibitory couplings of complementary subnetworks (see **Chapter 3**), we couple the three neuron by inhibitory dynamical synapses. The dynamics of the neural activity is driven, hence, by the sum of excitatory and inhibitory inputs:

$$\dot{x}_i = -\Gamma x_i + \frac{w_0}{2pR} (x_i^{(a)} + pR) - z_0 \sum_{j \neq i} u_j \varphi_j y(x_j), \quad (4.10)$$

where  $\Gamma$  is the leak rate and  $z_0 > 0$  denotes the static inhibitory synaptic weights (note the minus sign in front of  $z_0$ ), respectively. The inhibitory weights are modulated via short-term synaptic plasticity, denoting with  $u_j$  and  $\varphi_j$  the calcium and neurotransmitter concentration in the corresponding presynaptic terminal (cf. Fig. 3.1). The dynamics of STSP is described by the full-depletion model intro-

duced in Sec. 3.1.3:

$$\begin{aligned} \dot{u}_i &= \frac{U(y_i) - u_i}{T_u}, & U(y_i) &= 1 + (U_{\max} - 1)y_i \\ \dot{\varphi}_i &= \frac{\Phi(u_i, y_i) - \varphi_i}{T_\varphi}, & \Phi(u_i, y_i) &= 1 - \frac{u_i y_i}{U_{\max}} \end{aligned} \quad (4.11)$$

characterized by the respective time scales  $T_u$  and  $T_\varphi$ . The maximum concentration is set by the parameter  $U_{\max}$  (see Fig. 3.2). We note that by choosing a  $U_{\max} = 1$  parameter, the calcium concentration converges to  $u_j = 1$ , reducing hence the number effective variables. Looking at Eq. 4.10 we see that, while the excitatory term is pushing the weight to the end of the rod, the inhibition coming from the other two neurons has an opposite effect. However, as we have seen in the previous chapter, high presynaptic activity,  $y(x_j) = 1$ , results in the depletion of neurotransmitters,  $u_j(t)\varphi_j(t) \rightarrow 0$ , leading typically to transient-state dynamics.

We intend to focus on the employment of the dynamical systems view in the study of robotic locomotion. Therefore, similarly to the previous section, we mostly omit the usage of physical units, SI units being implied: seconds / meters for time / lengths respectively, while the masses are given in units of kilograms. We choose, however, biologically and physically realistic parameters for the full-depletion model and for the physical dimensions of the robots, respectively. Therefore, when presenting time-series plots, we also provide the time units in the axis labels for an easier interpretation of the results. We consider robots with radius  $R = 0.25$ , body mass  $M = 1$ , and weights of masses of  $m = 1$ . For the time scales of the calcium and neurotransmitter dynamics,  $T_u = 0.3$  and  $T_\varphi = 0.6$  is used, respectively. The leak rate is  $\Gamma = 20$ . For the neurons a gain  $a = 0.4$  and threshold  $b = 0$  is set. The gravitational acceleration and the rolling friction coefficient are the same as for the barrel robot,  $g = 9.81$  and  $\Psi = 0.3$ , respectively. The simulations have been performed in the LPZRobots environment using a time step of 0.001 units. For an exhaustive list of all the parameter values with the corresponding units see the Appendix D.

First, we examine the robot with the reduced full-depletion model, by setting  $U_{\max} = 1$  in Eq. (4.11). In this way the calcium concentration remains unaffected by the presynaptic activity, reducing STSP to the depletion of neurotransmitters.

To illustrate the dynamics of the controller-actuator system in the absence of the environmental feedback, we assume that the weights may be moved instantaneously to their target positions, as specified by Eq. (4.8). Note that this not only means that there are no interaction forces, but in this case the whole PID controller is cut out via short-circuiting the actual and target position signals,  $x_i^{(a)} = x_i^{(t)}$ . Therefore, the system reduces to a recurrent network of three neurons, the actuators being replaced by an excitatory self-coupling, as shown in Fig. 4.8. The corresponding excitatory

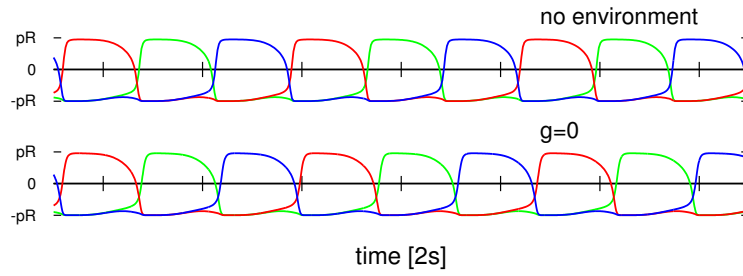


**Figure 4.9:** The dynamics of the controller sketched in Fig. 4.7, showing the time series of the target positions  $x_i^{(t)}$  of the three balls (red, green, blue). **Top:** The network controller isolated from the actuator and from the rest of the robot body, by short cutting the feedback of the environment via setting  $x_i^{(a)} = x_i^{(t)}$ , defined by Eq. (4.12). **Bottom:** The spherical robot suspended in air without gravity,  $g = 0$ . The time series are very similar, but the period of the oscillations is a bit longer in the latter case. The parameters are  $U_{max} = 1$  for the full-depletion model (4.11) and  $(w_0, z_0) = (190, 600)$  for the synaptic weights, which correspond to the C1 mode shown in Fig. 4.11 and 4.12.

term in Eq. (4.10) is hence replaced by the firing rate of the considered neuron:

$$\dot{x}_i = -\Gamma x_i + w_0 y(x_i) - z_0 \sum_{j \neq i} u_j \varphi_j y(x_j), \quad (4.12)$$

since  $(x_i^{(t)} + pR)/2pR = y(x_i)$ . The corresponding network dynamics is shown in the top plot of Fig. 4.9, where the activity of the three neurons is transformed into time series of target positions  $x_i^{(t)}$  via Eq. (4.8). In the resulting transient state dynamics (cf. Sec. 3.2), the neurons are activated sequentially, leading to a periodic switching of target positions.

One obtains an almost identical behavior when suspending the sphere robot in the air in the absence of gravity, viz. with  $g = 0$ . Due to the damped-spring actuator, the actual position may only follow the target position with a certain (quite small) time-delay. Nevertheless, the limit-cycle attractor generates very similar oscillations in the projection of target positions  $x_i^{(t)}$ , though it is embedded in a significantly higher order phase space. The delayed dynamics is only observable by the slightly prolonged oscillation period in the bottom plot of Fig. 4.9.

Note that the presented limit cycles are the only attractors of the isolated 3-neuron network and respectively of the sphere robot system. Placing now the robot in simple environments, the closed-loop control scheme leads to the self-organized generation of a whole zoo of motion patterns. In the next section we investigate the found motion primitives in terms of the attractors formed in the overarching phase space of the robot-environment system. Furthermore, we give a dynamical systems type of interpretation of the dynamics of interactions.

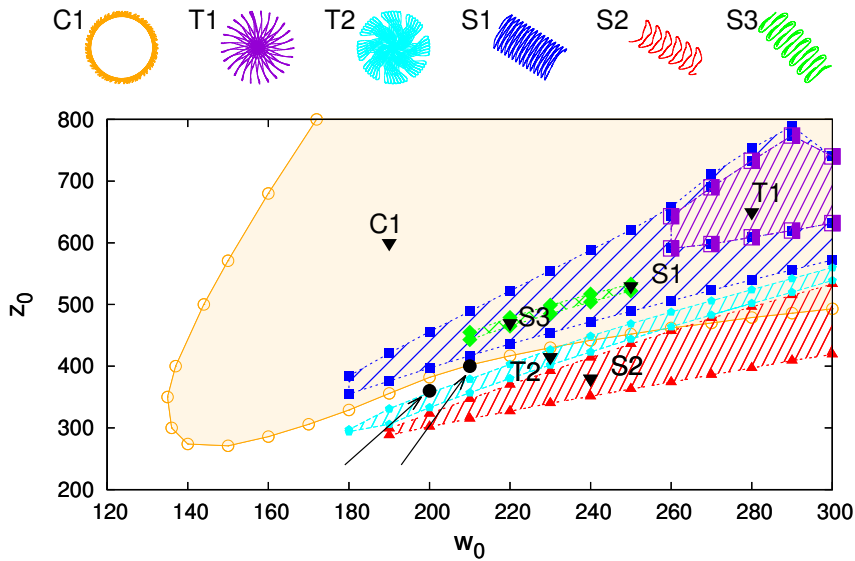


**Figure 4.10:** Phase diagram of the sphere robot in the parameter plane of excitatory and inhibitory synaptic weights,  $(w_0, z_0)$ , for  $U_{\max} = 1$ . The shaded areas denote the stability domains of the six limit cycles corresponding to the regular motion patterns shown on the top, as illustrated by the trajectory traces in the plane of locomotion, viz. in the plane of the environment (compare Fig. 4.11). The trajectories are color coded, using the same conventions as the one used for the stability domains, while the respective  $(w_0, z_0)$  parameter pairs are indicated via the labeled black triangles. The arrows pointing to the black dots indicate two examples of parameter sets,  $(200, 360)$  and  $(210, 400)$ , for which the robot exhibits chaotic motion.

### 4.3.2 Motion patterns as degenerate attractors

In Sec. 4.2.2 we have seen that the dynamics of barrel robots, though different patterns are possible, may be reduced to a one-dimensional locomotion. The spherical shape of the here considered robots allows, however, for locomotion in all directions, leading to more complex behavior patterns as well. To investigate the possible motion primitives, we consider two controller setups with  $U_{\max} = 1$  and  $U_{\max} = 4$ , respectively. Note that in the first case only synaptic depression is allowed, without calcium dynamics in the full-depletion model (4.11).

The phase diagram of regular motions patterns in the plane of the bare synaptic weight parameters  $(w_0, z_0)$ , is divided into several overlapping stability regions, as shown in Fig. 4.10 for  $U_{\max} = 1$ . An example of the corresponding locomotion trajectories is illustrated in Fig. 4.11. The spherical body shape tends to produce meandering motion patterns (for animations of the behavior see the supplementary material of Ref. [15]). In the C1 mode the trajectory is almost circular. The T1 and T2 modes, with torus attractors in the phase space, generate star-like trajectories, where the robot is rolling back-and-forth while also turning one direction. Contrary to the previous three motion patterns, in the S1, S2 and S3 modes we see

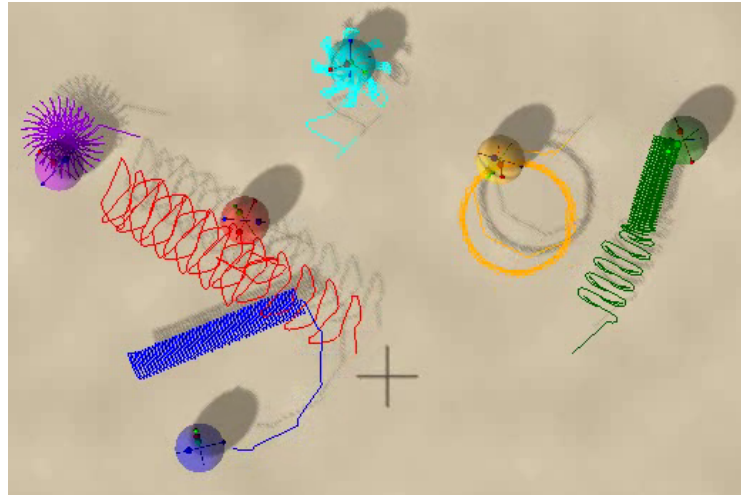


**Figure 4.11:** A snapshot of the simulation with six copies of the sphere robot placed on a flat plane in the LPZRobots environment. The robots have identical parameter settings, except for the  $(w_0, z_0)$  parameters, which have been set corresponding to the regular rolling modes, indicated by labeled black triangles in the phase diagram presented in Fig. 4.10: T1 (magenta) - (280, 650), T2 (cyan) - (230, 415), C1 (orange) - (190, 600), S1 (blue) - (250, 530), S2 (red) - (240, 380), S3 (green) - (220, 470). The color lines are showing the traces of the trajectories in the plane of locomotion. The green and blue robots switch to coexisting attractors as a result of collisions with the yellow and respectively the red spheres. The latter one, in the absence of multistability, changes only the direction of locomotion, when colliding for example with the magenta robot. For the corresponding video see the supplementary material of Ref. [15].

a meandering snake-like motion in a certain direction.

The differences of the rolling patterns are also reflected by the motion of the weights along the perpendicular rods, see Fig. 4.12. For C1, T2 and S2 all the three weights are oscillating, either phase-shifted with respect to each other, or in a pair-wise (partially) synchronized manner. However, in the T1, S1 and S3 modes one of the balls is never crossing the center of the sphere. The period of the oscillations, while being close to the natural period of the controller (cf. Fig. 4.9), may also differ significantly from each other. Note that the actual positions  $x_i^{(a)}$  of the balls may overshoot the interval of target positions,  $x_i^{(t)} \in [-pR, pR]$ , due to the inertial forces and the gravitational pull acting on them. Choosing  $p = 1/2$  for scaling factor keeps, however, the motion inside the sphere.

Since both the isolated controller network and the weightlessness robot possess only one limit-cycle attractor, the complex set of patterns found in simple plane environments (with gravity) provides another proof of embodiment. Comparing the time series corresponding to the six different rolling modes to the time series

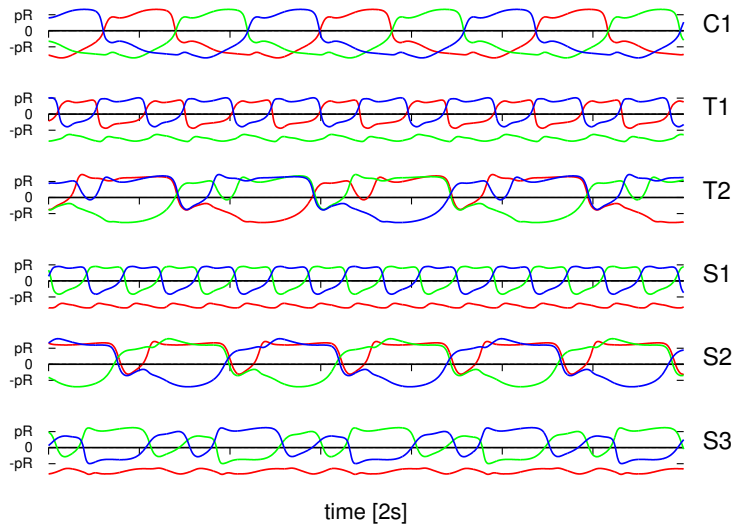


**Figure 4.12:** Time series of the actual positions  $x_i^{(a)}$  of the three weights (red, green, blue), compare Fig. 4.7. The selected regular motions patterns are labeled in the right side of the plots, using identical parameter settings as in Fig. 4.11. The small tick marks on the time axis indicate intervals of 2 seconds.

of the isolated network, we see that the C1 mode is topologically equivalent to the one presented in Fig. 4.9. Therefore, the C1 mode may be seen as the driver of the dynamics, also having the largest region of stability among the observed self-organized patterns, cf. Fig. 4.10.

The stability domains presented in Fig. 4.10 terminate presumably by saddle-node bifurcations of limit cycles [1]. When multiple attractors coexist, chaotic behavior is often generated in the form of an overarching attractor, combining the destabilized separate limit-cycle trajectories [7]. Such phenomena may be observed at the boundary of the stability regions of the C1, S1, T2, and S2 modes, where chaotic behavior has been found (cf. Fig. 4.10). Since long transients may occur close to a chaotic phase, the systematic study of their exact extent may be difficult. The examples of chaotic dynamics discussed here are stable both in the long term limit and in the presence of external noise as well (see Appendix D.3). The chaotic mode generates a random-walk-like meandering dynamics in open spaces, as shown in Fig. 4.13, which may be considered as a basic explorative behavior [167].

Note that the dynamics of the robots moving on a horizontal plane is invariant under translations and rotations about the vertical axis. In other words, the space is homogeneous and isotropic with respect to locomotion. This invariance allows for the formation of regular and chaotic attractors corresponding to different locomotion modes. These attractors, while being bounded in the phase space of the internal variables (cf. the phase plane plots of the barrel robot in Fig. 4.4), form overlapping continua in the physical (external) space. It is this continuum that

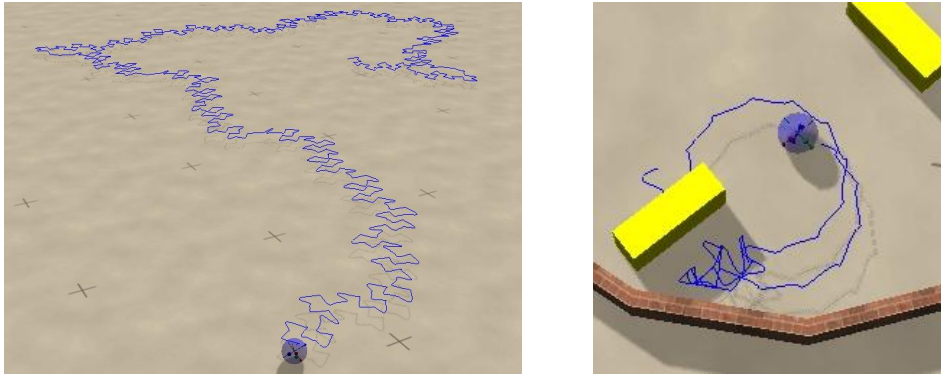


**Figure 4.13:** *Chaotic meandering of the sphere robot in open space and in structured environments. Snapshots of the trajectory traces are shown in the chaotic mode, for  $U_{max} = 1$  and  $(w_0, z_0) = (210, 400)$ . **Left:** The trajectory in open place, indicating chaotic explorative behavior. Small segments of the trace resemble that of the S2 mode, which is however unstable here (see Fig. 4.11). **Right:** The dynamics in a closed environment with movable objects (yellow blocks). The circular-like trajectory, corresponding to an unstable C1 limit cycle, is induced by the collisions with the obstacles. For a video of the behavior see the suppl. material of Ref. [15].*

permits the description of motion patterns in terms of degenerate attractors (see Sec. 1.1.4). The initial conditions - defined in the subspace of internal variables - determine, hence, which of the possibly more coexisting degenerate attractors will be approached in the asymptotic limit.

In the next section we investigate what happens if we place the robot in a structured environment, where translational and rotational symmetries may only be locally available. A manifest example for such an environment can be realized by placing static boundaries on the previously used infinite plane. The system is then characterized by only local symmetries, which are broken as soon as the robot collides with something.

### 4.3.3 Interactions as autonomous mode switching

Among the simplest interactions robots may have with their surroundings are collisions, produced when locomoting agents bump into obstacles. Collisions are generally thought to be undesirable events during robotic locomotion, cause it might potentially damage both the robot itself or the environment. There is a great deal of effort put in the research of obstacle avoidance via using adaptive neural controllers [168], much less known is, however, about the dynamics of collisions in terms of the attractors, which are driving the motions. Here, we investigate the interactions both with passive and with active elements of the environment, viz. movable obstacles and other spherical robots, respectively.

Keeping the horizontal plane, we place fixed walls in form of a large polygonal-

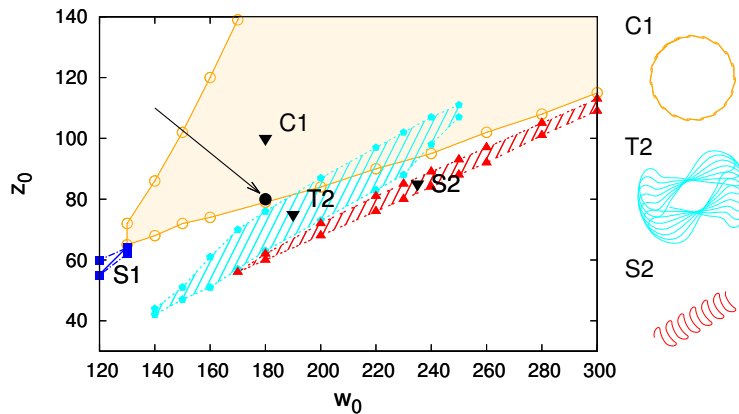


**Figure 4.14:** Phase diagram of the sphere robot in the parameter plane  $(w_0, z_0)$  obtained when using  $U_{max} = 4$  in the full-depletion model (4.11). The naming and color coding of the locomotion modes corresponds to the ones in Fig. 4.10. Traces of trajectories in the plane of locomotion are provided on the right of the figure for the C1, T2 and S2 modes, corresponding to the parameters indicated by the labeled black triangles. An example of chaotic state, coexisting with the C1 mode, is marked by the black dot at the tip of the arrow, for  $(w_0, z_0) = (180, 80)$ . The other parameters are kept unchanged, see Appendix D.

shaped arena, around the robot. Furthermore, movable obstacles, with masses similar to the robot's own total mass, are scattered around, as in the right picture of Fig. 4.13. We let the robot wander around using the parameter settings of the chaotic mode (shown on the left). In this structured environment one observes that the robot is roaming among the obstacles, exploring different regions of the available space. In the right picture of Fig. 4.13 we show a snapshot of this explorative behavior, illustrating the trajectory corresponding to a time interval when the robot stays close for a while to the yellow block. The trajectory traces out the C1 circular mode, which is however not stable for the used parameter settings (cf. Fig. 4.10). This is possible since the selected chaotic mode exists close to the borders of the C1 stability domain. Unstable C1-type limit cycles are hence expected to exist embedded in the chaotic attractor (for an example, compare the chaotic and regular orbits of the prototype system shown in Fig. 2.7 in **Chapter 2**). The walls and objects of the arena break the translational symmetry of the plane, so the trajectory cannot settle on attractors in the overarching phase space of the system. The active exploration of the environment, with the robot bumping into obstacles, gives however access to otherwise unstable limit cycle options. The resulting dynamics may also be interpreted (by an external observer not knowing the system) as explorative playful behavior in a playground [12].

Symmetry breaking may also be caused by other active agents roaming around on the otherwise empty ground plane. In Fig. 4.11 we illustrate the interactions of six copies of the presented spherical robots, with parameter settings corresponding to the six representative examples of regular locomotion patterns shown in Fig. 4.10.

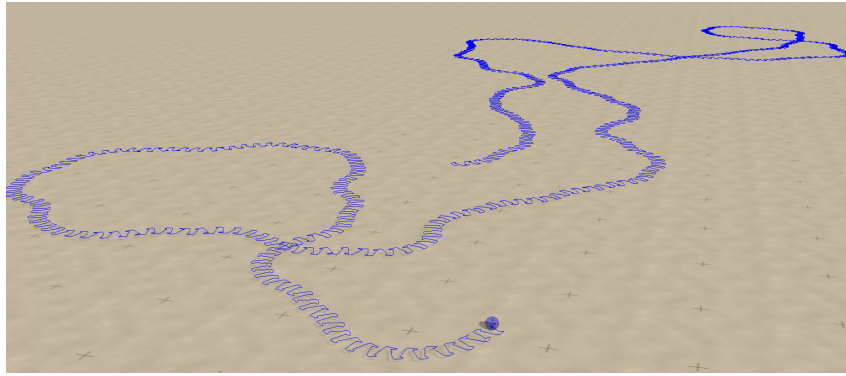


**Figure 4.15:** *Smooth chaotic wandering on a horizontal ground plane. The snapshot with the blue trajectory of the sphere robot is made for the  $U_{max} = 4$  and  $(w_0, z_0) = (180, 80)$  parameters, indicated by the arrow in Fig. 4.14. The dynamics is substantially smoother than the chaotic exploration observed for the  $U_{max} = 1$  case (compare Fig. 4.13).*

Since several stable attractors coexist for the selected  $(w_0, z_0)$  parameters, interactions with other robots lead to autonomous switching between these locomotion modes. The green robot, started in S2 mode, switches to S1 as a result of colliding with the yellow agent. Similarly, the blue robot ends up circulating in C1 mode after the collision with the red sphere. The latter one, being a global stable attractor, changes only the direction of locomotion whenever it bumps into other robots (here magenta and blue).

#### 4.3.4 Smooth chaotic meandering

The rolling modes presented so far have been obtained with an inactive calcium dynamics, by setting  $U_{max} = 1$  in the full-depletion model (4.11). With  $U_{max} = 4$  one may also enable the interaction of facilitation and depression mechanisms in the STSP rules. The corresponding phase diagram shown in Fig. 4.14 reveals a set of similar locomotion modes to ones discussed previously (cf. Fig. 4.10), with the main difference being the reduced range of inhibitory weights  $z_0$ . The chaotic mode found for  $(w_0, z_0) = (180, 80)$  allows for a biologically more realistic, smooth exploration of the space, changing the average direction of propagation relatively slowly, compared to the distance traveled in a quasi-straight line, see Fig. 4.15. This may be surprising in many respects, knowing that chaotic behavior is characterized generally by unpredictability (see Sec. 1.1.3).

This type of dynamics we have investigated in the framework of another project [29], not discussed in the present thesis. We have shown that a partially predictable type of chaos (PPC) does indeed exist, and may generally be found between period-doubling bifurcations and strongly chaotic parameter regimes. We proposed, furthermore, a simple 0-1 test for an efficient identification of PPC. By measuring the cross-correlation between initially close-by trajectories, we have

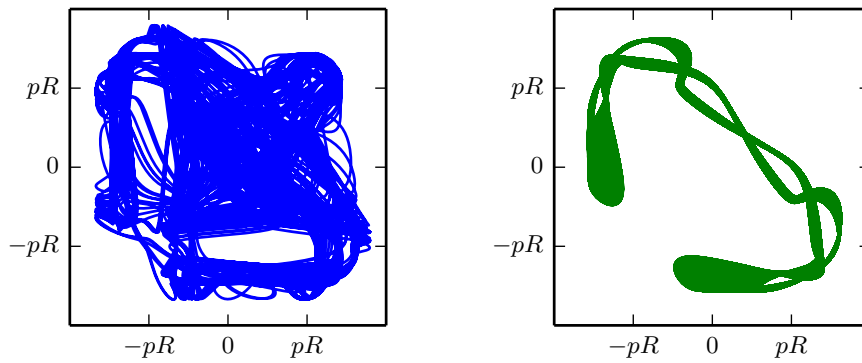


**Figure 4.16:** Comparison of the two chaotic meandering modes. Shown are the corresponding strongly chaotic (**left**) and partially predictable chaotic attractors (**right**), projected to the phase plane of actual positions  $(x_2^{(a)}, x_3^{(a)})$ , using  $(w_0, z_0) = (210, 400)$  with  $U_{max} = 1$  on the left, and  $(w_0, z_0) = (180, 80)$  with  $U_{max} = 4$  on the right. Note that due to the symmetry breaking dynamics of the weights, compare Fig. 4.17, there are actually three, symmetry related PPC attractors (only one is shown here).

shown that PPC is characterized by correlations persisting for exceedingly long times. The name, partially predictable chaos reflects hence the fact that the dynamics remains predictable - up to a certain level of precision - for time scales significantly longer, than the prediction time determined by the inverse Lyapunov exponent [23]. This is possible due to the special topology of the PPC attractors, which may be imagined as braid-like broadened limit-cycles. Trajectories started from small initial distances are exponentially diverging from each other in a perpendicular direction to the braids, the final decorrelation occurs, however, in a diffusive manner along flow [29].

Chaotic attractors generating PPC can be recognized hence by the formation braid-like structures in the phase space of the dynamical system. In Fig. 4.16 we compare the attractors of the chaotic locomotion modes found for  $U_{max} = 1$  and  $U_{max} = 4$ , respectively. Though we may only be able to visualize a low dimensional projection of the degenerate chaotic attractors embedded into a high dimensional phase space, the topological differences can be easily identified. The PPC attractor shown in the right plot of Fig. 4.16 indeed resembles a limit cycle with a braid-like structure, in contrast to the strong chaos one on the left, which allows for a qualitatively stronger mixing of the trajectories.

Both chaotic meandering modes are qualitatively similar to the S2 snake-like locomotion, which is accompanied by an irregular turning behavior in the plane of propagation. Note however that the S2 limit-cycle attractor has two types of degeneracies. The continuous degeneracy, as discussed previously, allows it to propagate in any direction. There is additionally a spontaneous symmetry breaking in the S2 mode, corresponding to a discrete degeneracy, since one of the weights is

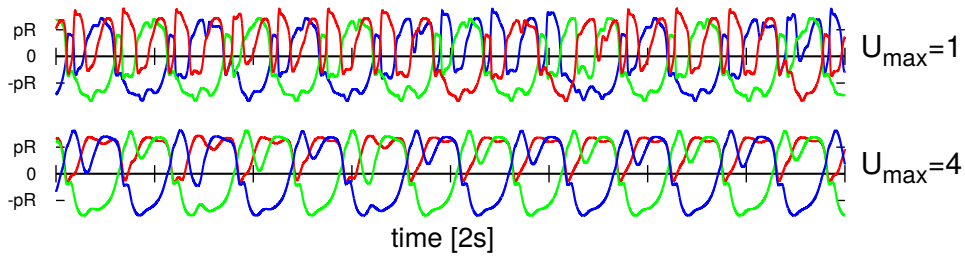


**Figure 4.17:** Time-series corresponding to the chaotic attractors presented in Fig. 4.16. Shown are the actual positions  $x_i^{(a)}$  of the three weights (red, green, blue) as a function of time (in units of 2 seconds). **Top:** Strong chaos for  $U_{max} = 1$  and  $(w_0, z_0) = (210, 400)$  shown in Fig. 4.13. **Bottom:** Partially predictable chaos for the  $U_{max} = 4$  and  $(w_0, z_0) = (180, 80)$  shown in Fig. 4.15. Both modes are locally similar to the time-series of the S2 mode, compare Fig. 4.12). Note that phase slips only occur for strong chaos.

always kept in the lower half of the rod, while the other two weights are oscillating phase-shifted (see Fig. 4.12). This discrete degeneracy is present also in the PPC mode for  $U_{max} = 4$ , as indicated by the corresponding time-series of Fig. 4.17. The smooth chaotic meandering is hence a consequence of a slow diffusion of the angle of propagation, which corresponds to the phase diffusion along the braids of the attractor. We observe, on the other hand, a discrete mode switching in the strongly chaotic mode for  $U_{max} = 1$ , tracing out occasionally one of the S2-like unstable limit cycles embedded in the chaotic attractor.

Though partially predictable chaos generates regular looking time series, see Fig. 4.17, the smooth diffusion of the propagation angle allows for the effective exploration of unknown, complex environments. Due to the only locally available symmetries, collisions induce further mode switching. In Fig. 4.18 we show two stages of such an explorative behavior in a simple maze, consisting of a rectangular arena and internal walls. Since the chaotic mode for  $U_{max} = 4$  coexists with the C1 circular shaped locomotion pattern, the robot switches intermittently between the two qualitatively different rolling modes. After long time, practically every single point of the arena may be visited.

## 4.4 Discussion

In this chapter we have investigated the dynamics of simple rolling robots in the LPZRobots simulations environment [12]. In order to allow for a detailed dynamical systems analysis of the locomotion patterns we considered cylindrical and spherical shaped robots, controlled by one, respectively three proprioceptual neurons, which may only measure the actual state of the body. The rolling motion is generated indirectly via moving internal weights along rods fixed to the barrel- or sphere-shaped robot-bodies. The neurons, characterized either by an adapting

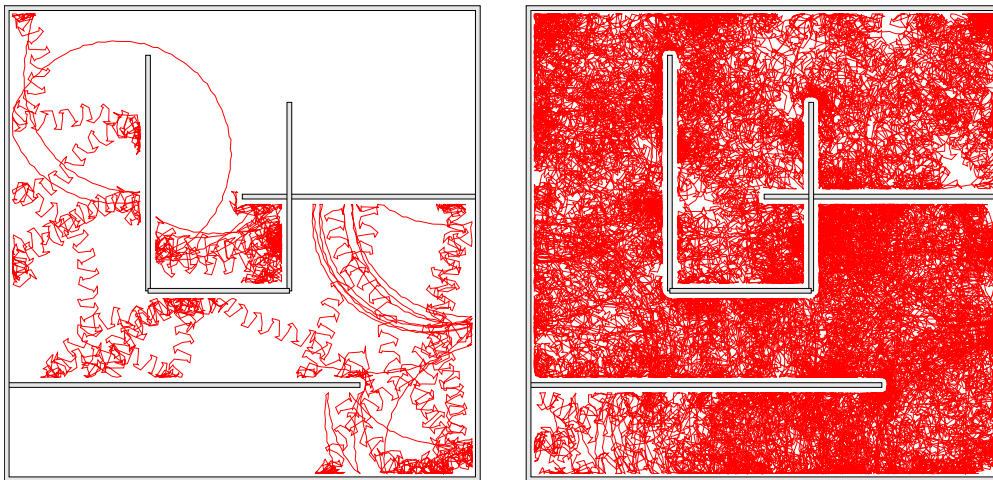


**Figure 4.18:** Chaotic exploration in a maze. The trajectory of the robot is indicated by the thin red curves in the partially predictable chaotic mode, for the  $U_{max} = 4$  and  $(w_0, z_0) = (180, 80)$  parameters. **Left:** An initial phase of the exploration showing the first 83 minutes of the simulation. **Right:** The visited locations after 1000 minutes. The robot may get stuck temporarily in corners, but due to the chaotic behavior it can always escape. After collisions it may switch to the CI mode, as that is a coexisting stable limit cycle. The corresponding radius of circulation is, however, so large (in this case) that the trajectory cannot retrace in itself.

threshold mechanism [164] or by dynamic inhibitory synapses [51], receive the actual positions of the weights and generate putative target positions for the next time step. The weights are then moved to the respective target positions via PD controllers, modeled as damped-spring systems.

In the absence of overpowering top-down control mechanisms, the dynamical behavior of the robots is self-organized due to the local instabilities generated by the neural dynamics [12]. The robots are hence fully embodied [13], since there would be either no locomotion at all, if the sensorimotor loop was interrupted, or only a very limited set of internal control patterns would exist. By following this approach, we propose a dynamical systems type definition of embodiment. This relies on the comparison of the possible locomotion patterns and the internally generated patterns in the absence of the environmental feedback. As an example we have shown, that our barrel robot is also able to generate rolling dynamics, when the isolated actuator-controller system would otherwise converge to a stable fixpoint with no internal motion at all [14]. Furthermore, the emerging rolling modes, which appear additionally to the controller's own dynamics, demonstrate that the feedback of environment is indeed essential in the development of complex behavior primitives (similar conclusions has been drawn in Ref. [160]).

We have shown that the resulting locomotion modes correspond to self-organized limit-cycle and chaotic attractors in the combined phase space of internal

variables of the robot (body, actuator and controller) and of the external variables related to the environment. This separation is possible whenever the internal variables span an independent subspace of the system [15]. The dynamics of the barrel and spherical robots is independent of the position of the agent and the direction of propagation. These external variables are however still necessary for the interpretation of the behavior as robotic locomotion in general, or explorative behavior in particular. Due to the global symmetries the attractors are degenerate, forming a continuum in the plane of locomotion. When coexisting attractors are present, viz. in case of multistable systems [5], the long-term behavior depends on the initial conditions of internal variables, that determine which of the available attractors is selected from the overlapping continua.

In the absence of global symmetries of the physical space one can not talk - in the strict sense - about attractors in the overarching phase space. For practical applications it is, however, enough to consider local symmetries. Since most of the (human-made) world is highly structured, one may approximate it as the collection of locally symmetric areas attached to each other (e. g. a room, a staircase, a segment of the pavement). Each of these components may be extended virtually into an infinite manifold, for which the degenerate attractors are again well defined, being characterized by global symmetries. In structured environments, the locomotion may hence be interpreted in terms of these transiently attracting states [42], corresponding to the virtual attractors. Collisions with the static elements of the environment lead to a symmetry breaking, resetting the initial conditions of the system, allowing hence the switching between motion patterns, or giving access to otherwise unstable, non-attracting modes. Interactions with other agents can be interpreted analogously in terms of (discontinuous) attractor metadynamics [76].

We have also revealed a partially predictable chaotic phase [29] which allows for a smooth meandering in structured environments. The robots are able to explore complex maze-like arenas, without getting stuck in dead ends or in the corners of the corridors.

Our investigation is embedded in the long-standing effort to reduce the complexity of the control of robotic locomotion [16, 17], focusing in particular on the formation of attractors in the combined phase space of the robot and environment. This approach has been successful in understanding locomotion gaits in terms of limit-cycle attractors [18], we believe however that a systematic (dynamical systems type) theory of robotic locomotion would contribute significantly both to the design and to the construction of autonomous robots. The work presented here may be considered as the first steps in this direction.



# Chapter 5

## Conclusions

In this work we have discussed new extensions and applications of dynamical systems theory in various fields, such as computational neuroscience and robotics. We argued that extending the scope of classical concepts, like attractors, stability, and bifurcations, to high dimensional systems, may help in finding general principles underlying their dynamical behavior. We have stressed, however, that new methods also need to be developed, which allow for the design of dynamical systems with predefined properties, for the understanding of attractors in terms of embedded manifolds, or in general, for a more effective investigation of complex adaptive systems. The here presented contributions to the field aim to bridge the gap between low dimensional standard dynamical systems and high dimensional complex systems with applications in neuroscience and robotics.

Firstly, we have introduced a new mechanistic design procedure for constructing high dimensional multistable systems, which are ubiquitous in all areas of science [7]. The proposed versatile class of prototype dynamical systems allows for creating fixpoint, limit-cycle or chaotic attractors at predefined spacial coordinates (in a subspace of the system). We presented examples of 2- and 4-dimensional systems by constructing detailed bifurcation diagrams, providing also a general analytic proof for the generations of stable fixpoints and limit-cycles in arbitrary dimensions.

Secondly, using a neural network model with coexisting fixpoint attractors, we have demonstrated that transient-state dynamics may be generated by adding slow local variables to a multistable system [51]. Considering clique-encoding attractor networks of different sizes, we have shown that the stable fixpoints, corresponding to active cliques of excitatory neurons, are destabilized as a result of adding dynamic synapses exhibiting short-term synaptic plasticity. The generated transient-state dynamics corresponds to stable limit-cycle and chaotic attractors, in which the trajectory revisits the slow manifolds of former attractors.

Finally, we have extended the dynamical systems approach to the study of robotic locomotion, showing that motion patterns correspond to self-organized degenerate attractors in the combined phase space of the robot and environment [14, 15]. We considered cylindrical and spherical shaped rolling robots, for which the controllers consist of a single or respectively three proprioceptual neurons. By comparing the attractors of the actuator-controller system to the attractors of locomotion emerging in the overarching phase space, we coined a dynamical systems type of definition of embodiment and situatedness for locomoting robots. Investigating the stability domains of different rolling modes, we have also provided a novel interpretation of interactions with the passive and active constituents of the environment in terms of switching between coexisting attractors or attractor ruins of the system.

The results listed above confirm that multistable systems are able to generate many interesting phenomena: complex bifurcation cascades, transients-state dynamics and switching behavior. Whether the foundations of dynamical systems theory with the geometric view of attractors and trajectories does inhere the potential to be generalized and effectively extended to arbitrary high dimensional phase spaces still remains to be determined. There has been a growing desire to develop a general theory for overarching the gap between simple nonlinear systems [24] and quasi-infinite dimensional thermodynamic systems [169]. Several problems have been addressed in this context, ranging from the fundamental structure of regular windows occurring in higher dimensional chaotic systems [170] to the reconstruction of complex systems from measured data and time series [171].

To look at the bigger picture, we may zoom out even further and consider nonautonomous [25], modular [172], random [173] or time-delayed dynamical systems [174] as well. This opens up a whole world of exciting questions and problems, for which, especially in case of high dimensional state spaces, generic routes of solutions do not yet exist:

- Effect of delays. How can we handle delays in large neural networks? Is there a need to build delayed feedback mechanisms in artificial cognitive agents?
- Modulation vs. driving. For nonautonomous systems, is there a qualitative difference between modulation and driving? Is our brain only modulated by the sensori information or completely driven?
- Nonautonomous attractors. Can we interpret the dynamics of interacting or input-driven systems in terms of the autonomous attractors, and, if yes under which conditions?

The presented novel applications to complex adaptive and cognitive systems provide promising results. We believe, hence, that the questions posed above suggest new research goals, which are worth pursuing in the future.

# Appendix A

## Dynamical systems

### A.1 Phase space contraction rate

In three dimensions the change of a finite volume of a connected domain  $D(t)$ , with arbitrary size and shape, can be expressed using the Leibniz integral rule for differentiation under the integral sign:

$$\frac{dD(t)}{dt} = \frac{d}{dt} \int_{D(t)} dV = \oint_{\partial D(t)} \mathbf{v}_b \cdot d\mathbf{S} = \oint_{\partial D(t)} \mathbf{f} \cdot d\mathbf{S} = \int_{D(t)} \nabla \cdot \mathbf{f} dV \quad (\text{A.1})$$

where  $\mathbf{v}_b = \mathbf{f}$  denotes the speed of the boundary  $\partial D(t)$  of the domain  $D(t)$ , while  $dV$ ,  $d\mathbf{S}$  are infinitesimal volume element and surface vector, respectively. Now, assuming that  $\sigma(\mathbf{x}) = \nabla \cdot \mathbf{f}$  is constant within the infinitesimal phase space volume  $D(t) = V(t) \rightarrow 0$  around point  $\mathbf{x}$ , we can write:

$$\frac{dV(t)}{dt} = \sigma(\mathbf{x}) V(t). \quad (\text{A.2})$$

As an alternative approach [1] one can consider an  $n$  dimensional hypercube of volume  $V(t)$  and edge length  $\Delta x_i(t)$ :

$$V(t) = \prod_i \Delta x_i(t), \quad \Delta x_i(t) = x'_i(t) - x_i(t). \quad (\text{A.3})$$

The time derivative of the infinitesimal phase space volume, i. e. when  $\Delta x_i \rightarrow 0$ , can then be expressed in terms of the contraction rate  $\sigma(\mathbf{x}) = \nabla \cdot \mathbf{f}$  as:

$$\frac{dV(t)}{dt} = \frac{d}{dt} \prod_i \Delta x_i(t) = V(t) \sum_i \frac{\partial f_i}{\partial x_i} = (\nabla \cdot \mathbf{f}) V(t) = \sigma(\mathbf{x}) V(t), \quad (\text{A.4})$$

since  $\dot{x}_i = f_i(\dots, x_i, \dots)$  and  $\dot{x}'_i = f_i(\dots, x'_i, \dots)$ , and using the definition of partial derivatives,

$$\frac{\partial f_i}{\partial x_i} = \lim_{\Delta x_i \rightarrow 0} \frac{f_i(\dots, x_i + \Delta x_i, \dots) - f_i(\dots, x_i, \dots)}{\Delta x_i}. \quad (\text{A.5})$$

## A.2 Box-counting dimension

The box counting dimension is a natural generalization of the concept of dimension for fractal sets. Assuming that a fractal set lies in the  $n$  dimensional phase space, we can imagine covering the space by a grid of  $n$  dimensional hypercubes of edge length  $\varepsilon \ll 1$ . Counting then the minimum number of hypercubes  $N(\varepsilon)$  needed to cover the entire set yields a power law scaling with a negative power  $-D$ , where  $D > 0$  [22, 23]. The generally non-integer quantity  $D \in \mathbb{R}$  is called the box counting dimension,

$$D = \frac{\ln N(\varepsilon)}{\ln 1/\varepsilon}, \quad N(\varepsilon) \sim \varepsilon^{-D}, \quad \varepsilon \ll 1, \quad (\text{A.6})$$

which reduces to the traditional integer dimension values,  $D \in \mathbb{N}$ , in case of non-fractal structures.

## A.3 Lyapunov exponents

Here we briefly discuss the definition of the Lyapunov spectrum in case of maps. The spectrum of Lyapunov exponents,  $\lambda_k$ , can be defined analogously to Eq. 1.14, considering non-typical initial directions,  $\delta \mathbf{x}_0 \rightarrow 0$ , as well [28]. The time evolution of a perturbed trajectory,  $\mathbf{x}_t + \delta \mathbf{x}_t$ , can be expressed as:

$$\mathbf{x}_t + \delta \mathbf{x}_t = \mathbf{m}^{(t)}(\mathbf{x}_0 + \delta \mathbf{x}_0) \approx \mathbf{m}^{(t)}(\mathbf{x}_0) + \mathbf{J}_{\mathbf{m}^{(t)}}(\mathbf{x}_0) \delta \mathbf{x}_0, \quad (\text{A.7})$$

where  $\mathbf{m}^{(t)}$  denotes the  $t$ -th iterate of the map, while  $\mathbf{J}_{\mathbf{m}^{(t)}}(\mathbf{x}_0)$  is the corresponding Jacobian. The absolute value of the perturbation at time  $t$  is given (see Eq. (1.12)) hence by:

$$|\delta \mathbf{x}_t| = (\delta \mathbf{x}_0^T \mathbf{U}(\mathbf{x}_0, t) \delta \mathbf{x}_0)^{\frac{1}{2}}, \quad \mathbf{U}(\mathbf{x}_0, t) = \mathbf{J}_{\mathbf{m}^{(t)}}^T(\mathbf{x}_0) \mathbf{J}_{\mathbf{m}^{(t)}}(\mathbf{x}_0) \quad (\text{A.8})$$

with the  $T$  superscript denoting the transpose of the respective vector or matrix. Note that the  $\mathbf{U}(\mathbf{x}_0, t)$  matrix is a real symmetric matrix, having an orthogonal set of eigenvectors  $\mathbf{u}_k$  and positive eigenvalues  $\alpha_k(t) > 0$ .

According to the Oseledets theorem [22] in the limit of  $t \rightarrow \infty$  the Lyapunov exponents  $\lambda_k$  are independent of the initial position  $\mathbf{x}_0$ , resulting in (compare Eq. (1.14))

$$\lambda_k = \lim_{t \rightarrow \infty} \frac{1}{t} \ln \frac{|\delta \mathbf{x}_t|}{|\delta \mathbf{x}_0|} = \lim_{t \rightarrow \infty} \frac{1}{2t} \ln \frac{\delta \mathbf{x}_0^T \mathbf{U}(\mathbf{x}_0, t) \delta \mathbf{x}_0}{|\delta \mathbf{x}_0|^2} = \lim_{t \rightarrow \infty} \frac{\ln \alpha_k(t)}{2t}. \quad (\text{A.9})$$

The existence of the limit is guaranteed by the Oseledets theorem under very general circumstances [28]. The direction of initial perturbation  $\delta \mathbf{x}_0$ , with respect to the orthogonal basis set  $\mathbf{u}_k$ , determines then which of the eigenvalues

$\alpha_1 > \alpha_2 > \dots > \alpha_n > 0$  is selected by the limit. Since a typical perturbation would generally have a finite component in the  $\mathbf{u}_1$  direction, corresponding to the maximal (largest) Lyapunov exponent  $\lambda_m = \lambda_1$ , the numerical computation of the full spectrum is not always straightforward. In practice, when attempting to compute the Lyapunov exponents  $\lambda_k$  numerically, one may follow for example Bennetin's method [175], which relies on the Gramm-Schmidt orthogonalization procedure [22] for estimating the individual  $\mathbf{u}_k$  directions.

## A.4 Coordinate transformations and stability

In **Chapter 1** we argued that it is often more convenient to investigate the behavior of a dynamical system in terms of new variables. This change of variables involves generally a nonlinear coordinate transformation. It is, however, not obvious how the transformation affects the flow in the phase space.

Here, we show that transformations may not change stability of attractors, viz. to give an example, a stable fixpoint or limit cycle remains stable in the new coordinate system as well. After defining linear and nonlinear transformations, we prove that for fixpoints of flows and for periodic points of maps the nonlinear change of variables reduces to a simple linear transformation. The eigenvalues, characterizing their stability, remain hence unchanged even under nonlinear transformations. Finally, we demonstrate that this is not generally true for the other points (not fixpoints) of the phase space, allowing for example for a qualitatively different phase space dynamics with respect to the one in the original coordinate system.

### A.4.1 Linear transformations and eigenvalues

It is easy to show that the eigenvalues  $\lambda \in \mathbb{C}$  of an  $n \times n$  real matrix  $\mathbf{A}$ , corresponding to eigenvectors  $\mathbf{x}$ ,

$$\mathbf{A} \mathbf{x} = \lambda \mathbf{x}, \quad \mathbf{x} = (x_1, \dots, x_n), \quad (\text{A.10})$$

are invariant under linear coordinate transformations,

$$\mathbf{y} = \mathbf{T}^{-1} \mathbf{x}, \quad \mathbf{y} = (y_1, \dots, y_n), \quad (\text{A.11})$$

where  $\mathbf{T}$  is the  $n \times n$  matrix form of a linear transformation:

$$\mathbf{B} \mathbf{y} = \lambda \mathbf{y}, \quad \mathbf{B} = \mathbf{T}^{-1} \mathbf{A} \mathbf{T}. \quad (\text{A.12})$$

Therefore, matrix  $\mathbf{B}$  (which is just the equivalent of  $\mathbf{A}$  but represented in the new basis) has the same eigenvalues  $\lambda$  as in the original coordinate system.

### A.4.2 Nonlinear transformations

Turning now to smooth but nonlinear, invertible coordinate transformations by considering:

$$\mathbf{y} = \mathbf{g}(\mathbf{x}), \quad \mathbf{g} = (g_1, \dots, g_n), \quad (\text{A.13})$$

with the inverse transformation

$$\mathbf{x} = \mathbf{g}^{-1}(\mathbf{y}), \quad \mathbf{g}^{-1} = (g_1^{-1}, \dots, g_n^{-1}), \quad (\text{A.14})$$

we can linearize Eq. (A.13) around any point  $\mathbf{x}^*$ :

$$\delta \mathbf{y} = \mathbf{J}_{\mathbf{g}}(\mathbf{x}^*) \delta \mathbf{x}, \quad \mathbf{x} = \mathbf{x}^* + \delta \mathbf{x}, \quad \mathbf{y} = \mathbf{y}^* + \delta \mathbf{y}, \quad (\text{A.15})$$

where  $|\delta \mathbf{x}| \rightarrow 0$  and  $|\delta \mathbf{y}| \rightarrow 0$ . The symbol  $\mathbf{J}_{\mathbf{g}}(\mathbf{x}^*)$  denotes the Jacobian matrix

$$\mathbf{J}_{\mathbf{g}} = \frac{\partial(g_1, \dots, g_n)}{\partial(x_1, \dots, x_n)} = \frac{\partial \mathbf{g}}{\partial \mathbf{x}}, \quad (\mathbf{J}_{\mathbf{g}}(\mathbf{x}^*))_{ij} = \left. \frac{\partial g_i(\mathbf{x})}{\partial x_j} \right|_{\mathbf{x}^*} \quad (\text{A.16})$$

evaluated at point  $\mathbf{x}^*$ . Hence, nonlinear transformations can be locally replaced by a linear transformation  $\mathbf{T} = \mathbf{J}_{\mathbf{g}}^{-1}$ , corresponding to the inverse of Jacobian matrix  $\mathbf{J}_{\mathbf{g}}$ .

### A.4.3 Fixpoints of continuous time systems

Applying now the nonlinear transformation  $\mathbf{y} = \mathbf{g}(\mathbf{x})$  to the phase space of a general dynamical system, as defined by Eq. (1.1), one can express the ODE in terms of the new variables  $\mathbf{y}$ :

$$\dot{\mathbf{y}} = \frac{\partial \mathbf{g}}{\partial \mathbf{x}} \dot{\mathbf{x}} = \mathbf{J}_{\mathbf{g}}(\mathbf{x}(\mathbf{y})) \mathbf{f}(\mathbf{x}(\mathbf{y})) = \mathbf{h}(\mathbf{y}), \quad (\text{A.17})$$

where  $\mathbf{h}$  denotes the new right-hand-side vector function defining the dynamics. We can perform now the linearization around  $\mathbf{y}^* = \mathbf{g}(\mathbf{x}^*)$ , with  $\mathbf{y} = \mathbf{y}^* + \delta \mathbf{y}$  and  $|\delta \mathbf{y}| \rightarrow 0$ , analogously to Eq. (1.10), in the new coordinate system:

$$\dot{\mathbf{y}} = \mathbf{h}(\mathbf{y}) \approx \mathbf{h}(\mathbf{y}^*) + \mathbf{J}_{\mathbf{h}}(\mathbf{y}^*) \delta \mathbf{y} + \dots, \quad (\text{A.18})$$

with the Jacobian matrix  $\mathbf{J}_{\mathbf{h}}(\mathbf{y}^*)$  evaluated at point  $\mathbf{y}^*$ :

$$\mathbf{J}_{\mathbf{h}} = \frac{\partial(h_1, \dots, h_n)}{\partial(y_1, \dots, y_n)} = \frac{\partial \mathbf{h}}{\partial \mathbf{y}}, \quad (\mathbf{J}_{\mathbf{h}}(\mathbf{y}^*))_{ij} = \left. \frac{\partial h_i(\mathbf{y})}{\partial y_j} \right|_{\mathbf{y}^*}. \quad (\text{A.19})$$

Using Eq. (A.17), the Jacobian  $\mathbf{J}_{\mathbf{h}}$  can be calculated with the generalized chain rule:

$$\begin{aligned} \frac{\partial \mathbf{h}}{\partial \mathbf{y}} &= \frac{\partial}{\partial \mathbf{y}} \left( \frac{\partial \mathbf{g}}{\partial \mathbf{x}} \right) \mathbf{f}(\mathbf{x}(\mathbf{y})) + \frac{\partial \mathbf{g}}{\partial \mathbf{x}} \frac{\partial \mathbf{f}}{\partial \mathbf{x}} \frac{\partial \mathbf{x}}{\partial \mathbf{y}} \\ &= \frac{\partial}{\partial \mathbf{y}} \left( \frac{\partial \mathbf{g}}{\partial \mathbf{x}} \right) \mathbf{f}(\mathbf{x}(\mathbf{y})) + \frac{\partial \mathbf{g}}{\partial \mathbf{x}} \frac{\partial \mathbf{f}}{\partial \mathbf{x}} \left( \frac{\partial \mathbf{g}}{\partial \mathbf{x}} \right)^{-1}, \end{aligned} \quad (\text{A.20})$$

where we have used that matrices of partial derivatives satisfy

$$\frac{\partial \mathbf{x}}{\partial \mathbf{y}} = \left( \frac{\partial \mathbf{y}}{\partial \mathbf{x}} \right)^{-1} = \left( \frac{\partial \mathbf{g}}{\partial \mathbf{x}} \right)^{-1}. \quad (\text{A.21})$$

Hence, if  $\mathbf{x}^*$  is a fixpoint,  $\mathbf{f}(\mathbf{x}^*) = 0$ , the Jacobian  $\mathbf{J}_h$  is related to the original matrix  $\mathbf{J}_f$  by a linear transformation:

$$\mathbf{J}_h = \bar{\mathbf{H}} \mathbf{f}(\mathbf{x}^*) + \mathbf{J}_g \mathbf{J}_f (\mathbf{J}_g)^{-1} = \mathbf{J}_g \mathbf{J}_f (\mathbf{J}_g)^{-1}. \quad (\text{A.22})$$

Here  $\bar{\mathbf{H}}$  denotes a three dimensional matrix, which can be written, by using the Einstein summation convention as:

$$(\bar{\mathbf{H}})_{ijk} = \frac{\partial}{\partial x_l} \left( \frac{\partial g_i}{\partial x_k} \right) \frac{\partial x_l}{\partial y_j}, \quad \bar{\mathbf{H}} = \frac{\partial}{\partial \mathbf{y}} \left( \frac{\partial \mathbf{g}}{\partial \mathbf{x}} \right). \quad (\text{A.23})$$

We can conclude, hence, that the eigenvalues, and thus the stability of a fixpoint does not change under any smooth, invertible nonlinear coordinate transformation.

This does not preclude, however, that the phase space contraction rate of general points, different from equilibrium points,  $\sigma(\mathbf{x}) = \text{tr}(J(\mathbf{x}))$ , changes when going from one coordinate system to another.

#### A.4.4 Fixpoints of maps

One can show analogously that, as expected, the conclusion from above also holds for discrete time maps (1.2). The coordinate transformation  $\mathbf{y} = \mathbf{g}(\mathbf{x})$  yields an equivalent map, denoted here by  $\mathbf{M}$ :

$$\mathbf{y}_{t+1} = \mathbf{g}(\mathbf{x}_{t+1}) = \mathbf{g}(\mathbf{m}(\mathbf{x}_t)) = \mathbf{M}(\mathbf{y}_t), \quad (\text{A.24})$$

and the corresponding Jacobian:

$$\mathbf{J}_M = \frac{\partial(M_1, \dots, M_n)}{\partial(y_1, \dots, y_n)} = \frac{\partial \mathbf{M}}{\partial \mathbf{y}}, \quad (\mathbf{J}_M(\mathbf{y}^*))_{ij} = \left. \frac{\partial M_i(\mathbf{y})}{\partial y_j} \right|_{\mathbf{y}^*}, \quad (\text{A.25})$$

Assuming again that  $\mathbf{x}^*$  is a fixpoint,  $\mathbf{x}_{t+1}^* = \mathbf{m}(\mathbf{x}_t^*)$ , the matrix can be written via

$$\frac{\partial \mathbf{M}}{\partial \mathbf{y}} = \frac{\partial \mathbf{g}}{\partial \mathbf{m}} \frac{\partial \mathbf{m}}{\partial \mathbf{x}} \frac{\partial \mathbf{x}}{\partial \mathbf{y}} = \frac{\partial \mathbf{g}}{\partial \mathbf{x}} \frac{\partial \mathbf{m}}{\partial \mathbf{x}} \left( \frac{\partial \mathbf{g}}{\partial \mathbf{x}} \right)^{-1}. \quad (\text{A.26})$$

as a linear transformation of  $\mathbf{J}_m$ :

$$\mathbf{J}_M = \mathbf{J}_g \mathbf{J}_m (\mathbf{J}_g)^{-1} \quad (\text{A.27})$$

Consequently, nonlinear variable transformations do not change the stability of fixpoints.

Furthermore, since limit cycles can be represented as fixpoints of the corresponding Poincarè maps, the arguments from above also hold in that case. Thus one should expect that limit cycles do not “get destroyed” by change of variables.

### A.4.5 Phase space contraction

To present an interesting example of how coordinate transformations affect the phase space contraction rate we consider the normal form of a Hopf-bifurcation in polar coordinates  $(r, \varphi)$  [1]:

$$\begin{aligned}\dot{r} &= f_1(r, \varphi) = r(\Gamma - r^2) \\ \dot{\varphi} &= f_2(r, \varphi) = \omega,\end{aligned}\tag{A.28}$$

where  $\omega$  is a constant angular velocity, while  $\Gamma > 0$  is setting the radius of the limit cycle,  $r_1^* = \sqrt{\Gamma}$ . The fixpoint  $r_0^* = 0$  of the radial part is only stable for  $\Gamma < 0$ , i. e. before the supercritical Hopf-bifurcation occurring at  $\Gamma = 0$ . Using the well-known transformations back to Cartesian coordinates,

$$\begin{aligned}x &= g_1(r, \varphi) = r \cos \varphi \\ y &= g_2(r, \varphi) = r \sin \varphi,\end{aligned}\tag{A.29}$$

we get the equivalent set of ODE-s:

$$\begin{aligned}\dot{x} &= h_1(r, \varphi) = -\omega y + x(\Gamma - x^2 - y^2) \\ \dot{y} &= h_2(r, \varphi) = \omega x + y(\Gamma - x^2 - y^2),\end{aligned}\tag{A.30}$$

which describes the dynamics in the  $(x, y)$  space.

We can calculate now the phase space contraction rate in both representations using Eq. (1.3):

$$\sigma(r, \varphi) = \nabla \cdot \mathbf{f} = \text{tr}(J_{\mathbf{f}}) = \Gamma - 3r^2,\tag{A.31}$$

$$\sigma(x, y) = \nabla \cdot \mathbf{h} = \text{tr}(J_{\mathbf{h}}) = 2\Gamma - 4r^2.\tag{A.32}$$

As we can see, the contraction rate depends on the coordinate system considered. It is, however, always negative at the radius of the cycle,  $\sigma(r_1^*, \varphi) = \sigma(x_1^*(\varphi), y_1^*(\varphi)) = -2\Gamma$ . Thus, the limit cycle is an attractor in both coordinate systems. On the other hand,  $r_1^* = \sqrt{\Gamma}$  is not a fixpoint of the full system,  $f_1(r_1^*, \varphi) = 0$  but  $f_2(r_1^*, \varphi) \neq 0$ . Hence, the transformation changes the eigenvalues of the Jacobian calculated at this radius. The sum of eigenvalues, i. e. the contraction rate, nevertheless, remains invariant under this transformation.

# Appendix B

## Prototype system

### B.1 Potential wells with arbitrary shape

Here, we provide a simple generalization of the potential functions introduced in Sec. 2.2.3 of **Chapter 2**, to construct minima of arbitrary shapes. Consider the potential  $V(\mathbf{x})$  defined by Eq. (2.9) having  $M$  number of predefined minima  $V(\mathbf{x}_m) = V_m$  at positions  $\mathbf{x}_m$ . By replacing the original  $g_m(\mathbf{z})$  hyperbolic tangent function in Eq. (2.9) to the

$$g_m^s(\Delta\mathbf{x}) = \tanh\left(\frac{|\Delta\mathbf{x}|}{z_m^s(\Delta\mathbf{x})}\right)^2, \quad (\text{B.1})$$

non-symmetric version, one can control the shape of the potential well around the minimum by suitably defined auxiliary functions  $z_m^s(\Delta\mathbf{x})$ .

As an example we consider the 2-dimensional potential function,

$$V(\mathbf{x}) = g_1^s(\mathbf{x} - \mathbf{x}_1) g_2^s(\mathbf{x} - \mathbf{x}_2), \quad (\text{B.2})$$

with two minima at  $\mathbf{x}_1 = (-1, 1)$  and  $\mathbf{x}_2 = (1, -1)$ , respectively. The symmetric double-well potential, used in **Chapter 2**, may be easily reproduced for constant shaping functions,  $z_{1,2}^s(\Delta\mathbf{x}) = z_{1,2}$ , as shown in the left panel of Fig. B.1.

Considering general  $z_m^s$  functions one can easily create minima of arbitrary shapes. To compare the potential functions with symmetric and non-symmetric minima, in the right plot of Fig. B.1 two possible shapes are presented, using the:

$$\begin{aligned} z_1^s(\Delta\mathbf{x}) &= z_1 + a_1 \cos(2\theta) \\ z_2^s(\Delta\mathbf{x}) &= z_2 + a_2 \cos(\theta) \cdot (\cos(\theta) - 1) \cdot (\cos(\theta) + 1) \end{aligned} \quad (\text{B.3})$$

shaping functions, respectively. The angle,

$$\theta = \theta(\Delta\mathbf{x}) = \arccos(\Delta x_1/|\Delta\mathbf{x}|) \quad (\text{B.4})$$

is measured between the  $\Delta\mathbf{x} = (\Delta x_1, \Delta x_2)$  vector and the  $x_1$  axis.

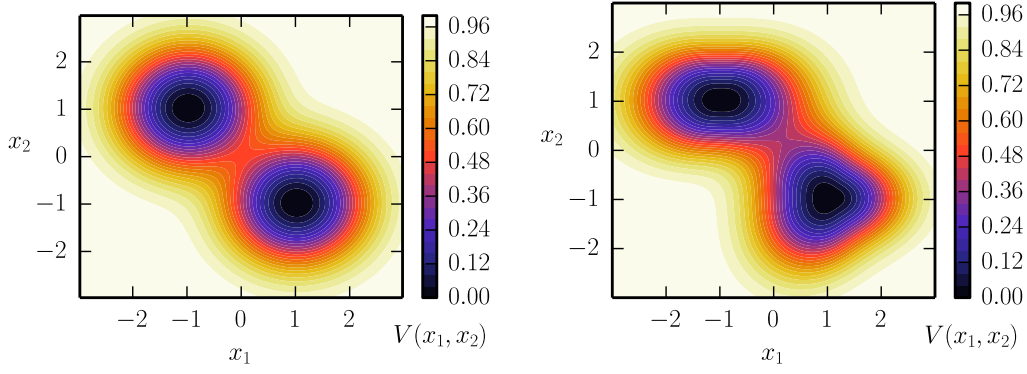


**Figure B.1:** Comparison of double well potential functions. The color coding for  $V(x_1, x_2)$  is indicated by the color bar on the right of the diagram. **Left:** Symmetric double potential well with  $z_{1,2} = 1.5$ , compare Fig. 2.6. **Right:** General 2-dimensional potential well with two minima using the  $z_{1,2}^s(\Delta\mathbf{x})$  shaping functions, defined by (B.3), with  $a_1 = 0.3$  and  $a_2 = 0.6$ .

## B.2 Bifurcations in the 4-dimensional system

As discussed in Sec. 2.2, the fixpoints  $\mathbf{p}_{1,2}^* = (\pm 1, \mp 1, 0, 0)$  of the prototype system, corresponding to the minima of the symmetric double-well potential shown in Fig. 2.6, undergo supercritical Hopf bifurcations as the control parameter changes sign at  $\mu_1 = 0$ . Due to the symmetry of the system, the Hopf points are characterized (see Sec. 2.4) by a double pair of purely imaginary eigenvalues,

$$\lambda_{1,2,3,4} = \pm i\sqrt{\gamma}, \quad \gamma = \left. \frac{\partial^2 V}{\partial x_{1,2}^2} \right|_{x_1^*, x_2^*}, \quad (\text{B.5})$$

which allow for the creation of a second set of limit cycles, additionally to the ones presented in Fig. 2.8.

These limit cycles are unstable, see the left plot of Fig. B.2 for almost the entire parameter interval investigated here, also having a perpendicular alignment with respect to the ones presented in the main text (see the right plot). We note, however, that the intermittent chaotic dynamics shown in Fig. 2.9 is organized partly by this second branch of unstable limit cycles. For  $\mu_1 = 0.34$  the limit cycles are hyperbolic, having two stable and one unstable directions. The trajectories are hence transiently attracted to these unstable cycles (which are embedded to the chaotic attractor), generating the bursting dynamics perpendicular to the (1,-1) symmetry axis of the potential function (compare Fig. 2.9).

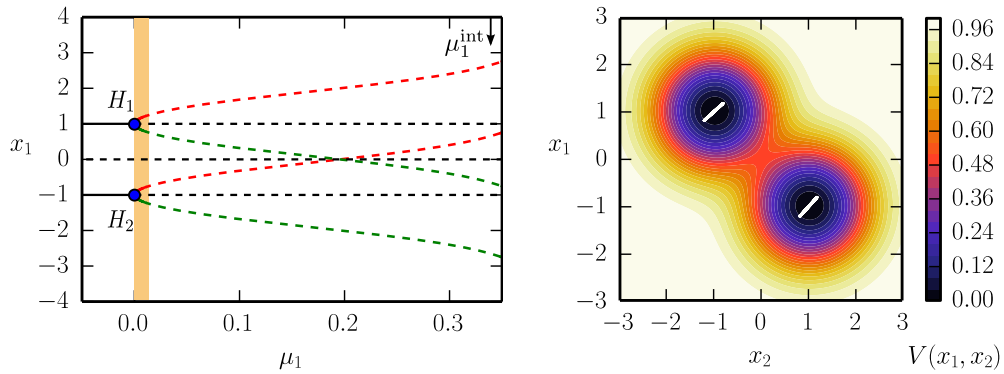


**Figure B.2:** The second branch of limit cycles of the 4-dimensional prototype system with the symmetrical double-well potential (with parameters as for Fig. 2.7). **Left:** The bifurcation diagram showing only the fixpoints and the second branch of limit cycles (compare Fig. 2.8). Stable/unstable fixpoints are indicated by the black continuous/dashed lines. Maximal/minimal  $x_1$ -values of the respective limit cycles are illustrated by the red/green dashed lines. The limit cycles are mostly unstable, except for the orange shaded parameter interval after the supercritical Hopf bifurcations  $H_{1,2}$ . Intermittent chaos (see Fig. 2.9) was found for  $\mu_1^{int} = 0.34$ , indicated by the arrow in the top right corner. **Right:** Projection of the limit cycles to the  $(x_1, x_2)$  plane for  $\mu_1 = 0.008$  (from the orange shaded region in the left). The minima of the double-well potential function  $V(x_1, x_2)$  are color-coded.

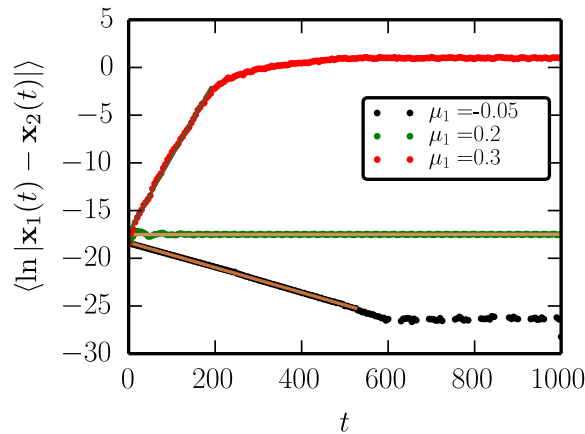


**Figure B.3:** Computation of the largest Lyapunov exponent  $\lambda_m$ . The logarithmic distance  $\langle \ln |\mathbf{x}_1(t) - \mathbf{x}_2(t)| \rangle$  is shown as a function of time, averaged over 100 pairs of trajectories  $\mathbf{x}_{1,2}(t)$ . The maximal Lyapunov exponents  $\lambda_m = -0.01 / 0 / 0.08$  are determined by the slope of the linear fits (brown lines) to the first part of the black/green/red trajectories, respectively. The control parameter values  $\mu_1 = -0.05/0.2/0.3$  correspond to fixpoint/limit-cycle/chaotic attractors (compare Fig. 2.8). The dashed line indicates that the maximal accuracy of the integrator has been reached.

### B.3 Lyapunov exponent

In this section we discuss the computation of the maximal Lyapunov exponent  $\lambda_m$  for the 4-dimensional prototype system with the double-well potential function discussed in Sec. 2.3.2 of **Chapter 2**.

To determine the largest Lyapunov exponent  $\lambda_m$  (plotted in Fig. 2.8) we follow the method described in Sec. 1.1.3. For every value of the control parameter  $\mu_1$  first we let the trajectory converge to the attractor by discarding the transients corresponding to the first  $t_{tr} = 1.5 \cdot 10^4$  time units. The Lyapunov exponent  $\lambda_m$  is then given by the slope of the initial linear part of the logarithmic distance,

$$\langle \ln |\mathbf{x}_1(t) - \mathbf{x}_2(t)| \rangle \approx \lambda_m t + \ln \delta_{12}, \quad (\text{B.6})$$

averaged over 100 pairs of trajectories  $\mathbf{x}_{1,2}(t)$  on the attractor of initial distance  $\delta_{12} = |\mathbf{x}_1(0) - \mathbf{x}_2(0)| = 10^{-8}$ . The initial slope of the logarithmic displacements is indicated in Fig. B.3) for three different control parameters  $\mu_1$ , corresponding to a fixpoint, to a limit-cycle and to a chaotic attractor, respectively.

# Appendix C

## Neural networks

### C.1 Chaotic dynamics in the symmetric network

In Sec. 3.2.2 of **Chapter 3** we have discussed the bifurcations leading to the transient-state dynamics. The bifurcation diagram as a function of the input strength  $I$  shown in Fig. 3.6 indicates a region with chaotic behavior. Inspecting the time-series corresponding to this chaotic behavior, as plotted in Fig. C.1, we find oscillations around the destabilized clique state. These unstable fixpoints are of saddle-focus type, i. e. the Jacobian matrix has a pair of complex eigenvalues with positive real parts, while the other eigenvalues being either negative or complex with negative real parts. The trajectory revisits these fixpoints, producing small amplitude oscillations around them. To check whether a heteroclinic contour [47] (cf. Sec. 1.1.5) also exists due to the  $C_4$  symmetry, needs further investigations. Also note that the chaotic dynamics is intermittent, the small amplitude oscillations are interceded by the sequential switching behavior (cf. Fig. 3.4), which is, however, not stable here.

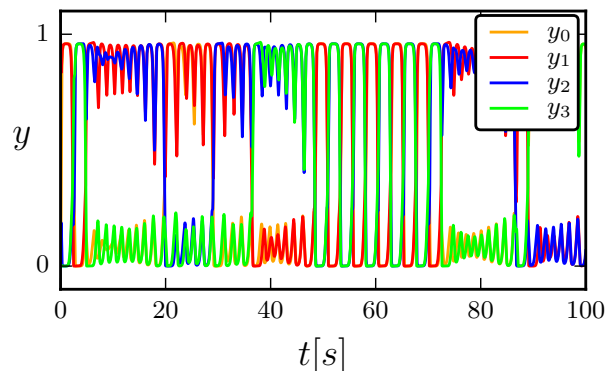


**Figure C.1:** *The time-series of firing-rates  $y_i$  showing intermittent chaotic-like transient-state dynamics for the  $N = 4$  neuron network (see Fig. 3.3) and input current  $I = -6.8$  Hz. The other parameters are as for Fig. 3.4.*



# Appendix D

## Robots

The simulation parameters used for the barrel robot in Sec. 4.2.1, respectively for the spherical robot in Sec. 4.3 of **Chapter 4** are summarized in the following two tables, indicating: the parameter name employed in the text / the name of the C++ variable in the LpzRobots simulation environment / the notation used in the thesis / their values or the parameter ranges / the units of measure in the International System of Units in the first / second / third / fourth / last columns, respectively.

### D.1 Simulation parameters of the barrel robot

Parameter name	LpzRobots var.	Symbol	Value	Unit
slope of $y(x)$	a	$a$	[1.2, 2]	-
adaption rate	eps	$\varepsilon$	[0, 1]	-
normalized spring const.	-	$\Omega$	$\sqrt{200}$	1/s
normalized damping	-	$\beta$	$2\Omega$	1/s
mass of the small ball	pendularmass	$m$	1	1 kg
spring constant	motorpowerfactor	$k$	200	1 kg/s <sup>2</sup>
damping	-	$\gamma$	$2\sqrt{km}$	1 kg/s
mass of the barrel	spheremass	$M$	1	1 kg
diameter of the barrel	diameter	$2R$	2	1 m
rolling friction coeff.	friction	$\Psi$	0.3	1 m <sup>2</sup> kg/s
gravitational acceleration	gravity	$g$	9.81	1 m/s <sup>2</sup>
simulation stepsize	simstepsize	$dt$	0.001	1 s
-	noise	-	0	-
-	controlinterval	-	1	-
-	pendularrange	-	0.5	-
-	roughness	-	0.8	-
-	hardness	-	40	-
-	slip	-	0.01	-
-	elasticity	-	0.5	-

## D.2 Simulation parameters of the spherical robot

Parameter name	LpzRobots var.	Symbol	Value	Unit
gain	a	$a$	0.4	-
threshold	b	$b$	0	-
leak constant	gamma	$\Gamma$	20	1 s
excitatory weight	w_0	$w_0$	[120, 300]	1 Hz
inhibitory weight	z_0	$z_0$	[50, 800]	1 Hz
calcium time constant	T_u	$T_u$	0.3	1 s
neurotr. time constant	T_phi	$T_\varphi$	0.6	1 s
calcium limit	U_max	$U_{\max}$	{1, 4}	-
mass of the small balls	pendularmass	$m$	1	1 kg
spring constant	motorpowerfactor	$k$	120	1 kg/s <sup>2</sup>
damping	-	$\gamma$	$2\sqrt{km}$	1 kg/s
mass of the sphere	spheremass	$M$	1	1 kg
diameter of the sphere	diameter	$2R$	0.5	1 m
scaling factor	r	$2p$	1	-
rolling friction coeff.	friction	$\Psi$	0.3	1 m <sup>2</sup> kg/s
gravitational acceleration	gravity	$g$	9.81	1 m/s <sup>2</sup>
simulation stepsize	simstepsize	$dt$	0.001	1 s
-	noise	-	0	-
-	controlinterval	-	1	-
-	pendularrange	-	0.5	-
-	roughness	-	0.8	-
-	hardness	-	40	-
-	slip	-	0.01	-
-	elasticity	-	0.5	-

The simulations can be reproduced by using the LpzRobots simulation software, available on <http://robot.informatik.uni-leipzig.de/software> or <https://github.com/georgmartius/lpzrobots>.

### D.3 Stability of the motion primitives

Here, we examine the stability of the rolling modes of the sphere robot, shown in Figs. 4.10 and 4.11, in the presence of sensory noise. We find that all attractors are resistant to relatively high noise levels (see Fig. D.1), the less stable ones being the T1 and S3 modes, which are characterized by the smallest stability domains in the  $(w_0, z_0)$  parameter space.

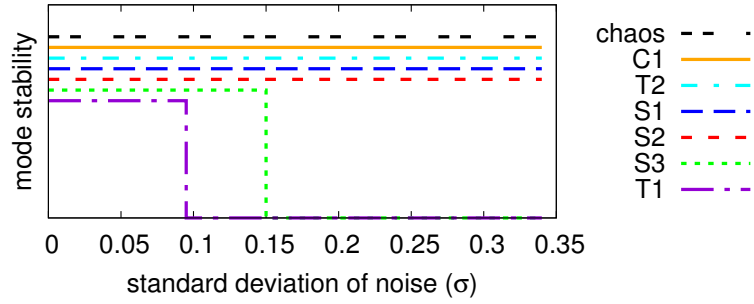


**Figure D.1:** *The stability of the locomotion modes found for  $U_{max} = 1$ , compare Fig. 4.10. The mode stability is indicated simply in a binary manner (denoting with 0 the unstable behavior) as a function of the noise term  $\Delta x$  in the sensory reading of the actual positions, defined by  $x_i^{(a)} \rightarrow x_i^{(a)}(1 + \Delta x)$ . The noise  $\Delta x$  is normal-distributed with standard deviation  $\sigma$ .*



# References

- [1] Claudius Gros. *Complex and Adaptive Dynamical Systems*. Springer International Publishing, Chambridge-Heidelberg, 2015.
- [2] Gustavo Deco, Viktor K Jirsa, and Anthony R McIntosh. Emerging concepts for the dynamical organization of resting-state activity in the brain. *Nature reviews. Neuroscience*, 12(1):43–56, 2011.
- [3] Mikhail I Rabinovich, Ramón Huerta, Pablo Varona, and Valentin S Afraimovich. Transient Cognitive Dynamics, Metastability, and Decision Making. *PLOS Computational Biology*, 4(5):1–9, 2008.
- [4] Steven H. Strogatz. Exploring complex networks. *Nature*, 410(6825):268–276, 2001.
- [5] Alexander N. Pisarchik and Ulrike Feudel. Control of multistability. *Physics Reports*, 540(4):167–218, 2014.
- [6] Ulrike Feudel. Complex dynamics in multistable systems. *International Journal of Bifurcation and Chaos*, 18(06):1607–1626, 2008.
- [7] Bulcsú Sándor and Claudius Gros. A versatile class of prototype dynamical systems for complex bifurcation cascades of limit cycles. *Scientific Reports*, 5:12316, 2015.
- [8] Mikhail I Rabinovich, Pablo Varona, Allen I Selverston, and Henry D I Abarbanel. Dynamical principles in neuroscience. *Reviews of modern physics*, 78(4):1213, 2006.
- [9] Claudius Gros. Neural networks with transient state dynamics. *New Journal of Physics*, 9(4):109, 2007.
- [10] Robert S Zucker and Wade G Regehr. Short-term synaptic plasticity. *Annual review of physiology*, 64(1):355–405, 2002.
- [11] Jeffrey Aguilar, Tingnan Zhang, Feifei Qian, Mark Kingsbury, Benjamin McInroe, Nicole Mazouchova, Chen Li, Ryan Maladen, Chaohui Gong, Matt Travers, Ross L Hatton, Howie Choset, Paul B Umbanhowar, and Daniel I Goldman. A review on locomotion robotics: the study of movement at

- the intersection of robotics, soft matter and dynamical systems. *Reports on Progress in Physics*, 79(11):110001, 2016.
- [12] Ralf Der and Georg Martius. *The Playful Machine: Theoretical Foundation and Practical Realization of Self-Organizing Robots*, volume 15. Springer Science & Business Media, 2012.
- [13] Tom Ziemke. What’s that thing called embodiment. In *Proceedings of the 25th Annual meeting of the Cognitive Science Society*, pages 1305–1310. Mahwah, NJ: Lawrence Erlbaum, 2003.
- [14] Bulcsú Sándor, Tim Jahn, Laura Martin, and Claudius Gros. The sensorimotor loop as a dynamical system: How regular motion primitives may emerge from self-organized limit cycles. *Frontiers in Robotics and AI*, 2:31, 2015.
- [15] Laura Martin, Bulcsú Sándor, and Claudius Gros. Closed-loop robots driven by short-term synaptic plasticity: Emergent explorative vs. limit-cycle locomotion. *Frontiers in Neurobotics*, 10, 2016.
- [16] JAS Kelso. The informational character of self-organized coordination dynamics. *Human Movement Science*, 13(3):393–413, 1994.
- [17] Ralf Der and Georg Martius. Novel plasticity rule can explain the development of sensorimotor intelligence. *Proceedings of the National Academy of Sciences*, 112(45):E6224–E6232, 2015.
- [18] Matt Travers, Alex Ansari, and Howie Choset. A dynamical systems approach to obstacle navigation for a series-elastic hexapod robot. In *Decision and Control (CDC), 2016 IEEE 55th Conference on*, pages 5152–5157. IEEE, 2016.
- [19] R. Pfeifer, M. Lungarella, and F. Iida. Self-Organization, Embodiment, and Biologically Inspired Robotics. *Science*, 318(5853):1088–1093, 2007.
- [20] David Sussillo and Omri Barak. Opening the black box: low-dimensional dynamics in high-dimensional recurrent neural networks. *Neural computation*, 25(3):626–49, 2013.
- [21] Steven H Strogatz. *Nonlinear dynamics and chaos: with applications to physics, biology, chemistry, and engineering*. Westview press, 2014.
- [22] Edward Ott. *Chaos in dynamical systems*. Cambridge university press, 2002.
- [23] Tamás Tél and Márton Gruiz. *Chaotic dynamics: An introduction based on classical mechanics*. Cambridge University Press, 2006.
- [24] Kathleen T Alligood, Tim D Sauer, and James A Yorke. Chaos. In *Chaos*, pages 105–147. Springer, 1997.

- [25] Peter E Kloeden and Martin Rasmussen. *Nonautonomous dynamical systems*. Number 176. American Mathematical Soc., 2011.
- [26] Peter E. Kloeden and C. Poetsche. Nonautonomous Dynamical Systems in the Life Sciences. In *Nonautonomous Dynamical Systems in the Life Sciences*, volume 2102, pages 199–224. Springer, 2013.
- [27] B. Mandelbrot. How Long Is the Coast of Britain? Statistical Self-Similarity and Fractional Dimension. *Science*, 156(3775):636–638, 1967.
- [28] Arkady Pikovsky and Antonio Politi. *Lyapunov Exponents: A Tool to Explore Complex Dynamics*. Cambridge University Press, 2016.
- [29] Hendrik Wernecke, Bulcsú Sándor, and Claudius Gros. How to test for partially predictable chaos. *Scientific Reports*, 7(1):1087, 2017.
- [30] Suso Kraut and Ulrike Feudel. Multistability, noise, and attractor hopping: The crucial role of chaotic saddles. *Phys. Rev. E*, 66(1):15207, 2002.
- [31] Adilson E. Motter, Márton Gruiz, György Károlyi, and Tamás Tél. Doubly transient chaos: Generic form of chaos in autonomous dissipative systems. *Physical Review Letters*, 111(19):194101, 2013.
- [32] A Chudzik, P Perlikowski, A Stefanski, and T Kapitaniak. Multistability and rare attractors in van der Pol-Duffing oscillator. *International Journal of Bifurcation and Chaos*, 21(07):1907–1912, 2011.
- [33] Marten Scheffer, Jordi Bascompte, William A Brock, Victor Brovkin, Stephen R Carpenter, Vasilis Dakos, Hermann Held, Egbert H Van Nes, Max Rietkerk, and George Sugihara. Early-warning signals for critical transitions. *Nature*, 461(7260):53–59, 2009.
- [34] Dawid Dudkowski, Sajad Jafari, Tomasz Kapitaniak, Nikolay V. Kuznetsov, Gennady A. Leonov, and Awadhesh Prasad. Hidden attractors in dynamical systems. *Physics Reports*, 637:1–50, 2016.
- [35] G.A. Leonov, N.V. Kuznetsov, and V.I. Vagaitsev. Localization of hidden Chua’s attractors. *Physics Letters A*, 375(23):2230–2233, 2011.
- [36] Daniel A Wiley, Steven H Strogatz, and Michelle Girvan. The size of the sync basin. *Chaos: An Interdisciplinary Journal of Nonlinear Science*, 16(1):15103, 2006.
- [37] Peter J Menck, Jobst Heitzig, Norbert Marwan, and Jürgen Kurths. How basin stability complements the linear-stability paradigm. *Nature Physics*, 9(2):89–92, 2013.

- [38] Vladimir V Klinshov, Vladimir I Nekorkin, and Jürgen Kurths. Stability threshold approach for complex dynamical systems. *New Journal of Physics*, 18(1):13004, 2016.
- [39] R Graham and T Tél. Potential for the Complex Ginzburg-Landau Equation. *EPL (Europhysics Letters)*, 13(8):715, 1990.
- [40] H.K. Leung. Synchronization dynamics of coupled van der Pol systems. *Physica A: Statistical Mechanics and its Applications*, 321(1):248–255, 2003.
- [41] Si Wu and Shun-ichi Amari. Computing with Continuous Attractors: Stability and Online Aspects. *Neural Computation*, 17:2215–2239, 2005.
- [42] Hendrik Wernecke, Bulcsú Sándor, and Claudius Gros. Attractor metadynamics in a recurrent neural network: adiabatic vs. symmetry protected flow. *arXiv preprint arXiv:1611.00174*, 2016.
- [43] István Z Kiss, Craig G Rusin, Hiroshi Kori, and John L Hudson. Engineering Complex Dynamical Structures: Sequential Patterns and Desynchronization. *Science*, 316(5833):1886–1889, 2007.
- [44] Alessandro Treves. Frontal latching networks: a possible neural basis for infinite recursion. *Cognitive Neuropsychology*, 22(3-4):276–291, 2005.
- [45] M Rabinovich, A Volkovskii, P Lecanda, R Huerta, H D I Abarbanel, and G Laurent. Dynamical Encoding by Networks of Competing Neuron Groups: Winnerless Competition. *Phys. Rev. Lett.*, 87(6):68102, 2001.
- [46] V S Afraimovich, V P Zhigulin, and M I Rabinovich. On the origin of reproducible sequential activity in neural circuits. *Chaos: An Interdisciplinary Journal of Nonlinear Science*, 14(4):1123–1129, 2004.
- [47] Valentin S Afraimovich, Mikhail I Rabinovich, and Pablo Varona. Heteroclinic contours in neural ensembles and the winnerless competition principle. *International Journal of Bifurcation and Chaos*, 14(04):1195–1208, 2004.
- [48] Mikhail I Rabinovich, Ramón Huerta, and Valentin Afraimovich. Dynamics of Sequential Decision Making. *Phys. Rev. Lett.*, 97(18):188103, 2006.
- [49] Mikhail I. Rabinovich, Pablo Varona, Irma Tristan, and Valentin S. Afraimovich. Chunking dynamics: heteroclinics in mind. *Frontiers in Computational Neuroscience*, 8:22, 2014.
- [50] Mikhail I. Rabinovich and Pablo Varona. Robust Transient Dynamics and Brain Functions. *Frontiers in Computational Neuroscience*, 5:24, 2011.

- [51] Bulcsú Sándor and Claudius Gros. Complex activity patterns generated by short-term synaptic plasticity. In *ESANN 2017 Proceedings, European Symposium on Artificial Neural Networks, Computational Intelligence and Machine Learning*, 2017.
- [52] Mathias Linkerhand and Claudius Gros. Generating functionals for autonomous latching dynamics in attractor relict networks. *Scientific reports*, 3, 2013.
- [53] Mathias Linkerhand and Claudius Gros. Self-organized stochastic tipping in slow-fast dynamical systems. *Mathematics and Mechanics of Complex Systems*, 1(2):129–147, 2013.
- [54] Yuri A. Kuznetsov. *Elements of Applied Bifurcation Theory*, volume 112 of *Applied Mathematical Sciences*. Springer New York, New York, NY, 2004.
- [55] Arkady Pikovsky, Michael Rosenblum, and Jürgen Kurths. *Synchronization: a universal concept in nonlinear sciences*, volume 12. Cambridge university press, 2003.
- [56] F C Moon and P J Holmes. A Megnetoelastic strange attractor. *Journal of Sound and Vibration*, 65(2):275–296, 1979.
- [57] Takashi Matsumoto. A chaotic attractor from Chua’s circuit. *IEEE Transactions on Circuits and Systems*, 31(12):1055–1058, 1984.
- [58] A. Venkatesan and M. Lakshmanan. Bifurcation and chaos in the double-well Duffing-van der Pol oscillator: Numerical and analytical studies. *Physical Review E*, 56(6):6321–6330, 1997.
- [59] Akira Yamaguchi, Hirokazu Fujisaka, and Masayoshi Inoue. Static and dynamic scaling laws near the symmetry-breaking chaos transition in the double-well potential system. *Physics Letters A*, 135(6-7):320–326, 1989.
- [60] Ruihong Li, Wei Xu, and Shuang Li. Chaos controlling of extended nonlinear liénard system based on the melnikov theory. *Applied Mathematics and Computation*, 178(2):405–414, 2006.
- [61] Shui-Nee Chow, Chengzhi Li, and Duo Wang. *Normal forms and bifurcation of planar vector fields*. Cambridge University Press, 1994.
- [62] Floris Takens. Singularities of vector fields. *Publications Mathématiques de l’IHÉS*, 43(1):47–100, 1974.
- [63] Rifkat Ibragimovich Bogdanov. Versal deformations of a singular point of a vector field on the plane in the case of zero eigenvalues. *Functional analysis and its applications*, 9(2):144–145, 1975.

- [64] Otto E Rössler. An equation for continuous chaos. *Physics Letters A*, 57(5):397–398, 1976.
- [65] L. Chua, M. Komuro, and T. Matsumoto. The double scroll family. *IEEE Transactions on Circuits and Systems*, 33(11):1072–1118, 1986.
- [66] Guanrong Chen and Tetsushi Ueta. Yet another chaotic attractor. *International Journal of Bifurcation and chaos*, 9(07):1465–1466, 1999.
- [67] Jinhu Lü and Guanrong Chen. Generating multiscroll chaotic attractors: theories, methods and applications. *International Journal of Bifurcation and Chaos*, 16(04):775–858, 2006.
- [68] Jinhu Lü and Guanrong Chen. A new chaotic attractor coined. *International Journal of Bifurcation and chaos*, 12(03):659–661, 2002.
- [69] Bo Deng. Constructing homoclinic orbits and chaotic attractors. *International Journal of Bifurcation and Chaos*, 04(04):823–841, 1994.
- [70] Chittaranjan Hens, Syamal K Dana, and Ulrike Feudel. Extreme multistability: Attractor manipulation and robustness. *Chaos: An Interdisciplinary Journal of Nonlinear Science*, 25(5):53112, 2015.
- [71] A G Balanov, N B Janson, and E Schöll. Delayed feedback control of chaos: Bifurcation analysis. *Phys. Rev. E*, 71(1):16222, 2005.
- [72] Xiaodong Luo, Michael Small, Marius-F. Danca, and Guanrong Chen. On dynamical systems with multiple chaotic attractors. *International Journal of Bifurcation and Chaos*, 17(09):3235–3251, 2007.
- [73] J Kengne, Z T Njitacke, and H B Fotsin. Dynamical analysis of a simple autonomous jerk system with multiple attractors. *Nonlinear Dynamics*, 83(1):751–765, 2016.
- [74] Robert Clewley. Hybrid models and biological model reduction with pydstool. *PLoS Computational Biology*, 8(8):e1002628, 2012.
- [75] Pascal Chossat, Martin Golubitsky, and Barbara Lee Keyfitz. Hopf-Hopf mode interactions with  $O(2)$  symmetry. *Dynamics and Stability of Systems*, 1(4):255–292, 1986.
- [76] Claudius Gros, Mathias Linkerhand, and Valentin Walther. Attractor meta-dynamics in adapting neural networks. In *Artificial Neural Networks and Machine Learning - ICANN 2014*, pages 65–72. Springer, 2014.
- [77] Dimitrije Marković and Claudius Gros. Self-organized chaos through poly-homeostatic optimization. *Physical Review Letters*, 105(6):068702, 2010.

- [78] Mária Ercsey-Ravasz and Zoltán Toroczkai. Optimization hardness as transient chaos in an analog approach to constraint satisfaction. *Nature Physics*, 7(12):966–970, 2011.
- [79] Karl Friston. The free-energy principle: a unified brain theory? *Nature Reviews Neuroscience*, 11(2):127–138, 2010.
- [80] Mikhail Prokopenko. *Guided self-organization: Inception*, volume 9. Springer, 2013.
- [81] Jochen Triesch. A gradient rule for the plasticity of a neuron’s intrinsic excitability. In *Artificial Neural Networks: Biological Inspirations - ICANN 2005*, pages 65–70. Springer, 2005.
- [82] Randall D. Beer. A dynamical systems perspective on agent-environment interaction. *Artificial Intelligence*, 72(1-2):173–215, 1995.
- [83] T M McKenna, T A McMullen, and M F Shlesinger. The brain as a dynamic physical system. *Neuroscience*, 60(3):587–605, 1994.
- [84] Eugene M Izhikevich. *Dynamical systems in neuroscience*. MIT press, 2007.
- [85] Wolf Singer. Cortical dynamics revisited. *Trends in Cognitive Sciences*, 17(12):616–626, 2013.
- [86] Rodrigo Echeveste and Claudius Gros. Generating functionals for computational intelligence: The fisher information as an objective function for self-limiting hebbian learning rules. *Frontiers in Robotics and AI*, 1(1), 2014.
- [87] Rodrigo Echeveste, Samuel Eckmann, and Claudius Gros. The fisher information as a neural guiding principle for independent component analysis. *Entropy*, 17(6):3838–3856, 2015.
- [88] Karl Friston and Ping Ao. Free energy, value, and attractors. *Computational and mathematical methods in medicine*, 2012, 2011.
- [89] Nihat Ay, Nils Bertschinger, Ralf Der, Frank Güttler, and Eckehard Olbrich. Predictive information and explorative behavior of autonomous robots. *The European Physical Journal B*, 63(3):329–339, 2008.
- [90] Wulfram Gerstner and Werner M Kistler. *Spiking neuron models: Single neurons, populations, plasticity*. Cambridge university press, 2002.
- [91] Bruce W Knight. Dynamics of encoding in neuron populations: some general mathematical features. *Neural Computation*, 12(3):473–518, 2000.
- [92] J J Hopfield. Neural networks and physical systems with emergent collective computational abilities. *PNAS*, 79(April):2554–2558, 1982.

- [93] J J Hopfield. Neurons with graded response have collective computational properties like those of two-state neurons Biophysics : Hopfield. *Proceedings of the National Academy of Sciences*, 81(May):3088–3092, 1984.
- [94] Anders Lansner. Associative memory models: from the cell-assembly theory to biophysically detailed cortex simulations. *Trends in neurosciences*, 32(3):178–186, 2009.
- [95] Moshe Abeles, Hagai Bergman, Itay Gat, Isaac Meilijson, Eyal Seidemann, Naftali Tishby, and Eilon Vaadia. Cortical activity flips among quasi-stationary states. *Proceedings of the National Academy of Sciences*, 92(19):8616–8620, 1995.
- [96] Tal Kenet, Dmitri Bibitchkov, Misha Tsodyks, Amiram Grinvald, and Amos Arieli. Spontaneously emerging cortical representations of visual attributes. *Nature*, 425(6961):954–956, 2003.
- [97] Ofer Mazor and Gilles Laurent. Transient Dynamics versus Fixed Points in Odor Representations by Locust Antennal Lobe Projection Neurons. *Neuron*, 48(4):661–673, 2005.
- [98] Lauren M Jones, Alfredo Fontanini, Brian F Sadacca, Paul Miller, and Donald B Katz. Natural stimuli evoke dynamic sequences of states in sensory cortical ensembles. *Proceedings of the National Academy of Sciences*, 104(47):18772–18777, 2007.
- [99] Christian K Machens, Ranulfo Romo, and Carlos D Brody. Flexible Control of Mutual Inhibition: A Neural Model of Two-Interval Discrimination. *Science*, 307(5712):1121–1124, 2005.
- [100] Albert K. Lee and Matthew A. Wilson. Memory of Sequential Experience in the Hippocampus during Slow Wave Sleep. *Neuron*, 36(6):1183–1194, 2002.
- [101] Richard H R Hahnloser, Alexay A Kozhevnikov, and Michale S Fee. An ultra-sparse code underlies the generation of neural sequences in a songbird. *Nature*, 419(6902):65–70, 2002.
- [102] Dario L Ringach. Neuroscience: States of mind. *Nature*, 425(6961):912–913, 2003.
- [103] Mikhail I. Rabinovich, Valentin S. Afraimovich, Christian Bick, and Pablo Varona. Information flow dynamics in the brain. *Physics of Life Reviews*, 9(1):51–73, 2012.
- [104] Karl J. Friston. Transients, Metastability, and Neuronal Dynamics. *NeuroImage*, 5(2):164–171, 1997.
- [105] Peter Dayan and Laurence F Abbott. *Theoretical neuroscience*, volume 806. MIT Press, Chambridge, MA, 2001.

- [106] Wulfram Gerstner, Werner M Kistler, Richard Naud, and Liam Paninski. *Neuronal dynamics: From single neurons to networks and models of cognition*. Cambridge University Press, 2014.
- [107] Kimberly Gerrow and Antoine Triller. Synaptic stability and plasticity in a floating world. *Current Opinion in Neurobiology*, 20(5):631–639, 2010.
- [108] Larry F Abbott and Sacha B Nelson. Synaptic plasticity: taming the beast. *Nature neuroscience*, 3:1178–1183, 2000.
- [109] Robert S Zucker. Short-term synaptic plasticity. *Annual review of neuroscience*, 12(1):13–31, 1989.
- [110] Henry Markram and Misha Tsodyks. Redistribution of synaptic efficacy between neocortical pyramidal neurons. *Nature*, 382(6594):807–810, 1996.
- [111] Wade G Regehr. Short-term presynaptic plasticity. *Cold Spring Harbor perspectives in biology*, 4(7):a005702, 2012.
- [112] Yun Wang, Henry Markram, Philip H Goodman, Thomas K Berger, Junying Ma, and Patricia S Goldman-Rakic. Heterogeneity in the pyramidal network of the medial prefrontal cortex. *Nature neuroscience*, 9(4):534–542, 2006.
- [113] Anirudh Gupta, Yun Wang, and Henry Markram. Organizing principles for a diversity of gabaergic interneurons and synapses in the neocortex. *Science*, 287(5451):273–278, 2000.
- [114] Misha Tsodyks, K Pawelzik, and Henry Markram. Neural networks with dynamic synapses. *Neural computation*, 835(1996):821–835, 1998.
- [115] Simon Haykin and Neural Network. A comprehensive foundation. *Neural Networks*, 2(2004):41, 2004.
- [116] Randall D Beer. On the Dynamics of Small Continuous-Time Recurrent Neural Networks. *Adaptive Behavior*, 3(4):469–509, 1995.
- [117] H Sompolinsky, A Crisanti, and HJ Sommers. Chaos in random neural networks. *Physical review letters*, 61(3):259–262, 1988.
- [118] Donald Olding Hebb. *The organization of behavior: A neuropsychological theory*. Psychology Press, 2005.
- [119] Erkki Oja. Principal Components, Minor Componentets, and Linear Neural Networks. *Neural Networks*, 5(6):927–935, 1992.
- [120] E L Bienenstock, L N Cooper, and P W Munro. Theory for the development of neuron selectivity: orientation specificity and binocular interaction in visual cortex. *The Journal of neuroscience : the official journal of the Society for Neuroscience*, 2(1):32–48, 1982.

- [121] Wulfram Gerstner, Richard Kempter, J Leo van Hemmen, and Hermann Wagner. A neuronal learning rule for sub-millisecond temporal coding. *Nature*, 383(6595):76, 1996.
- [122] Rodrigo Echeveste and Claudius Gros. Two-trace model for spike-timing-dependent synaptic plasticity. *Neural Computation*, 27(3):672–698, 2015.
- [123] Misha V Tsodyks and Henry Markram. The neural code between neocortical pyramidal neurons depends on neurotransmitter release probability. *Proceedings of the National Academy of Sciences*, 94(2):719–723, 1997.
- [124] Gianluigi Mongillo, Omri Barak, and Misha Tsodyks. Synaptic theory of working memory. *Science*, 319(5869):1543–6, 2008.
- [125] Jesus M Cortes, Mathieu Desroches, Serafim Rodrigues, Romain Veltz, Miguel A Munoz, and Terrence J Sejnowski. Short-term synaptic plasticity in the deterministic Tsodyks-Markram model leads to unpredictable network dynamics. *Proceedings of the National Academy of Sciences*, 110(41):16610–16615, 2013.
- [126] Omri Barak and Misha Tsodyks. Persistent activity in neural networks with dynamic synapses. *PLoS computational biology*, 3(2):e35, 2007.
- [127] Lawrence Christopher York and Mark C W van Rossum. Recurrent networks with short term synaptic depression. *Journal of computational neuroscience*, 27(3):607–20, 2009.
- [128] Yan Jia and David Parker. Short-term synaptic plasticity at interneuronal synapses could sculpt rhythmic motor patterns. *Frontiers in neural circuits*, 10, 2016.
- [129] Farzan Nadim and Yair Manor. The role of short-term synaptic dynamics in motor control. *Current opinion in neurobiology*, 10(6):683–690, 2000.
- [130] Hazem Toutounji and Frank Pasemann. Behavior control in the sensorimotor loop with short-term synaptic dynamics induced by self-regulating neurons. *Frontiers in neurorobotics*, 8, 2014.
- [131] J J Hopfield and D W Tank. Computing with neural circuits: a model. *Science (New York, N.Y.)*, 233(4764):625–33, 1986.
- [132] Paul Erdős and Alfréd Rényi. On random graphs, I. *Publicationes Mathematicae (Debrecen)*, 6:290–297, 1959.
- [133] Tamás Tél, Ying-Cheng Lai, and Márton Gruiz. Noise-induced chaos: a consequence of long deterministic Transients. *International Journal of Bifurcation and Chaos*, 18(02):509–520, 2008.

- [134] Bulcsú Sándor, Ferenc Járjai-Szabó, Tamás Tél, and Zoltán Néda. Chaos on the conveyor belt. *Phys. Rev. E*, 87(4):42920, 2013.
- [135] György Buzsáki. Neural syntax: cell assemblies, synapsembles, and readers. *Neuron*, 68(3):362–85, 2010.
- [136] David Hansel and German Mato. Short-term plasticity explains irregular persistent activity in working memory tasks. *The Journal of neuroscience : the official journal of the Society for Neuroscience*, 33(1):133–49, 2013.
- [137] Mark D’Esposito. From cognitive to neural models of working memory. *Philosophical transactions of the Royal Society of London. Series B, Biological sciences*, 362(1481):761–72, 2007.
- [138] Alan Baddeley. Working memory: looking back and looking forward. *Nature reviews. Neuroscience*, 4(10):829–39, 2003.
- [139] Omri Barak and Misha Tsodyks. Working models of working memory. *Current opinion in neurobiology*, 25:20–24, 2014.
- [140] Edmund T Rolls, Laura Dempere-Marco, and Gustavo Deco. Holding multiple items in short term memory: a neural mechanism. *PloS one*, 8(4):e61078, 2013.
- [141] Daniel Durstewitz, Jeremy K Seamans, and Terrence J Sejnowski. Neurocomputational models of working memory. *Nature neuroscience*, 3:1184–1191, 2000.
- [142] Auke Jan Ijspeert. Central pattern generators for locomotion control in animals and robots: a review. *Neural Networks*, 21(4):642–653, 2008.
- [143] Carlos Canudas de Wit, Bruno Siciliano, and Georges Bastin. *Theory of robot control*. Springer Science & Business Media, 2012.
- [144] Richard C Dorf and Robert H Bishop. *Modern control systems*. Pearson (Addison-Wesley), 1998.
- [145] Volodymyr Mnih, Koray Kavukcuoglu, David Silver, Andrei A Rusu, Joel Veness, Marc G Bellemare, Alex Graves, Martin Riedmiller, Andreas K Fidjeland, Georg Ostrovski, and Others. Human-level control through deep reinforcement learning. *Nature*, 518(7540):529–533, 2015.
- [146] Alex Graves, Greg Wayne, Malcolm Reynolds, Tim Harley, Ivo Danihelka, Agnieszka Grabska-Barwińska, Sergio Gómez Colmenarejo, Edward Grefenstette, Tiago Ramalho, John Agapiou, Adrià Puigdomènech Badia, Karl Moritz Hermann, Yori Zwols, Georg Ostrovski, Adam Cain, Helen King, Christopher Summerfield, Phil Blunsom, Koray Kavukcuoglu, and Demis Hassabis. Hybrid computing using a neural network with dynamic external memory. *Nature*, 538(7626):471–476, 2016.

- [147] Marc Raibert, Kevin Blankespoor, Gabriel Nelson, Rob Playter, and T Bigdog Team. Bigdog, the rough-terrain quadruped robot. In *Proceedings of the 17th world congress*, volume 17, pages 10822–10825, 2008.
- [148] Jonas Buchli, Jerry Pratt, Nicholas Roy, Michael P Murphy, Aaron Saunders, Cassie Moreira, Alfred A Rizzi, and Marc Raibert. The littledog robot. *The International Journal of Robotics Research*, 30(2):145–149, 2011.
- [149] Alfred Shapere and Frank Wilczek. Self-Propulsion at Low Reynolds Number. *Phys. Rev. Lett.*, 58(20):2051–2054, 1987.
- [150] Vincent C. Müller and Matej Hoffmann. What Is Morphological Computation? On How the Body Contributes to Cognition and Control. *Artificial Life*, 23(1):1–24, 2017.
- [151] Rolf Pfeifer, Max Lungarella, and Fumiya Iida. The challenges ahead for bio-inspired ‘soft’ robotics. *Communications of the ACM*, 55(11):76–87, 2012.
- [152] Georg Martius, Ralf Der, and Nihat Ay. Information driven self-organization of complex robotic behaviors. *PLOS ONE*, 8:e63400, 2013.
- [153] Stefano Nolfi and Dario Floreano. *Evolutionary Robotics: The Biology, Intelligence, and Technology of Self-organizing Machines*. MIT Press, 2000.
- [154] Andrej Gams, Auke J Ijspeert, Stefan Schaal, and Jadran Lenarčič. On-line learning and modulation of periodic movements with nonlinear dynamical systems. *Autonomous Robots*, 27(1):3–23, 2009.
- [155] Ioannis Iossifidis and Gregor Schoner. Dynamical systems approach for the autonomous avoidance of obstacles and joint-limits for an redundant robot arm. In *Intelligent Robots and Systems, 2006 IEEE International Conference on*, pages 580–585. IEEE, 2006.
- [156] Ralf Der and Georg Martius. *From Motor Babbling to Purposive Actions: Emerging Self-exploration in a Dynamical Systems Approach to Early Robot Development*, pages 406–421. Springer, Berlin, Heidelberg, 2006.
- [157] Jonas Buchli, Ludovic Righetti, and Auke Jan Ijspeert. *A Dynamical Systems Approach to Learning: A Frequency-Adaptive Hopper Robot*, pages 210–220. Springer Berlin Heidelberg, Berlin, Heidelberg, 2005.
- [158] Nihat Ay, Holger Bernigau, Ralf Der, and Mikhail Prokopenko. Information-driven self-organization: the dynamical system approach to autonomous robot behavior. *Theory in Biosciences*, 131(3):161–179, 2012.
- [159] Gregor Schöner. Dynamical systems approaches to cognition. *Cambridge handbook of computational cognitive modeling*, pages 101–126, 2008.

- [160] Hazem Toutounji and Frank Pasemann. Autonomous learning needs a second environmental feedback loop. In *Computational Intelligence*, pages 455–472. Springer, 2016.
- [161] Ralf Der and Georg Martius. Self-organized behavior generation for musculoskeletal robots. *Frontiers in Neurorobotics*, 11:8, 2017.
- [162] Russell Smith. Open Dynamics Engine - an open source, high performance library for simulating rigid body dynamics. <http://www.ode.org/>, 2008.
- [163] Robert Osfield. Open Scene Graph - an open source high performance 3D graphics toolkit. <http://www.openscenegraph.org/>, 2002.
- [164] Dimitrije Marković and Claudius Gros. Intrinsic adaptation in autonomous recurrent neural networks. *Neural Computation*, 24(2):523–540, 2012.
- [165] Randall D Beer and Paul L Williams. Information processing and dynamics in minimally cognitive agents. *Cognitive science*, 39(1):1–38, 2015.
- [166] Paul Williams and Randall Beer. Environmental feedback drives multiple behaviors from the same neural circuit. In *Advances in Artificial Life, ECAL 2013*, volume 12, pages 268–275. MIT Press, 2013.
- [167] Silke Steingrube, Marc Timme, Florentin Wörgötter, and Poramate Manoonpong. Self-organized adaptation of a simple neural circuit enables complex robot behaviour. *Nature physics*, 6(3):224–230, 2010.
- [168] Eduard Grinke, Christian Tetzlaff, Florentin Wörgötter, and Poramate Manoonpong. Synaptic plasticity in a recurrent neural network for versatile and adaptive behaviors of a walking robot. *Frontiers in Neurorobotics*, 9:11, 2015.
- [169] Christian Beck and Friedrich Schögl. *Thermodynamics of chaotic systems: an introduction*. Number 4. Cambridge University Press, 1995.
- [170] Ernest Barreto, Brian R. Hunt, Celso Grebogi, and James A. Yorke. From High Dimensional Chaos to Stable Periodic Orbits: The Structure of Parameter Space. *Physical Review Letters*, 78(24):4561–4564, 1997.
- [171] Wen-Xu Wang, Ying-Cheng Lai, and Celso Grebogi. Data based identification and prediction of nonlinear and complex dynamical systems. *Physics Reports*, 644:1–76, 2016.
- [172] Lee DeVille and Eugene Lerman. Modular dynamical systems on networks. *Journal of the European Mathematical Society*, 17(12):2977–3013, 2015.
- [173] Ludwig Arnold. *Random Dynamical Systems*. Springer Science & Business Media, 1998.

- 
- [174] Kumpati S Narendra and Kannan Parthasarathy. Identification and control of dynamical systems using neural networks. *IEEE Transactions on neural networks*, 1(1):4–27, 1990.
- [175] Giancarlo Benettin, Luigi Galgani, Antonio Giorgilli, and Jean-Marie Strelcyn. Lyapunov characteristic exponents for smooth dynamical systems and for Hamiltonian systems; a method for computing all of them. Part 1: Theory. *Meccanica*, 15(1):9–20, 1980.

# Acknowledgements

Here, I would like to thank to all the people who have contributed in one or another way to this work. It has been a long journey from my small village in Transylvania to the cosmopolitan Frankfurt.

First of all, I would like to thank Prof. Claudius Gros for his invaluable guidance throughout these years, for allowing me the freedom to manage my projects and providing me the necessary time to follow my own ideas. I'm also grateful for the delightful discussions about exciting questions of science and life in general.

I thank my teachers who always encouraged me to do my best at everything I do; my physics teacher, Ferenc Illyés, who made me look behind the things and love physics.

I'm grateful to my professors at Babeş-Bolyai University, to Prof. Ferenc Járαι-Szabó for giving me the first research project, to Prof. Zoltán Néda who taught me to enjoy research, which finally lead to this thesis.

I thank Prof. Tamás Tél for introducing me to the beauties of chaos.

I wish to thank my friends, colleagues, and students at ITP for the cheerful discussions. I thank Hendrik Wernecke, Laura Martin, Tim Jahn and Marvin Göbel for the fruitful collaborations with exciting results, and Rodrigo Echeveste for introducing me to neuroscience.

I'm very grateful to Etele Molnár, Rodrigo Echeveste and Casper Drukier for carefully reading and commenting on parts of my thesis. A special thanks goes to Hendrik Wernecke and Kira Riedl for helping with the German translation of the abstract.

I thank my family for their unconditional support in pursuing my dreams. Köszönöm.

Finally, I thank Ági for standing beside me throughout all these years.

**name** Bulcsú Sándor  
**address** 6410, Siolistr. 7, 60323,  
Frankfurt am Main, Germany  
**phone** +49 15 732403123  
**email (personal)** [sbulcsu@gmail.com](mailto:sbulcsu@gmail.com)  
**email (office)** [sandor@itp.uni-frankfurt.de](mailto:sandor@itp.uni-frankfurt.de)  
**date of birth** 23<sup>th</sup> July 1989  
**place of birth** Odorheiu-Secuiesc  
**citizenship** Romanian



### current

2013 - **PhD student, Institut für Theoretische Physik, Goethe Universität, Frankfurt am Main, Germany**  
ADVISOR: **Prof. Claudius Gros**

### education

2011 - 2013 **MSc in Computational Physics, Faculty of Physics, Babeş-Bolyai University, Cluj-Napoca, Romania**  
ADVISOR: **Prof. Zoltán Néda**

2008 - 2011 **BSc in Physics, Faculty of Physics, Babeş-Bolyai University, Cluj-Napoca, Romania**  
ADVISOR: **Prof. Zoltán Néda, Asst. Ferenc Járαι-Szabó**

2004 - 2008 **High school, Orbán Balázs Gimnázium, Cristuru-Secuiesc, Romania**

### teaching

2013 - 2017 **Teaching Assistant**  
Electrodynamics, Self-Organisation: Theory and Simulations, Programming for Physicists, Complex and adaptive dynamical systems, Advanced Introduction to C++ and Scientific Computing

### languages

Hungarian **native**  
Romanian **good**  
English **good**  
German **intermediate**

### computational skills

programming **Python, C, C++, Java, Fortran**  
systems **Linux and Windows**  
office **Latex, Inkscape, Vi, Libre Office**

## visits

- 2012 - 2013 **Eötvös Loránd University, Budapest, Hungary (6 months)**  
ADVISOR: **Prof. Tél Tamás**
- 2011 **University of Bergen, Bergen, Norway (2 weeks)**  
ADVISOR: **Prof. Zoltán Nédá**

## schools

- 2016 **Advanced Course on "Piecewise Smooth Dynamical Systems"**  
CRM, Universitat Autònoma de Barcelona, Barcelona, Spain
- 2015 **INCF Short Course on Information Processing in Neural Systems**  
Institute of Cognitive Science, Osnabrück, Germany
- 2015 **Interdisciplinary College**  
Gesellschaft für Informatik, Günne, Germany
- 2014 **Winter School in Quantitative Systems Biology**  
International Centre for Theoretical Physics, Trieste, Italy
- 2011 **IPP Summer University on Plasma Physics and Fusion Research**  
Max Planck Institute for Plasma Physics, Greifswald, Germany

## awards, scholarships

- 2016 **2nd Poster Prize**  
by Advisory board of Dynamics Days Europe at XXXVI Dynamics Days Europe 2016, Corfu, Greece
- 2016 **Travel award**  
by U.S. National Science Foundation at Dynamics Days US 2016, Durham, NC, USA
- 2014 **Poster Prize Winner**  
by F1000 Research at OCCAM 2014, Osnabrück, Germany
- 2012 - 2015 **Over-the Border Excellent Student Scholarship**  
by National Excellence Program, Office of Public Administration and Justice, Budapest, Hungary
- 2012 - 2015 **Collegium Talentum Scholarship**  
by Collegium Talentum, Tatabánya, Hungary

papers

- 2017 **How to test for partially predictable chaos**  
Hendrik Wernecke, **Bulcsú Sándor**, Claudius Gros, Scientific Reports 7:1087
- 2016 **Closed-loop robots driven by short-term synaptic plasticity: Emergent explorative vs. limit-cycle locomotion**  
Laura Martin, **Bulcsú Sándor**, Claudius Gros, Frontiers in Neurobotics 10:12
- 2016 **Time-scale effects on the gain-loss asymmetry in stock indices**  
**Bulcsú Sándor**, Ingve Simonsen, Bálint Zsolt Nagy, Zoltán Neda, Phys. Rev. E 94(2): 022311
- 2015 **The sensorimotor loop as a dynamical system: How regular motion primitives may emerge from self-organized limit cycles**  
**Bulcsú Sándor**, Tim Jahn, Laura Martin, Claudius Gros, Frontiers in Robotics and AI 2:31
- 2015 **A versatile class of prototype dynamical systems for complex bifurcation cascades of limit cycles**  
**Bulcsú Sándor**, Claudius Gros, Scientific Reports 5: 12316
- 2015 **A spring-block analogy for the dynamics of stock indexes**  
**Bulcsú Sándor**, Zoltán Neda, Physica A: Statistical Mechanics and its Applications 427: 122-131
- 2013 **Chaos on the conveyor belt**  
**Bulcsú Sándor**, Ferenc Járjai-Szabó, Tamás Tél, Zoltán Neda, Phys. Rev. E 87(4): 042920
- 2012 **Rms-flux relation in the optical fast variability data of BL Lacertae object S5 0716+714**  
Gabriela Raluca Mocanu and **Bulcsú Sándor**, Astrophysics and Space Science, 342(1): 147-153
- 2011 **Spring-block model for a single-lane highway traffic**  
Ferenc Járjai-Szabó, **Bulcsú Sándor** and Zoltán Neda, Central European Journal of Physics 9(4): 1002-1009

conference proceeding

- 2017 **Complex activity patterns generated by short-term synaptic plasticity**  
**Bulcsú Sándor**, Claudius Gros, ESANN 2017 Proceedings ISBN 978-2-87587-038-4: 317

extended abstracts

- 2015 **Limit cycles with transient state dynamics in cyclic networks**  
**Bulcsú Sándor**, Claudius Gros, BMC Neuroscience 16(Suppl 1): P89

posters

- 2016 **The role of sensori-motor loop for cognition**  
EUCognition Meeting, "Cognitive Robot Architectures", TU Wien, Vienna, Austria
- 2016 **Short-term synaptic plasticity generates complex activity patterns of cell assemblies in Hopfield-networks**  
XXXVI Dynamics Day Europe, Corfu Holiday Palace Hotel, Corfu, Greece
- 2016 **Complex time series of cell assemblies generated by short-term synaptic plasticity**  
9th Bernstein Sparks Workshop, Max Planck Institute for Dynamics and Self-Organization, Göttingen, Germany
- 2016 **A new class of prototype dynamical systems for constructing multiple coexisting attractors**  
Dynamics Days US 2016, Duke University, Durham, NC, USA
- 2015 **Limit cycles with transient state dynamics in cyclic networks**  
CNS 2015, Organization for Computational Neurosciences, Prague, Czech Republic
- 2015 **A prototype dynamical system with a generalized mechanical potential**  
DPG 2015, Technische Universität Berlin, Berlin, Germany
- 2015 **Transient state dynamics arising from short-term synaptic plasticity**  
OCCAM 2015, Institute of Cognitive Science, Osnabrück, Germany
- 2014 **Limit cycles in a ring network**  
WSQSB 2014, International Centre for Theoretical Physics, Trieste, Italy
- 2014 **Dynamics of neural networks with transient synaptic plasticity rules**  
OCCAM 2014, Institute of Cognitive Science, Osnabrück, Germany
- 2014 **Short-term synaptic plasticity in a ring network**  
ESI-SyNC 2014, Ernst Strüngmann Institute for Neuroscience, Frankfurt am Main, Germany
- 2014 **Dynamics of neural networks with transient synaptic plasticity rules**  
DPG 2014, Technische Universität Dresden, Dresden, Germany
- 2012 **Time scale effects on the asymmetry of inverse statistics in stock markets**  
TIM 12, West University, Timisoara, Romania

- 2017      **A dynamical systems approach to robotics: the role of attractors in locomotion**  
Seminars in Statistical Physics, ITP, Eötvös Loránd University, Budapest, Hungary
- 2017      **Complex activity patterns generated by short-term synaptic plasticity**  
ESANN 2017, Hotel Novotel, Bruges, Belgium
- 2016      **Partial predictability in chaos**  
Seminars in Statistical Physics, ITP, Eötvös Loránd University, Budapest, Hungary
- 2015      **A new prototype dynamical system with a generalised mechanical potential**  
Seminars in Statistical Physics, ITP, Eötvös Loránd University, Budapest, Hungary
- 2014      **Dynamics of working memory**  
Seminars in Statistical Physics, ITP, Eötvös Loránd University, Budapest, Hungary
- 2013      **Chaos on the conveyor belt**  
Magyar Fizikus Vándorgyűlés, Roland Eötvös Physical Society, Debrecen, Hungary
- 2013      **The complex phase space of a simple mechanical system**  
XXXI. OTDK FiFöMa, University of Technology and Economics, Budapest, Hungary
- 2013      **Time scale effects on the asymmetry of inverse statistics in stock markets**  
Statistical Physics Day, Hungarian Academy of Sciences, Budapest, Hungary